Optical Holographic Microscopy for Bio- and Nanoparticle Characterization

Doctoral Thesis
by

Unai Ortiz de Orruño Cuesta

Thesis Advisor:

Prof. Dr. Niek F. van Hulst

ICFO – Institut de Ciències Fotòniques

UPC – Universitat Politècnica de Catalunya

January 2023

Thesis advisor:

Prof. Dr. Niek F. van Hulst

Thesis committee:

Prof. Dr. Ramón A. Álvarez Puebla (Universitat Rovira i Vigili, Tarragona, Spain)

Prof. Dr. Laura M. Lechuga (ICN2 – Institut Català de Nanociència i Nanotecnologia, Barcelona, Spain)

Prof. Dr. Valerio Pruneri (ICFO – Institut de Ciències Fotòniques, Castelldefels, Spain)

A mi familia

Abstract

Nowadays, being able to precisely characterize nanoparticles is of key relevance in a wide range of scenarios. For instance, chemical and pharmaceutical industries often rely in particle-sizing for quality control. In a clinical context, in contrast, sensitive bioparticle characterization platforms can lead to the diagnosis of early-stage illnesses. However, the needs between each scenario vary, due to the differences in samples' composition and the particle-property of interest. Hence, several nanoparticle characterization techniques have emerged, each one based on a different physical principle and best suited for particular usage scopes.

In this thesis, I improve the optical nanoparticle sizing techniques by using holography. I present different optical systems that image nanoparticles and record their scattering signal into holograms. I show how to reconstruct the scattered light's wavefront using holographic processing tools and how to extract the particle-size information from it. I prove the capabilities of the holographic imaging systems that I introduce by providing their technical characterization and by measuring relevant samples.

First, I introduce an imaging system with an extended the dynamic range compared to conventional darkfield microscopes. I demonstrate the nanoparticle sizing capabilities of such holographic platform using calibration samples. Moreover, I provide a proof-of-concept in the form of the characterization of a clinical sample, composed by extracellular vesicles, to demonstrate the feasibility of the platform for the development of point-of-care systems.

Afterwards, I show how nanoparticle tracking analysis (NTA), that is to size particles from their diffusion, can be improved by using holography. The use of holography not only increases the NTA's precision, thanks to its ability to capture better the particles' diffusion, but also provides the refractive index information of the sample. The latter is of especial interest when measuring samples of unknown compositions, such as clinical extractions. I present experimental evidence of the improvements in the NTA's sizing precision and the simultaneous retrieval of the refractive index.

Additionally, I measure the radial shift of the nanoparticles induced by the formation of protein-coronas, which I believe that proves the platform's relevance for studying the particles' behaviour in biological fluids.

Finally, I present a system that confines particles in the volume-of-view of a holographic imaging system for further improving the NTA's sizing precision. Such platform's design was motivated by the promising results obtained using holographic NTA and its potential usage on fundamental research of protein-corona formation. The idea behind the system is to obtain longer particle-diffusion trajectories for pushing the holographic NTA sensitivity down to what is necessary to detect the absorption of a single protein onto a nanoparticle. I demonstrate the capabilities of such platform by showing a thorough technical evaluation based on experimental evidence.

I foresee that the presented holographic platforms will find many applications of both fundamental and applied nature. In particular, considering the ability of such platforms to analyse polydisperse samples, I expect to contribute to advances in the fundamental research of extracellular vesicles.

Resum

Avui en dia, la correcta caracterització de les nanopartícules és clau en molts aspectes. Per exemple, las industries química i farmacèutica normalment confien en la mida de les partícules per a fer el control de qualitat. Per altra banda, en un context clínic la caracterització de certes biopartícules pot ajudar a diagnosticar diferents malalties en el seu inici. Tot i així, les necessitats en els diferents camps varia, degut a la diferència en la composició de les mostres i les propietats de les partícules d'interès. Per tant, s'han desenvolupat diferents tècniques per a caracteritzar nanopartícules, cadascuna basada en un principi físic diferent i adequades a àmbits d'ús específics.

En aquesta tesi, he millorat les tècniques òptiques per a mesurar la mida de nanopartícules fent servir holografia. Presento diferents sistemes òptics d'imatge que capten la llum que dispersen les nanopartícules i la graven en hologrames. Mostro com reconstruir el front d'ona de la llum dispersada fent servir eines de processament hologràfic i com extreure d'aquesta informació la mida de la partícula. Demostro la capacitat dels sistemes d'imatge per holografia que presento proporcionant una caracterització tècnica i mesurant mostres rellevants.

Primer, introdueixo un sistema d'imatge amb un rang dinàmic ampliat en comparació als microscopis de camp fosc convencionals. Demostro la capacitat de mesura de nanopartícules d'aquesta plataforma hologràfica fent servir mostres de calibratge. A més a més, aporto una prova de concepte caracteritzant una mostra clínica formada per vesícules extracel·lulars, per tal de demostrar la viabilitat de la plataforma per a desenvolupar sistemes de proves al punt de atenció.

Tot seguit, milloro el anàlisi de seguiment de nanopartícules (*Nanoparticle Tracking Analysis*, NTA), fet servir per mesurar partícules a partir de la seva difusió, gracies a la holografia. L'ús d'holografia no només augmenta la precisió del NTA per la seva capacitat de capturar millor la difusió de les partícules, si no que també aporta l'índex de refracció de la mostra. Aquest és d'especial interès a mesurar mostres de composició desconeguda, com les extraccions clíniques. Presento proves

experimentals de la millora de mesures de mida per NTA i de l’obtenció simultània de l’índex de refracció. Addicionalment, mesuro el canvi radial induït per la formació de corones de proteïnes, demostrant la rellevància de la plataforma per l’estudi del comportament de les partícules en fluids biològics.

Finalment, presento un sistema que confina partícules en el volum de visió d’un sistema d’imatge hologràfic per a millorar la precisió de les mesures per NTA. El disseny d’aquesta plataforma va ser motivat per els bons resultats fent servir el NTA hologràfic i el seu potencial ús en investigació bàsica en la formació de corones de proteïnes. La idea d’aquest sistema és obtenir trajectòries de la difusió de partícules més llargues, augmentant la sensibilitat del NTA hologràfic per tal de detectar l’absorció d’una única proteïna a una nanopartícula. Demostro les capacitats d’aquesta plataforma mitjançant una minuciosa avaluació tècnica basada en evidencies experimentals.

Preveig que les plataformes hologràfics presentades en aquesta tesi es podran utilitzar en varies aplicacions, tan en investigació bàsica com aplicada. En particular, considerant la capacitat d’aquestes plataformes per analitzar mostres polidisperses, espero contribuir a avançar la recerca bàsica de vesícules extracel·lulars.

Resumen

Hoy en día, la correcta caracterización de las nanopartículas es clave en muchos aspectos. Por ejemplo, las industrias química y farmacéutica a menudo confían en la medida de las partículas para hacer el control de calidad. Por otro lado, en un contexto clínico la caracterización de ciertas biopartículas puede ayudar a diagnosticar diferentes enfermedades en etapas tempranas. Sin embargo, las necesidades en los diferentes campos varían, debido a la diferencia en la composición de las muestras y en las propiedades de las partículas de interés. Por tanto, se han desarrollado diferentes técnicas para caracterizar nanopartículas, cada una basada en un principio físico diferente y adecuadas a ámbitos de uso específicos.

En esta tesis, he mejorado las técnicas ópticas para medir el tamaño de las nanopartículas mediante el uso de la holografía. Presento diferentes sistemas ópticos de imagen que captan la luz que dispersan las nanopartículas y la graban en hologramas. Muestro como reconstruir el frente de onda de la luz dispersada usando herramientas de procesamiento holográfico y como extraer de esta información la medida de la partícula. Demuestro la capacidad de los sistemas de imagen holográficos que presento proporcionando una caracterización técnica y midiendo muestras relevantes.

Primero, introduzco un sistema de imagen con un rango dinámico ampliado en comparación a los microscopios de campo oscuro convencionales. Demuestro la capacidad de medida de nanopartículas de esta plataforma holográfica usando muestras de calibración. Además, aporto una prueba de concepto caracterizando una muestra clínica formada por vesículas extracelulares, para demostrar la viabilidad de la plataforma en cuanto al desarrollo de sistemas de pruebas en el punto de atención.

A continuación, mejoro el análisis de seguimiento de nanopartículas (*Nanoparticle Tracking Analysis*, NTA), el cual mide las partículas mediante el estudio de su difusión, gracias a la holografía. El uso de la holografía no solo aumenta la precisión del NTA por su capacidad de capturar mejor la difusión de las partículas, sino que

también aporta el índice de refracción de la muestra. Esto es de especial interés para medir muestras de composición desconocida, como las extracciones clínicas. Presento pruebas experimentales de la mejora de las mediciones del tamaño por NTA y de la obtención simultánea del índice de refracción. Adicionalmente, mido el cambio radial inducido por la formación de coronas de proteínas, lo cual demuestra la relevancia de la plataforma para el estudio del comportamiento de las partículas en fluidos biológicos.

Finalmente, presento un sistema que confina partículas en el volumen de visión de un sistema de imagen holográfico para mejorar la precisión de las medidas por NTA. El diseño de esta plataforma fue motivado por los buenos resultados usando el NTA holográfico y su uso potencial en investigación básica sobre la formación de coronas de proteínas. La idea de este sistema es obtener trayectorias de difusión de partículas más largas, aumentando la sensibilidad del NTA holográfico con tal de detectar la absorción de una única proteína a una nanopartícula. Demuestro las capacidades de esta plataforma mediante una minuciosa evaluación técnica basada en evidencias experimentales.

Preveo que las plataformas holográficas presentadas en esta tesis se podrán utilizar en varias aplicaciones, tanto en investigación básica como aplicada. En particular, considerando la capacidad de estas plataformas para analizar muestras polidispersas, espero contribuir a la investigación básica de vesículas extracelulares.

Table of Contents

Chapter 1:

Introduction

Since their invention four centuries ago, microscopes have enabled innumerable scientific advances. In fact, the progresses in fields such as histology or microbiology, to name a few, have been historically related to the development of microscopy.

Nowadays, our need for analysing nanoobjects of few nanometres presents a challenge for optical microscopy. The wave-nature of light limits the lateral-resolution of optical devices because of its diffraction[1], which complicates resolving nanoscopic features shorter than half wavelength. In addition, the low scattering efficiency of particles of few nanometres leads to weak signals. In consequence, several non-optical techniques have emerged for characterizing nanoparticles[2–4].

The interferometric scattering microscope (iSCAT), presented by Jacobsen *et.al.*[5], showed that it was possible to efficiently image and size nanoparticles smaller than the diffraction limit in an optical manner. iSCAT boosts the weak signal of nanoparticles by interfering the light scattered by them with a bright reference wave. The enhanced signal results in images of higher contrast that is then quantified for retrieving the particles' size information. Additionally, the enhanced contrast made possible to track particles in 2D[6–8] and even in 3D[9–11].

However, even though iSCAT's sensing capabilities enable single protein's molecular weight characterization[12,13], its implementation as a routine nanoparticle sizing technique is limited. The interference-based signal boost leads to sizing ambiguities, which hinder its applicability when there is no previous knowledge of sample.

Interestingly, since iSCAT's images are based on the interference of light, they contain the amplitude and phase information of the interfering waves. In other words, said images are essentially holograms and, thus, the recorded signal is fully described by holography's theory[14–16].

Motivated by the holographic description of iSCAT's signal, this thesis aims at implementing holographic microscopes able to size nanoparticles. Specifically, the thesis focuses on microscope designs that reconstruct the wavefront originated from the light scattered by the sample in order to avoid the mentioned iSCAT sizing ambiguities.

First, I implement a microscope, named *k*-scope, that sizes nanoparticles by quantifying their scattered light intensity from the reconstructed wavefronts. The *k*-scope's name comes from the *k*-space images it records. In such images the light produced by diffraction limited particles is spread over the *k*-space plane[17]. In consequence, when imaging polydisperse nanoparticle samples the bright emitters do not locally saturate the camera, which results in an extended dynamic range.

I show the *k*-scope's sizing capabilities by analysing both metallic and dielectric fixed nanoparticles. The measurements I present demonstrate that the *k*-scope can simultaneously image 20 and 250 nm nanoparticles. Moreover, I show that the *k*-scope can successfully size nanoparticles by relying on calibration measurements obtained from a different material. In addition, I provide proof-of-concept measurements of a clinical sample composed of extracellular samples.

Secondly, I present a modification of the *k*-scope that estimates nanoparticles' size by examining their diffusion in a liquid, what is known as nanoparticle tracking analysis (NTA)[18,19]. Such platform, the holoNTA, propagates the reconstructed wavefront for localizing the nanoparticles in 3D and, at the same time, quantifies the scattered light's intensity. The two-parameter characterization yields particles' refractive index in addition to their size.

I validate holoNTA's sensing capabilities by characterizing metallic and dielectric particles. Presented measurements show that holoNTA can successfully resolve samples composed of particles of different sizes and dielectric constants. Furthermore, I demonstrate holoNTA's precision by measuring the particles' diameter shift induced by protein-corona formations.

Finally, I present a platform that aims at increasing the holoNTA's sizing capabilities. Said platform uses microwells for trapping individual nanoparticles in the field-of-view of the microscopes, which results in extended track lengths. According to the relation in between the sizing precision and the track length in NTA measurements[20,21], such track lengths dramatically reduce the sizing error.

I show the 3D trajectory of a trapped nanoparticle over several minutes, which demonstrates that the particles free-float inside of the microwells and that they do not leave them. I analyse such trajectory for providing an experimental evidence of how the track length affects the particles' sizing uncertainty. In addition, I prove the nanoparticles' stability inside of the microwells by showing their temporal sizing.

Thesis outline

- In Chapter 2 first I provide an overview of the most relevant routine nanoparticle sizing technologies. I explain their function, main characteristics and scope. Then I talk about how we can infer a particle's size by imaging it with an optical microscope by both quantifying its scattering signal and analysing its diffusion in a liquid.
- In Chapter 3 I describe the principles of holography and its implementation into an optical microscope. I start by briefly introducing *traditional* optical holography, which is necessary for understanding its digital counterpart. I continue by explaining the latter, for which I show how we can numerically reconstruct a warfront from a digital hologram. Next, I show how to experimentally implement a holographic microscope. I explain the different experimental parameters and their effect on the reconstructed wavefront. Finally, I outline how to digitally correct the potential optical aberrations and propagate the reconstructed wavefront.
- In Chapter 4 I introduce the *k*-scope. First, I explain why recording *k*-space images extends the dynamic range. Then I show the experimental implementations of the *k*-scope and discuss its signal analysis. Afterwards, I characterize *k*-scope's signal stability. I continue by showing nanoparticles' sizing measurements, which includes data of metallic and dielectric particles. I demonstrate that calibration curves can be numerically adapted for sizing

other materials. Finally, I present proof-of-concept measurements of extracellular vesicles[22–24].

- In Chapter 5 I present the holoNTA. I start by discussing about NTA and how its precision depends on the particles' track lengths. I continue by explaining the importance of localizing a particle in 3D for extending the particles' tracking time. I continue by I showing the experimental implementation of the holoNTA and discussing the signal analysis. Then I demonstrate the sizing and refractive index retrieval capacities of holoNTA by characterizing metallic and dielectric particles. Finally, I show holoNTA's sizing precision by resolving particles' diameter shift induced by protein-corona formations.
- In Chapter 6 I introduce a microwell system that aims at trapping free-floating nanoparticles for confining them in the field-of-view of a microscope. First, I introduce the design of the microwell system and I continue by showing how it is microfabricated. Then I explain how the particles are trapped and I discuss the data analysis. Afterwards, I demonstrate that the particles do not leave the microwells by showing the 3D localizations of a nanoparticle over many minutes. The I experimentally show how NTA's precision depends on the track length. Next, I prove the system's stability by showing the temporal sizing of several particles. Finally, I characterize the sizing precision of the system.
- In Chapter 7 I summarise the present thesis work and I provide the outlook of the possible future developments.

Chapter 2:

Label-free particle sizing

In this chapter I briefly review the most commonly used label-free nanoparticle characterization techniques. I explain their usage, scope and physical working principles. The overview puts into context the sensing platforms presented in the upcoming chapters. In addition, I describe in detail the two nanoparticle sizing approaches used by such platforms: the quantification of the scattered light and the nanoparticle tracking analysis method.

2.1 Introduction

Our understanding about the *nanoworld* has gradually increased in parallel to the development of our tools to characterize it. Therefore, there is a high interest in developing new *nanodecoding* tools. Characterizing nanoparticles[2–4] is not an exception, due their potential impact in the development of novel nanomedicines and diagnosis platforms.

Analysing the properties of these nano-objects is not a simple task. On one hand, due to the vast number of parameters; size, surface charge, composition, shape or surface markers, to name a few[4]. On the other hand, because of their widely different nature. For example, the industrially synthetized metallic particles and the vesicles extracted from human serum have little in common, other than the *nanoparticle* definition. As a result, we lack an *ideal* tool to be able to measure every single property for any particle. Furthermore, it seems unrealistic to achieve such universal tool. Therefore, the choice of the appropriate tools to use is driven by the different needs of each scenario; such as the properties of interest, the nature of the particles or the precision needed.

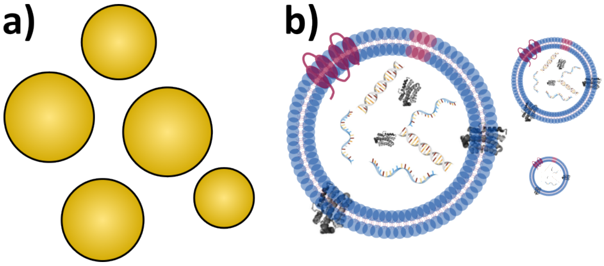

Figure 2.1, Nanoparticles. Representation of a) industrially synthetized homogeneous gold colloidal nanoparticles and b) vesicles extracted form clinical samples.

This chapter aims at providing an overview of the most common label-free nanoparticle sizing methods, which includes their function, main characteristics and scope. Motivated by the working principles of the sizing platforms developed in this thesis work, the scattering intensity quantification and nanoparticle tracking based methods are explained in further detail. A section dedicated to the particle sizing using optical microscopes introduces said approaches.

2.2 Methods

Several label-free nanoparticle sizing techniques have been proposed, and adopted, during the last years. Each of them is based on different physical principles and best suited for particular needs.

Transmission electron microscopes (TEM) are one of the most extended nanoparticle sizing devices due to their extraordinary lateral resolution, down to 0.05 nm[25]. As shown in Figure 2.2a, these devices propagate an electron beam through the sample and the image formed by the transmitted electrons is recorded[26–28]. These images provide the size, the shape[27] and, because the electrons interact with the whole sample volume, the crystal structure of the individual particles[29].

Due to TEM's working principle, samples must be electron-transparent, which results in thin specimens of typically less than 200 nm in thickness[4]. In addition, samples must resist the high-vacuum and the electron beam energy, of the order of 100 keV, employed during the measurements[27,28]. Otherwise, measurements are prone to bias because of the potential sample modifications induced by the mentioned tough measurement conditions. Furthermore, said vacuum and electron beam energy requirements make TEM not compatible with relevant biological conditions and, thus, *in vivo*/*in vitro* studies are not possible.

Besides, obtaining meaningful statistics for nanoparticle properties requires analysing several particles[27]. Said analysis tends to be manual and, thus, a time-consuming process[26,30]. As a result, TEM's throughput is limited. Moreover, TEM devices are expensive[4] and require an extensive sample preparation[26], which complicates its routine implementation.

Scanning electron microscopes (SEM) focus a moving electron beam onto the sample surface[31], as shown in Figure 2.2b. While performing the scan, the beam pumps local atoms and they emit secondary electrons. A sensor records these electrons as a matter of the moving-beam position and, as a result, the sample image is formed. We obtain the size and shape of the individual particles from those images, with a lateral resolution of few nanometers[4]. Moreover, we can perform surface composition studies by recording the backscattered electrons[32] or the sample x-ray emission[33] along with the secondary electrons.

Compared to TEM devices, SEM systems employ lower beam energies[31], often lower than 1 keV, which has some important implications. On one hand, the penetration depth of SEM devices is limited to the surface[4,31,34]. As a consequence, the sample thickness is not a limitation, but the crystal structure cannot be accessed. On the other hand, the potential sample damage associated to the electron beam energies is lower for SEM measurements, although not completely avoided[31,34]. In addition, the high-vacuum applied during measurements[35,36] and the extensive sample preparation, which often implies a thin metallic film coating for non-conductive samples[31,37,38], also contribute to the potential SEM sizing bias. Moreover, both methods have similar throughput limitations[39] and incompatibilities regarding biologically relevant conditions. Finally, the high cost associated to SEM systems, although lower than their TEM counterparts[4,31], further reduces its routine implementation.

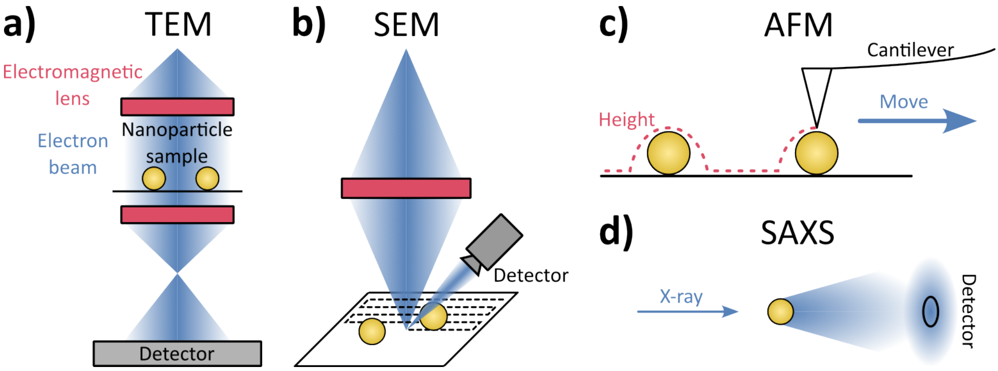

Figure 2.2, Dry nanoparticle sizing methods. a) Transmission electron microscopy (TEM), an electron beam is transmitted through the particles and projected onto a sensor. b) Scanning electron microscopy (SEM), an electron beam scans the sample. Secondary electrons are detected. c) Atomic force microscopy (AFM), a tip scans the sample surface. A height profile is acquired. d) Small angle x-ray scattering (SAXS), nanoparticles are illuminated with an x-ray beam. A detector collects scattered radiation at the small angles.

Atomic force microscopes (AFM) yield the topological information of a sample by scanning a sharp tip over the surface[40–42]. The tip is placed at the end of a cantilever, as depicted in Figure 2.2c. The force that the sample's surface exerts on the tip during the scan is tracked into the deformation of the cantilever which consequently allows the topology and the surface to be resolved, providing high resolution-maps[4]. AFM can operate in liquid[43].

We can retrieve particles' individual size from the topological information, although that the latter is often difficult to interpret[44]. On one hand, because the obtained height profile, sketched in Figure 2.2c, is a convolution of the surface motifs and the tip shape[45,46], which typically results in a higher vertical resolution than the lateral one. On the other hand, due to the topological bias related to the potential sample damage due to its interaction with the tip[47–50]. As a consequence, highly skilled users are often required. In addition, AFM suffers from a limited throughput[4]. Nonetheless, a deep understanding of the different scanning techniques and the available tips permits the characterization of several additional parameters, such as elasticity[51,52], surface potential[53,54] or magnetism[55,56].

Small-angle x-ray scattering (SAXS) devices characterize nanoparticles by illuminating them with an x-ray beam and recording the scattered radiation at low angles[57,58], as shown in Figure 2.2d. As a result, the particle size and agglomeration state are accessed in a non-destructive form and with minimal sample preparation. SAXS measurements can be performed for particles in both dry and liquid suspension states[4].

Interestingly, SAXS can also provide morphology[58–60], crystallinity[61], porosity[58,61] and molecular weight[57] information. Regarding the solute samples, it is compatible with most biological buffers[62]. However, SASX in an ensemble method, i.e. does not provide the individual particle data. Moreover, SAXS struggles to precisely describe polydisperse samples, unless prior sample knowledge is available when performing the data interpretation[63].

Dynamic light scattering (DLS) yields nanoparticles' size-distributions by analysing particles' Brownian motion in solution[64–66]. Figure 2.3a shows DLS working principle. A laser beam is transmitted through the sample and the scattered light is recorded. The temporal fluctuations of the latter are directly related to the diffusion time of the nanoparticles and, thus, their size.

The minimal acquisition and analysis times[67,68], together with the wide solvent compatibility[4,68] and the ability to detect small nanoparticles[69], make DLS an extremely suitable technique for routine and rapid characterization measurements. However, DLS does not provide the individual particle size[70,71], due to its ensemble nature. Moreover, when dealing with polydisperse samples, the size-distribution estimation tents to bias towards the larger particles[68,72].

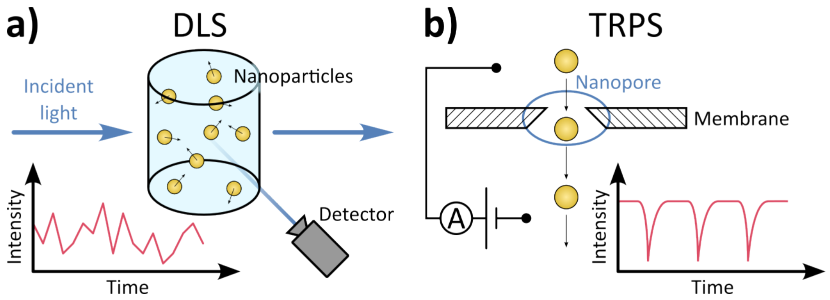

Figure 2.3, Nanoparticle characterization methods. a) Dynamic light scattering (DLS), nanoparticles in solution scatter light from an incident beam. A detector tracks the dispersed light intensity over time. b) Tunable resistive pulse sensing (TRPS), a voltage and a particle flow are applied across a membrane. The ionic current is measured.

Tunable resistive pulse sensing (TRPS) characterizes particles in suspension by analysing the current changes they induce when passing through an aperture[73,74], as illustrated in Figure 2.3b. A voltage difference is applied across a nanopore, which induces an ionic current flow that is monitored. A pressure driven nanoparticle flow passes through said pore and when a particle crosses the aperture it is partially blocked. As a result, there is a temporal change in the current which, according to Coultier principle, is proportional to the blocking particle's size[75,76]. For that reason, TRPS provides individual particle sizing.

The particle flux (J) across the pore is described as[73]

$$J = J_{ep} + J_{eo} + J_{pdf} + \cdots, \tag{2.1}$$

where the three most important terms for TRPS are the electrophoresis (J_{ep}), the electro-osmosis (J_{eo}) and the pressure-driven flow (J_{pdf}). When $J_{pdf} \gg J_{ep} + J_{eo}$, the pulse rate of the monitored current is proportional to the particle flow rate and provides information about the nanoparticle concentration along with the particles' size, if combined with calibration measurements[73].

Moreover, TRPS can estimate individual nanoparticle's surface-charge by combining the pore's zeta-potential and the particles' velocity[73,74]. The latter is acquired from the recorded pulse shape, as long as J_{pdf} is known from calibration samples.

TRPS requires a conductive sample medium, which makes it compatible with physiological buffers[77]. For that reason, TRPS has been used to detect DNA molecules[78] and size extracellular vesicles[73]. Besides, its pore size can be tuned during data acquisition, which adapts its sensitivity[73].

Size exclusion chromatography (SEC) separates nanoparticles according to their hydrodynamic radius[79,80]. Figure 2.4a illustrates SEC's functioning. A separation column is filled with porous microparticles and nanoparticles in suspension, which constitute the solid and the liquid phase respectively. Pressure is applied, so that it induces the liquid phase to flow along the column. Nanoparticles interact with the solid phase while traveling along the separation column. Said interactions retain the moving nanoparticles and depend on the size of the latter. The smaller the particle, the more interactions and, thus, the longer the travel times. As a result, nanoparticles arrive at the separation column's end sorted by their hydrodynamic radius, which allows to divide the liquid phase into highly monodisperse fractions. The use of calibration samples provides absolute sizing[79,81].

Although that SEC can resolve polydisperse samples' size-distributions, it struggles with inhomogeneous particle populations due to the impact in the relative travel times that the different particles' shape[82] and surface charge[83] induce. Still, there is a high interest in SEC because of its compatibility with industrial production[84].

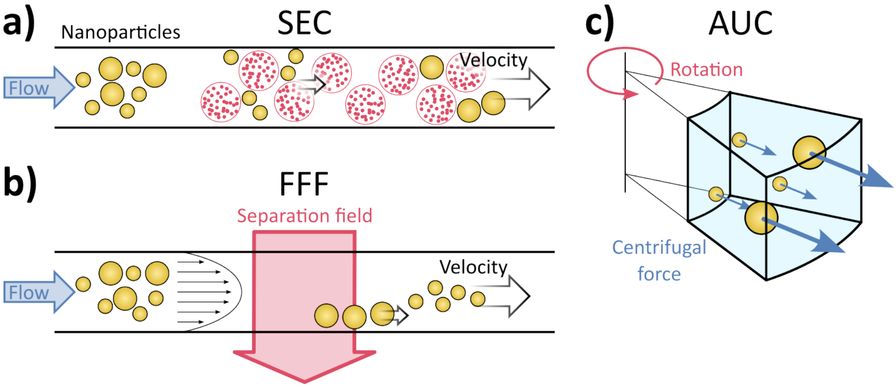

Figure 2.4, Sample fractionalization techniques. a) Size exclusion chromatography (SEC), the sample flows through porous microparticles. Large particles diffuse faster. b) Flow field fractionation (FFF), a parabolic laminar-flow pushes the nanoparticles. A perpendicular force is applied, which induces a gradient. Small particles diffuse more rapidly. c) Analytical ultracentrifugation (AUC), the sample solution is rotated. A centrifugal force pushes the particles towards.

Flow field fractionation (FFF) techniques split nanoparticle distributions by differential transport[85–88]. Similar to SEC, FFF makes the sample to flow along a channel, but instead of a solid phase, it applies a force to induce particle separation.

The particle solution is introduced into the channel, where a field perpendicular to the long axis pushes the nanoparticles towards one channel boundary. Figure 2.4b shows the case for a cross-flow[89,90], but other types of forces can be applied, e.g., magnetic[91] or electric[92,93]. The applied force induces a gradient, that sorts the particles according to their interaction with the field. A parabolic laminar-flow induces the particle transport along the long axis of the channel and the particles travel at different velocities due to their gradient position.

Cross-flow FFF method induces a nanoparticle gradient that depends on the hydrodynamic radius of the particles and, thus, it enables the sample division into monodisperse sample fractions. The use of calibration samples enables absolute sizing for cross-flow FFF by stablishing the relation in between the elution times and the hydrodynamic radius of the nanoparticles[4].

Analytical ultracentrifugation (AUC) yields the nanoparticles’ size-distributions and density from their sedimentation properties[94,95]. As shown in Figure 2.4c, a cuvette containing particles in suspension is rotated at high-speed. That process exerts a centrifugal force over the nanoparticles, which makes them to sediment at different rates according to their size and weight. The dynamic concentration of the solution during centrifugation is monitored, from which the particle size-distribution is obtained[96].

Despite AUC’s multimodal population characterizing capabilities, the high costs of the instrumentation and the data interpretation complexity limits the widespread adoption of the technique[4]. Moreover, AUC is an ensemble analysis method and, therefore, does not provide individual particle resolution.

Because of the different working principles of the sizing methods, for characterizing a nanoparticle dispersion we first have to choose which technique to use, attending to the sample composition and experimental needs. For instance, TEM and SEM are the best suited for high precision measurements. However, DLS is much more appropriate for routine analyses in a clinical context[97,98]. As such, every method’s suitability must be evaluated in the usage context of interest.

2.3 Optical microscopes for nanoparticle sizing

Even though optical microscopes are typically used as an imaging tool and that they possess a lateral resolution limited by the diffraction limit, they can precisely size nanoparticles much smaller than the illumination wavelength. This section aims at explaining the apparent contradiction.

First, the sizing based on the quantification of the light scattered by a particle is explained. Next, the size estimation based on the analysis of the diffusion coefficient of single particles is described. Because the present thesis work presents microscopes that use both sizing methods, significant *state-of-the-art* implementations regarding said measuring techniques are introduced in the corresponding relevant sections.

Light scattering quantification

Darkfield optical microscopes produce images that originate exclusively from the light scattered by the sample[99,100]. In consequence, when imaging a nanoparticle, the collected light shows information about its light scattering pattern.

Let us consider the intensity of the light scattered by a nanoparticle, $I(\theta,\varphi)$, at a large distance r. Angles θ and φ indicate the light propagation direction in polar coordinates. Since $I(\theta,\varphi)$ must be proportional to the incident light intensity, I_o, and r^{-2}, we may write[101]

$$I(\theta,\varphi) = \frac{I_o}{k^2r^2}F(\theta,\varphi), \tag{2.2}$$

where k refers to the wavenumber and $F(\theta,\varphi)$ is a function that indicates the scattered light propagation direction. $I(\theta,\varphi)$ is described by the Mie theory[102]. For small particles $F(\theta,\varphi)$ shows a ring-shaped pattern (Figure 2.5a), reminiscent of the dipole radiation. Large nanoparticles, however, scatter the light enhancing the propagation at certain angles[102] (Figure 2.5b), which are size dependent.

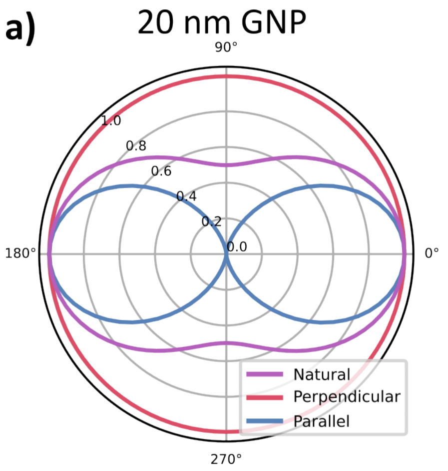

Figure 2.5, Gold nanoparticle's scattering patterns. Polar diagrams showing the Mie scattering for gold particles of 20 and 200 nm in diameter, a) and b) respectively. The incident light propagates from 180° to the centre. *Parallel* refers to the scattering pattern on the incident light's polarization plane. *Perpendicular* indicates the transversal surface. *Natural* corresponds to the average of *parallel* and *perpendicular*.

According to the Rayleigh approximation[103,104], $I(\theta)$ for a nanosphere much smaller than the incident light's wavelength is defined as

$$I(\theta) = \frac{1+\cos^2\theta}{2r^2}\left(\frac{2\pi}{\lambda}\right)^4\left(\frac{\left(\frac{n_p}{n_m}\right)^2-1}{\left(\frac{n_p}{n_m}\right)^2+2}\right)^2\left(\frac{d}{2}\right)^6 I_o, \tag{2.3}$$

where n_p and n_m refers to the refractive index of the particle and medium, respectively, λ to the wavelength and d to the particle's diameter. Note that the signal scales quadratically with the particle's volume. If we assume a size-independent $F(\theta,\varphi)$ for small nanoparticles, the collected darkfield light and d are directly proportional and, thus, the particle sizing is possible.

Figure 2.6 shows how the collected light intensity scales with d. The sixth-root plotting aims at a clear representation of the signal scaling. For small particles the collected light intensity scales as indicated in equation (2.3), that is $I(\theta) \propto d^6$. For particles outside the Rayleigh regime, however, the variations of $F(\theta,\varphi)$ affect the scattered light collection. Said effect must be considered because, depending on the microscope's configuration, large particles may exhibit decreased collected light compared to smaller ones, as shown for the backward scattering case of the simulated data shown in Figure 2.6.

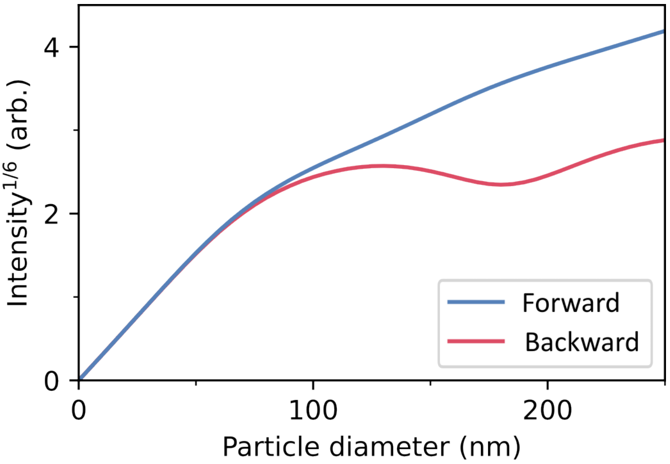

Figure 2.6, Signal scaling. Collected light intensity as a function of the nanoparticle's size for darkfield microscopes. The forward (blue) and backward (red) scattered light corresponds to transmission and reflection geometries, respectively. A gold nanosphere suspended in water, 520 nm wavelength illumination and 1.2 numerical aperture were considered for calculations.

Accurate sizing requires acquiring calibration curves that consider the experimental λ, n_p and n_m. In case of signal simulations, the Mie theory[102] must be considered for particles outside the Rayleigh regime.

The strong signal scaling related to particles' size, especially for the Rayleigh domain, leads to dramatic scattering efficiency differences for particles of similar sizes. In consequence, due to the available sensors' limited dynamic ranges, the darkfield microscopes have narrow particle-size detection windows.

Movement analysis

The capabilities of optical microscopes for sizing nanoparticles are not limited to the quantisation of the amount of scattered light. For particles is solution, their size can be extracted from inspecting their individual movement over time, which is known as nanoparticle tracking analysis (NTA)[18,19]. Contrary to DLS, NTA sizes the particles individually[98], i.e., it is not an ensemble method.

NTA records videos of particles moving, localizes them along the consecutive frames and calculates their diffusion coefficient (D). NTA converts D into particles' hydrodynamic diameter (d_H), which is usually approximated to d.

In order to obtain D, first, the mean square displacement (MSD) is calculated. The most common definition of MSD for individual particle-trajectories is given by[20]

$$MSD = \frac{1}{N-n}\sum_{i=1}^{N-n}(\vec{r}_{i+n} - \vec{r}_i)^2, \qquad n = 1, \dots, N-1 \tag{2.4}$$

where N refers the number of acquired frames, r to the particle's position in the corresponding frame and n to the spacing in between frames, which equals 1 for consecutive frames. The displacements considered in equation (2.4) are not independent from each other[105] and, thus, they are correlated. In that regard, MSD can be defined for only accounting for non-overlapping displacements, at the expense of rejecting terms[20]. However, the remainder of this chapter considers equation (2.4) for the sake of simplicity.

The MSD definition given by equation (2.4) accounts for $N - n$ displacements. In consequence, for $n \ll N$ the number of displacements is large and, therefore, MSD is well averaged and its values fulfil the theoretical expectations. For larger n values, in contrast, the number of displacements decreases and the obtained MSD estimates tent to differ from the theoretically expected values due to the poor statistics, as seen in Figure 2.7.

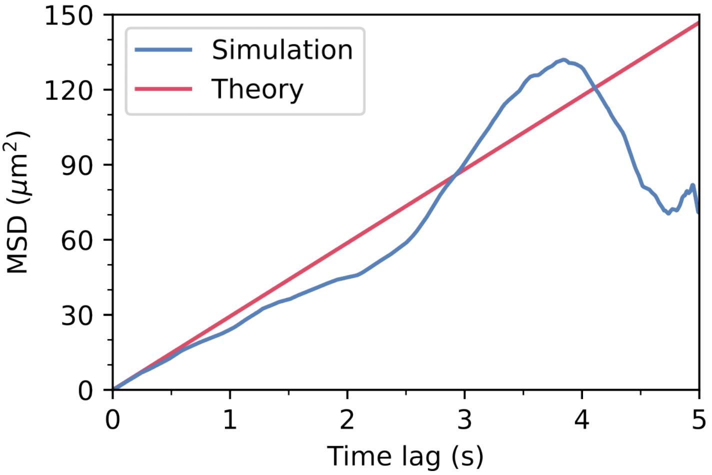

Figure 2.7, Two-dimensional MSD curve. Simulated (blue) and theoretical (red) MSD values for a 60 nm nanoparticle suspended in water at 21°C. 1000 displacements were simulated, considering 5 ms time lapses.

For a single particle-trajectory D is typically obtained by performing a linear fit to the MSD vs time curve and extracting the fit's slope. According to Einstein's classic fluctuation-dissipation formula, in the case of a two-dimensional Brownian motion of a particle[106,107]

$$MSD = 4D\Delta t, \tag{2.5}$$

where Δt is the duration of the displacement. Therefore, the slope of a linear fit equals $4D$. However, due to potential deviation in between the expected MSD values and the measured ones for large values of n, only the points related to short time lags are fitted[20,21].

Finally, d_H is calculated. The Stokes-Einstein equation[108] ,which accounts for Brownian motion, relates D and d_H as

$$D = \frac{k_B T}{3\pi\eta d_H}, \tag{2.6}$$

where k_B refers to the Boltzmann constant, T to the temperature and η to the fluid viscosity. Note that d_H refers to a rigid uncharged sphere that exhibits the same hydrodynamic behaviour as the particle under study[109], which implies that depending on the particles' nature d_H may not indicate their exact size[110,111]. Additionally, accurate sizing requires the particles to free-float in a liquid without undesired internal flows that would increase particles' D. As a consequence, the nanoparticles must be small enough to neglect the gravitational effect over the liquid-particle electrostatic interactions.

The often label-free nature of the method, resulting from recording particles' scattering signal[98,111,112], and the low solvent compatibility requirements, which mostly relate to the transparency, have contributed to the widespread adoption of NTA as a routine characterization technique. However, scattering based NTA struggles to characterize polydisperse samples due to the relation in between a nanoparticle's size and its scattering efficiency[98]. Such relation makes larger particles to mask the signal of the smaller ones. Said signal masking can be mitigated using fluorescent labels[113] at the cost of increasing the sample preparation complexity.

2.4 Summary

In summary, this chapter presents different methods for nanoparticle characterization. The particularities of each technique require a deep understanding of each of them in order to choose the best-suited one for the different research- and industrial-scenarios. The provided overview will help the reader to understand the usage scope and to appreciate the relevance of the presented holographic nanoparticle sizing platforms presented in the upcoming chapters.

In addition, the use of optical microscopy for nanoparticle sizing was introduced. In that regard, two techniques were described, one of which is based on quantifying the amount of scattered light and the other one on analysing the particles’ diffusion. The sizing platforms introduced in this thesis are based on said techniques and, therefore, their comprehension is essential for understanding their functioning.

Chapter 3:

Principles of digital holography for microscopy

In this chapter, I explain the basics of holography and its implementation onto optical microscopes. The concepts that I introduce are helpful not only for understanding the function of the holographic microscopes that I introduce on the upcoming chapters, but also for understanding the design decisions that I took for meeting the demands of the different nanoparticle samples.

Furthermore, I show how to reconstruct images from holograms, including the optical aberration correction and the digital refocusing. Those concepts are key pillars of this thesis work, as the data-analyses that I describe in the experimental sections rely on those reconstruction techniques.

3.1 Introduction

Holography is an optical imaging technique that consists on recording interference between two light waves[14–16]. One wavefront containing the information of interest is superimposed onto another one, a reference, resulting in an inference pattern called hologram. These *images* contain wavefronts' amplitude and phase information, in contraposition to the recordings obtained by common imaging systems that only capture light's intensity. Digital Holography (DH) aims at numerically retrieving the amplitude and phase information of the wavefront of interest from digitally recorded holograms[114].

DH is one of the major pillars of the present thesis work, as all the nanoparticle sizing microscope designs described in the following chapters rely on such technology. The following sections aim to introduce the principles of holography, both analogue and digital. In addition, DH's implementation into microscopy and related computational tools are discussed. Readers interested into deepening their understanding of those topics are encouraged to consult both the general[115,116] and the microscopy focused[117,118] holography bibliography.

3.2 Conventional holography

Although that DH heavily relies on modern computational capabilities, its foundations date back to late 1940s, when Dannis Gabor discovered holography aiming to improve electron microscopes' resolution[119,120]. In 1971, he was awarded the Nobel Prize in Physics based on this invention. It is very convenient to understand the *classical* holography's foundations when dealing with DH.

The essence of holography consists on recording the amplitude and the phase information of a given wavefront for reconstructing it afterwards. However, given that all sensing methods record light's intensity, the phase retrieval seems to be impossible at a first glance. To understand this apparent contradiction, let us consider two waves, the object ($\boldsymbol{O}$) and the reference ($\boldsymbol{R}$), recorded on a photographic plate (Figure 3.1a). If both waves are emitted from the same coherent light source and they spatially overlap in a sensor, they will interfere, resulting in a detected intensity, $I(x, y)$, described as[15,121,122]

$$I(x,y) = (\boldsymbol{R}+\boldsymbol{O})(\boldsymbol{R}+\boldsymbol{O})^* = |\boldsymbol{R}|^2 + |\boldsymbol{O}|^2 + \boldsymbol{R}^*\boldsymbol{O} + \boldsymbol{R}\boldsymbol{O}^*, \tag{3.1}$$

where $|\boldsymbol{R}|^2$ and $|\boldsymbol{O}|^2$ correspond to the intensities of the reference and the object waves, respectively. $\boldsymbol{R}^*\boldsymbol{O}$ and $\boldsymbol{R}\boldsymbol{O}^*$ are the interferometric terms. In order to reconstruct the recorded wavefront, the signal is recorded onto a photographic plate. A thin film is developed from the latter, so that its amplitude's transmittance is proportional to the recorded intensity. Said film is illuminated with a second reference wave ($\boldsymbol{R}'$) of the same wavelength, resulting in a transmitted light, $\psi(x, y)$, of the form of[15,121,122]

$$\psi(x, y) = \boldsymbol{R}' I(x, y) = \boldsymbol{R}'|\boldsymbol{R}|^2 + \boldsymbol{R}'|\boldsymbol{O}|^2 + \boldsymbol{R}'\boldsymbol{R}^*\boldsymbol{O} + \boldsymbol{R}'\boldsymbol{R}\boldsymbol{O}^*. \tag{3.2}$$

The above expression can be similarly divided into pure intensity and interferometric terms. The former components, called zero-order terms, are $\boldsymbol{R}'|\boldsymbol{R}|^2$ and $\boldsymbol{R}'|\boldsymbol{O}|^2$ and do not affect the propagation direction of $\boldsymbol{R}'$. The latter terms, named twin-images, are $\boldsymbol{R}'\boldsymbol{R}^*\boldsymbol{O}$ and $\boldsymbol{R}'\boldsymbol{R}\boldsymbol{O}^*$, which, in contrast, do modify the path of $\boldsymbol{R}'$ due to the diffraction caused by the interferometric terms of $I(x, y)$. Figure 3.1b shows the wavefront propagation of $\boldsymbol{R}'\boldsymbol{R}^*\boldsymbol{O}$ and $\boldsymbol{R}'\boldsymbol{R}\boldsymbol{O}^*$, simplified to $\boldsymbol{O}$ and $\boldsymbol{O}^*$ respectively. The former component forms a replica of the encoded wavefront, i.e. an observer would see a virtual image of the information contained on it. The latter term projects a real conjugate image, meaning that the depth perception is reversed.

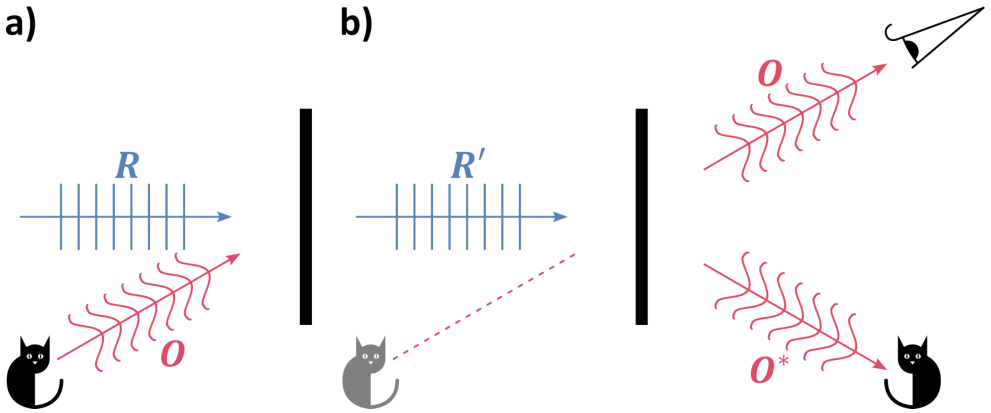

Figure 3.1, Classical holography. a) Recording of a hologram in the *off-axis* configuration. b) Illuminating the hologram from (a) reconstructs the encoded wavefront.

3.3 Digital holograms in optical microscopy

Compared to conventional photographic plates, digital cameras encode $I(x, y)$ into a numerical array by quantifying signal's intensity and spatial values, which enables numerical computation[123]. The paragraphs below explain how to record digital holograms and how to decode their information.

Let us consider equation (3.1) as the recorded signal. We can further develop $I(x,y)$ in terms of intensity and phase, assuming collinear $\boldsymbol{R}$ and $\boldsymbol{O}$, as[122]

$$I(x,y) = I_R + I_O + 2\sqrt{I_R I_O}\cos(\varphi_R - \varphi_O), \tag{3.3}$$

with I_R, I_O, φ_R and φ_O corresponding to the intensities and phases of $\boldsymbol{R}$ and $\boldsymbol{O}$, respectively. All those terms are in function of (x,y) because they reflect the 2D projection of $\boldsymbol{R}$ and $\boldsymbol{O}$ onto the camera's chip plane. Assuming that we know the phase and amplitude information of the reference wave, we can see the interferometric contributions, $2\sqrt{I_R I_O}\cos(\varphi_R - \varphi_O)$, as a way to encode the object's wave phase.

Figure 3.2 shows a microscope implementation in the transmission geometry[99] where $\boldsymbol{R}$ and $\boldsymbol{O}$ are collinear. In such microscope, the light non-scattered by the sample constitutes the reference wave and interferes with the object. We refer to these configurations where both waves share the optical path as *in-line* holography[124–126]. In microscopy, *in-line* implementations are often referred as interferometric scattering (iSCAT)[127] or coherent brightfield (COBRI)[10] for reflection and transmission illumination geometries, respectively.

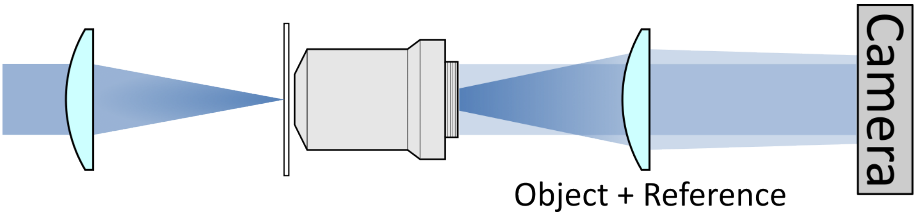

Figure 3.2, *In-line* configuration. The object and reference, the non-scattered light, waves share the optical path. The sample is illuminated in a transmission geometry.

The overlap of I_R, I_O and the interferometric terms on *in-line* holograms makes accessing φ_O complicated[128]. Instead, the spatial intensity modulation associated to the interference of two non-collinear waves enables the terms to decouple[129]. Now, let us consider $\boldsymbol{R}$ and $\boldsymbol{O}$ to reach the camera with a relative angle of θ, which is known as *off-axis* holography[126,128]. Here, the intensity at the detector is described by[15,122]

$$I(x,y) = I_R + I_O + 2\sqrt{I_R I_O}\cos\left(\frac{2\pi}{\lambda}(x+y)\sin\theta + \varphi_R - \varphi_O\right), \tag{3.4}$$

where λ refers to the waves' wavelength while x and y correspond to the position on the detector across x- and y-axes, respectively. The interference between $\boldsymbol{R}$ and $\boldsymbol{O}$ in *off-axis* configurations leads to a phase gradient over the detector's plane, which induces interferometric fringes across the whole recorded image, as shown in Figure 3.3.

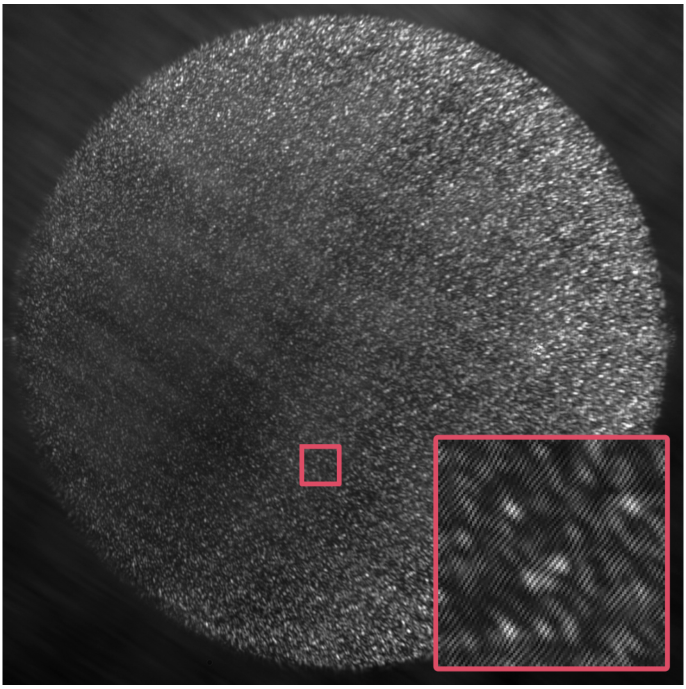

Figure 3.3, Digital hologram. An example of a recoded interferogram corresponding to an *off-axis* configuration with a diagonal phase gradient. The inset shows a detailed view of the interference fringes. The intensity is capped for representation-purposes.

Figure 3.4 shows a holographic microscope in the *off-axis* configuration. Conceptually, it is a darkfield[99,100,130] microscope in the transmission geometry that projects a second wave, the reference, onto the sensor for interfering with the sample image, the object. The darkfield mask blocks the light of the object wave not scattered by the sample for avoiding the interference of collinear beams.

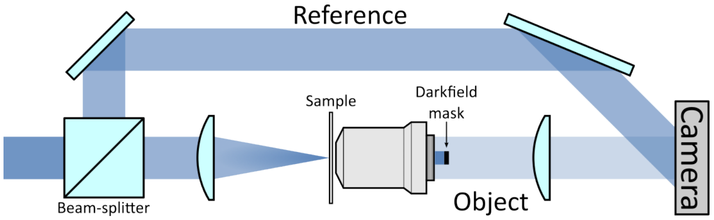

Figure 3.4, *Off-axis* configuration. A beam-splitter produces two waves, the object and the reference. The former propagates through a typical darkfield microscope, in a transmission geometry. The latter is directly projected onto the camera.

Compared to *off-axis* designs, the interference of *in-line* configurations tends to be more stable[128], because both waves are phase-matched and their optical-path lengths are equal, which minimizes the negative effect of vibrations. However, the phase gradient across *off-axis* holograms leads to an easier phase retrieval and allows wavefront modification techniques[131]. We focus on *off-axis* configurations for the rest of the chapter.

Equation (3.4) can be simplified by subtracting I_R, which is easily done by recording an image containing just the reference wave as that wave is considered to be constant over time. In addition, we can reject the $\sqrt{I_R}$ dependence from the interferometric terms by dividing the image by said term, which removes the spatial modulation induced by the reference wave's potential inhomogeneities. The resulting signal, $I'(x,y)$, is described as

$$I'(x,y) = \frac{I_O}{\sqrt{I_R}} + 2\sqrt{I_O}\cos\left(\frac{2\pi}{\lambda}(x+y)\sin\theta + \varphi_R - \varphi_O\right). \tag{3.5}$$

In terms of signal components, the previously mentioned interferometric fringes are part of the interferometric terms and, thus, these components are spatially modulated. The zero-order component, $I_O/\sqrt{I_R}$, does not contain any interference information and, therefore, is not affected by said spatial modulation. Applying a Fast Fourier Transform (FFT) to $I'(x,y)$ decomposes the signal into its spatial frequency components[132,133]. Due to the spatial modulation, the interferometric terms are shifted with respect to the zero-order component, which is located in the spatial low frequency domain. Interestingly, the shift occurs in opposite directions for each interferometric component due to their conjugate nature. Figure 3.5 shows the FFT signal decomposition of hologram from Figure 3.3. The decoupled interferometric terms are often referred as twin-images[134].

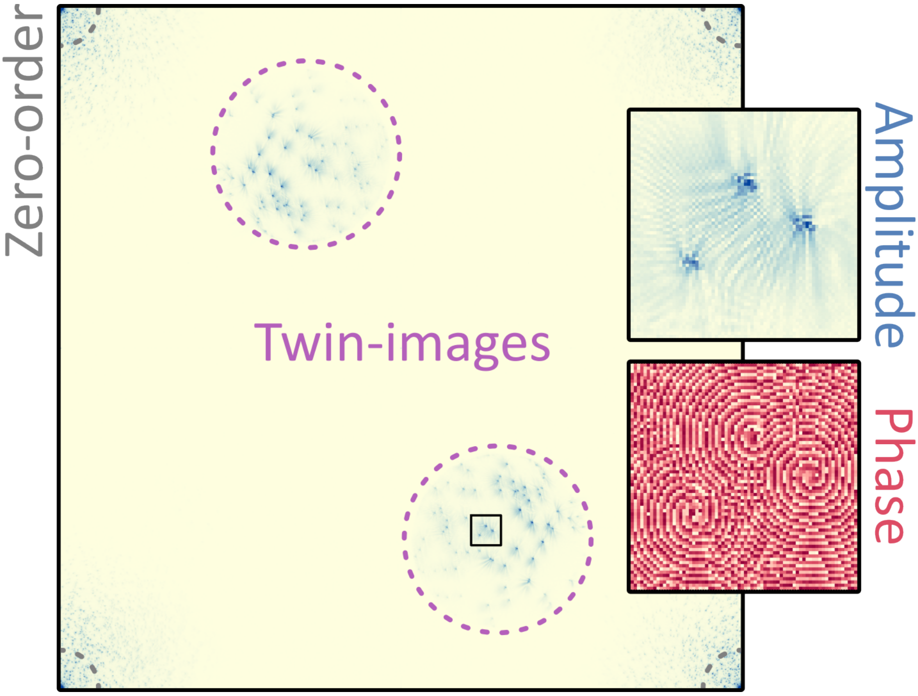

Figure 3.5, Signal decomposition. An FFT decouples the terms corresponding to the zero-order and the twin-images. The latter components correspond to 80 nm gold nanoparticle darkfield images. The insets show the magnified amplitude and phase components of the framed area. The intensity is capped for representation-purposes.

Assuming that φ_R is known, equation (3.5) indicates that the twin-images fully describe the wavefront of $\boldsymbol{O}$. For that reason, a twin-image crop enables the $\boldsymbol{O}$ wavefront extraction. Note that the twin-images are symmetric with respect to the horizontal and vertical axes, i.e. they contain the exact same information, including identical noise.

Interestingly, we can convert the real-space representation of the extracted wavefront into a *k*-space one and vice versa without information loss by applying an FFT[132,133], as shown in Figure 3.6. In other words, whether $\boldsymbol{O}$ is encoded onto the hologram in either of these representations leads to the same recovered wavefront.

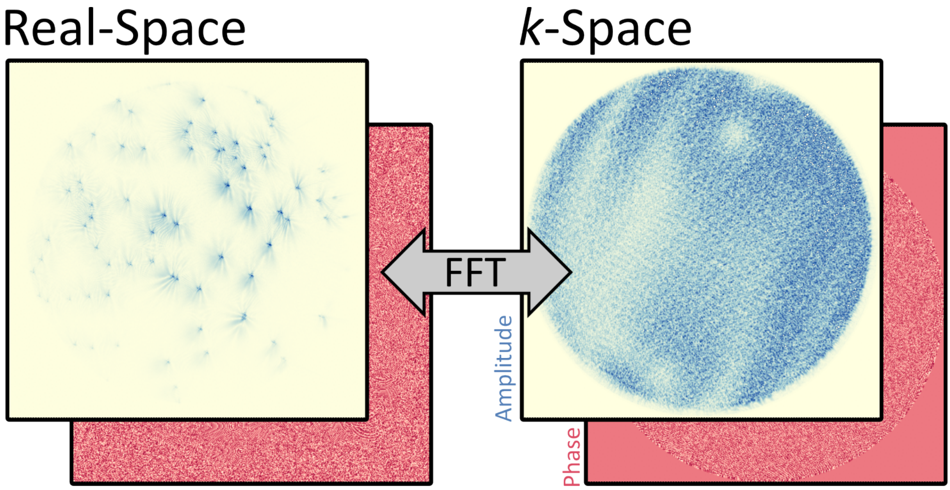

Figure 3.6, Reconstructed wavefront. Both amplitude and phase information are retrieved. An FFT converts the real-space representations of the wavefront (right) into their *k*-space counterparts (left) and vice versa. The signal corresponds to 80 nm gold nanoparticles' darkfield scattering. The amplitude is capped for representation-purposes.

3.4 Experimental implementation of *off-axis* microscopes

When designing a holographic microscope, understanding the effect of both the phase ramp induced by θ and the camera's sampling on the wavefront reconstruction is of paramount importance and not straightforward. The paragraphs below aim at explaining how we can tune those parameters for implementing the twin-image and zero-order layout of Figure 3.7, that is an identical radius for the mentioned components corresponding to one sixth of the diagonal axis of the resulting image and no term overlap.

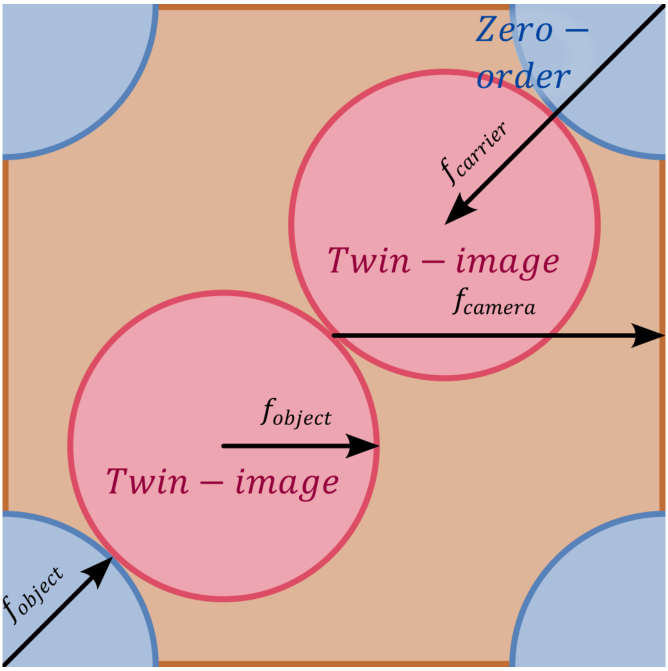

Figure 3.7, Diagonal twin-image shift. The twin-images and the zero-order have the same radius, f_{object}. The twin-images are shifted from the zero-order by $f_{carrier}$, where $f_{carrier}$ corresponds to half-image side.

In Figure 3.7, the zero-order and the twin-images are equal in size, which according to equation (3.5) indicates that $I_O \sim I_R$. In addition, because the twin-images do not depend on I_R, we can define their size as the spatial frequency low-pass of $\boldsymbol{O}$, f_{object}. Considering Nyquist sampling, f_{object} is related to the camera's spatial frequency bandpass, f_{camera}, as[122]

$$f_{object} = \frac{\sqrt{2}}{3} f_{camera} = \frac{N}{3\sqrt{2}\delta p}, \tag{3.6}$$

where N refers to the detector's pixel row number and δp to the pixel size.

The carrier frequency ($f_{carrier}$), which refers to the spatial modulation that induces the shift when an FFT is applied to the hologram, depends on θ. For the particular case of Figure 3.7, in which $f_{carrier} = 2f_{object}$ and the phase gradient expands diagonally, θ is defined as

$$\theta = \arcsin\frac{\lambda}{3\sqrt{2}\delta p},$$

(3.7)

However, f_{camera} limits the maximum angle, θ_{max}, at which the interference fringes are correctly sampled. Considering Nyquist sampling and a diagonal phase ramp, the maximum angle, θ_{max}, is defined as[121,122]

$$\theta_{max} = \arcsin\frac{\lambda}{2\sqrt{2}\delta p}.$$

(3.8)

Note that the value of θ_{max} depends on the phase ramp direction. When $\theta > \theta_{max}$, applying an FFT leads to corrupted images. For $\theta \leq \theta_{max}$ inadequate values of θ typically require reducing f_{object} for avoiding the twin-images and the zero-order term to overlap.

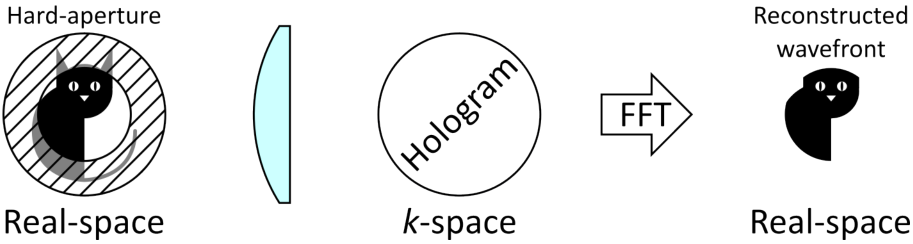

Figure 3.8, Adjustment of the twin-image size. Adding a hard aperture in the image plane crops the reconstructed wavefront.

We can experimentally tune f_{object} by adding a hard aperture on the image plane that corresponds to the reconstructed wavefront (Figure 3.8). When the image on the hologram plane corresponds to a real-space representation, the numerical aperture (NA) limits the twin-image size. Small twin-images are often desired for their ease of experimental implementation. However, low f_{object} values compromise the lateral resolution (r) of the reconstructed image, which is defined as[122]

$$r = \frac{FoV}{f_{object}} = \frac{N\delta p}{M \cdot f_{object}},$$

(3.9)

where FoV refers to the field-of-view and M to the optical system's magnification. The case of Figure 3.7, leads to

$$r = \frac{3\sqrt{2}\delta p}{M}. \tag{3.10}$$

When applied to microscopy, it is convenient to set δp and M so that the resulting r is equal or lower to the system's diffraction limit.

Regarding the twin-image isolation, the cropped image may contain portions of the zero-order and the other twin-image, as shown in Figure 3.9. In such cases, we may apply a digital mask to remove those signal portions.

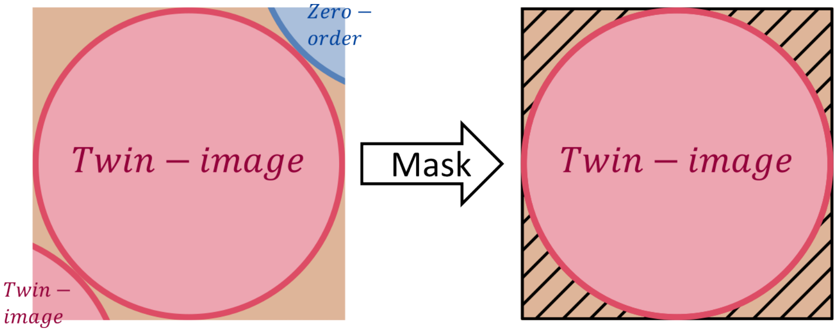

Figure 3.9, Twin-image isolation. An interferometric term is cropped (right) and a digital-mask (left) removes any unwanted signal.

Finally, due to DH's ability to convert real-space wavefront representations into k-space ones and vice versa, recording the back-focal-plane (BFP) of a microscope gains especial interest. When dealing with such optical configurations, matching the size of the BFP image and the camera's chip is convenient. Otherwise, the effective N and, thus, f_{object} are reduced. BFP's diameter is defined as[135]

$$BFP_{diameter} = \frac{2 \cdot NA \cdot l_{tube\ lens}}{M}, \tag{3.11}$$

where $l_{tube\ lens}$ refers to the focal length of the tube lens. Equation (3.11) helps us setting an appropriate relay system for optimizing the BFP's image size.

3.5 Optical aberration correction

One key tool of DH is the optical aberration correction[131], which enables mitigating the image quality losses related to the use of low-quality optical elements or system's misalignments. The paragraphs below explain how we can correct the optical aberrations of a reconstructed wavefront that originated from diffraction limited light sources.

Optical aberrations must be characterized for their removal, which in microscopy is usually done by analysing the point-spread-function (PSF)[132,136]. The PSF refers to the image of a point source. For an ideal optical system that images a point source placed at infinity, or that uses infinitive corrected lenses, the PSF's shape is a diffraction limited Airy disk and its phase is constant over the *k*-space. In consequence, we can characterize the optical aberrations of a microscope using infinitive corrected lenses by analysing the darkfield *k*-space emission pattern of a point source.

Let us consider the reconstructed real-space wavefront of Figure 3.6, which consist of a darkfield image of nanoparticles that are smaller than the system's diffraction limit and, thus, point sources. Figure 3.10 shows how to decode the aberrations by characterizing the PSF.

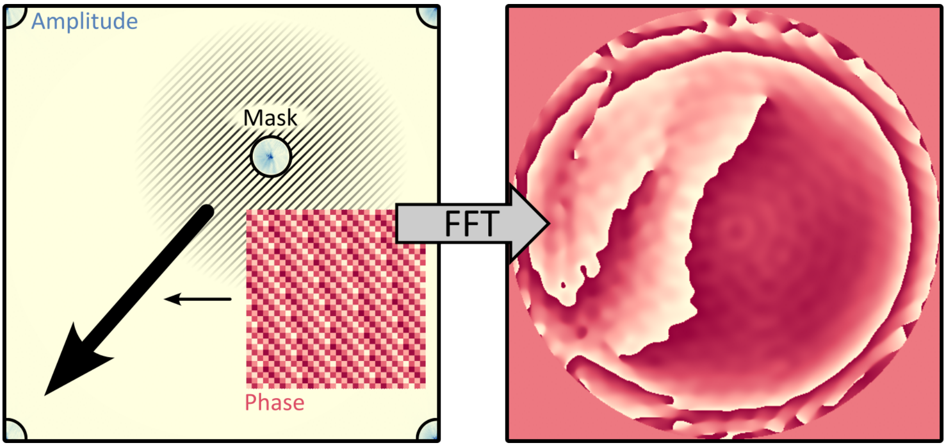

Figure 3.10, Error phase extraction. A digital mask isolates a point emitter. A phase ramp is applied in the *k*-space. The emitter position is shifted to (0,0). An FFT shows the *k*-space representation of optical aberrations. The emitter is an 80 nm gold nanoparticle. The amplitude is capped for representation-purposes.

First, a digital mask isolates one particle, conveniently in the centre of the FoV. Considering the angular spectrum method (ASM)[137,138], we can relate a wavefront, $E(x, y)$, and its plane-wave components, $A(k_x, k_y)$, with

$$A(k_x, k_y) = \mathcal{F}\{E(x, y)\};$$

(3.12)

with $\mathcal{F}$ being the Fourier transform. We now define the isolated PSF as $E(x, y)$ and we shift it from the image's centre to one corner by

$$E_o(x, y) = \mathcal{F}^{-1}\{A(k_x, k_y) \cdot R(k_x, k_y)\},$$

(3.13)

where $E_o(x, y)$ corresponds to the resulting image and $R(k_x, k_y)$ to a phase ramp function. The latter being

$$R(k_x, k_y) = e^{-i(k_x + k_y)},$$

(3.14)

where k_x and k_y correspond to the discretised spatial frequencies for the x- and y-axes, respectively. We define k_x and k_y as

$$(k_x, k_y) = \frac{2\pi(x, y)}{\delta p_M N_R};$$

(3.15)

with δp_M, N_R, x and y referring to the magnified pixel size, the reconstructed wavefront pixel length and the initial position of the point emitter in the real-space for x- and y-axes, respectively. The resulting PSF phase (φ_{E_o}), k-space representation shown in Figure 3.10 right, indicates the wavefront's optical aberration. In consequence, we can define the function inducing the optical aberrations, the distortion function, $D(k_x, k_y)$, as

$$D(k_x, k_y) = e^{-i\varphi_{E_o}}.$$

(3.16)

Interestingly, we can use $D(k_x, k_y)$ for removing the optical aberrations. If we consider an aberrated object wave, $O_A(x, y)$, the corresponding distortion-free wave, $O(x, y)$, can be obtained by

$$O(x, y) = \mathcal{F}^{-1}\left\{\frac{\mathcal{F}\{O_A(x, y)\}}{D(k_x, k_y)}\right\}.$$

(3.17)

Equation (3.17) requires $O_A(x,y)$ and φ_{E_o} to be generated form the same imaging system. However, once $D(k_x, k_y)$ is set it can be applied to all recorded holograms as long as the optical paths of neither $\boldsymbol{O}$ nor $\boldsymbol{R}$ are modified. Moreover, $O_A(x,y)$ and φ_{E_o} can be acquired from the same hologram.

Figure 3.11 shows the reconstructed wavefront of Figure 3.6 before and after removing the optical aberrations, left and right respectively. Both $O_A(x,y)$ and φ_{E_o} were acquired from hologram of Figure 3.3.

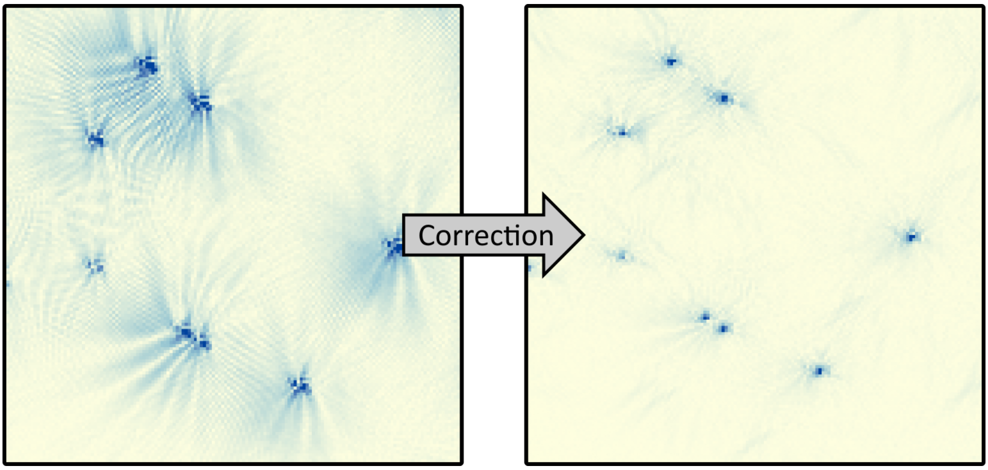

Figure 3.11, Optical aberration removal. Comparison of 80 nm gold nanoparticle darkfield images before and after removing the optical aberrations, left and right respectively. The amplitude is capped for representation-purposes.

In case of low signal-to-noise scenarios, φ_{E_o} can be averaged from many different point emitters or it can be calculated by fitting Zernike polynomials[139] in the *k*-space domain. The latter case is especially relevant because it enables decomposing the aberrations into different types by analysing the contribution of each polynomial.

3.6 Digital propagation

DH tools take advantage of the phase retrieval and the related wavefront propagation for digitally refocusing images[131] (Figure 3.12). In microscopy, digitally accessing the third spatial dimension is especially relevant when dealing with dynamic events, as the ability to project a 3D representation from a single 2D image avoids the need for time-consuming axial-scans[140].

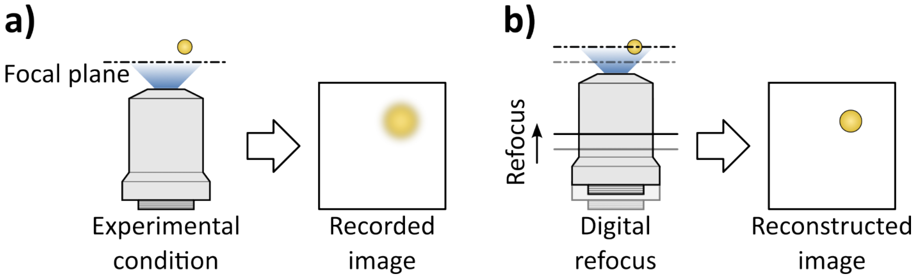

Figure 3.12, Digital refocusing. a) A particle out of the focal plane is recorded, which results in a blurry image. b) The image from (a) is digitally refocused, which equals to physically moving the imaging lens, yielding a sharp depiction.

We can propagate a complex wavefront along the optical axis by employing the ASM[137,138,141]. Let us consider the plane wave components of the reconstructed wavefront at a system's physical focal plane as $A_f(k_x, k_y)$. According to ASM, the propagated wavefront, $E(x, y, z)$, is obtained by

$$E(x,y,z) = \mathcal{F}^{-1}\left\{A_f(k_x,k_y)e^{-iz\sqrt{k_m^2-k_x^2-k_y^2}}\right\}, \tag{3.18}$$

where z corresponds to the propagated distance and k_m to the wave number. The latter is defined as

$$k_m = \frac{2\pi n}{\lambda}, \tag{3.19}$$

with n referring to the refractive index of the medium.

Figure 3.13 shows a reconstructed image before (left) and after (right) the digital refocus. The wavefront was propagated for 58 µm, which demonstrates that holography enables reconstructing the 3D signal of a sample over several micrometres without physically moving parts, as mentioned above.

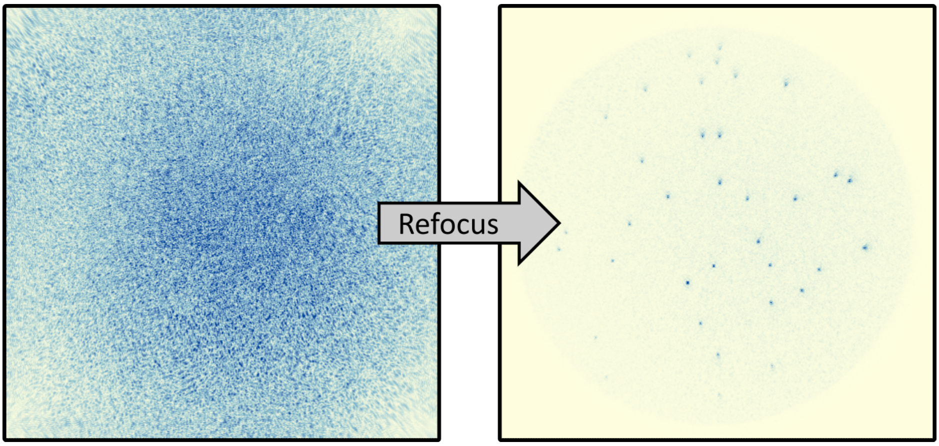

Figure 3.13, Digital refocus. An image showing fixed 80 nm gold nanoparticles, before (left) and after (right) digital refocus. The signal was recorded in a darkfield configuration and the wavefront was propagated over 58 µm.

3.7 Summary

In summary, this chapter explained the working-principle of both the digital and the conventional holography. In addition, the implementation of DH onto optical microscopes was discussed, by analysing the so called *in-line* and *off-axis* configurations and the benefits of the latter with respect to the light's phase retrieval.

In order to understand the design decisions taken regarding the holographic platforms introduced in the upcoming chapters, a thorough explanation about the experimental implementation of microscopes in the *off-axis* configuration was provided. Moreover, said explanation will help the reader in successfully replicating the presented setups and in designing new ones.

Finally, this chapter shows how to reconstruct images from holograms and how to employ DH's tools for their digital *a posteriori* processing. In that regard, the optical aberration correction and digital refocusing was explained. Such concepts are essential for understanding the data-analyses described in the experimental sections.

Chapter 4:

Precise nanosizing of heterogeneous nanoparticle populations by high-dynamic range sensing

Optical sensing is one of the key enablers of modern diagnostics. Especially label-free imaging modalities hold great promise as they eliminate labelling procedures prior to analysis. However, scattering signals of nanometric particles scale with their volume square, which makes it extremely difficult to quantitatively characterize intrinsically heterogeneous clinical samples, such as extracellular vesicles, as their signal variation easily exceeds the dynamic range of currently available cameras. Here, we introduce off-axis k-space holography that circumvents this limitation. By imaging the back-focal plane of our microscope, we project the scattering signal of all particles onto all camera pixels, thus dramatically boosting the achievable dynamic range to up to 110 dB. We validate our platform by detecting and quantitatively sizing metallic and dielectric particles. Additionally, we present quantitative size distributions of extracellular vesicle samples.

Parts of this chapter have been adapted from the following publication: Ortiz-Orruño, U., Jo, A., Lee, H., van Hulst, N. F., and Liebel, M., *Nano Lett.* **2021**, 21, 1, 317–322 and are copyright (2020) by American Chemistry Society. Most of the work presented was performed by myself apart from extracellular vesicle extraction and purification, which was performed by Ala Jo and Hakho Lee.

4.1 Introduction

Diagnostics is key to detecting, quantifying and, ultimately, curing diseases. A very important aspect of modern diagnostics is to provide rapid identification of a medical condition at the highest possible sensitivity[142–144]. Ideally, a novel platform yields quantitative results that allow taking necessary measures to prevent the spread of any infectious disease or to commence a suitable treatment before non-reversible conditions develop. Numerous potential techniques for providing rapid diagnostics are based on label-free detection[145–151], which eliminates the need for sample labelling prior to analysis, thus dramatically reducing the overall time needed.

An extremely promising approach to robust particle quantification is digital holography, due to its label-free characterization capabilities. For macroscopic samples, such as tissue or cell populations, holographic lensless imaging can provide diffraction limited resolution, over millimetre-sized field-of-views, thus paving the way towards next-generation point-of-care devices[152,153]. On the nanoscale, lens-based *in-line* holography[5,154] enables high-speed observations, in the hundreds of kilohertz range, and highly-sensitive label-free particle size estimation[12,13,155,156]. However, as these techniques rely on light scattering, a big challenge is the dramatic scaling of the scattering signal with particle size[103,104].

This dependence is especially problematic for heterogeneous biological samples, such as extracellular vesicles (EVs)[22–24], or exosomes, which are promising biomarkers for future liquid biopsy implementations. This interesting class of bioparticles typically spans diameter-ranges of, approximately, 20-250 nm[157,158]. Label-free EV characterization protocols suffer various limitations in this regard[159], and three major approaches: dynamic light scattering[64,65], nanoparticle tracking analysis (NTA)[18,19] and tuneable resistive pulse sensing[73,74], all struggle with heterogeneous samples[160–162]. Alternative approaches, such as optical fibre-based sensing[163] and micro-resonators[164] may be appropriate to overcome this heterogeneity-problem but their cost and low throughput currently prevents applications in routine analysis on a day-to-day basics.

In this chapter I introduce an *off-axis* microscope, named *k*-scope, and I demonstrate that it effectively sizes EV samples by showing proof-of-concept measurements. In addition, I provide a signal stability analysis and I detail the microscope's calibration in order to validate the mentioned EV characterization.

4.2 Theoretical considerations

Even though our daily intuition suggests that it should be trivial to, simultaneously, observe objects whose diameter differs by approximately twenty, on the nanoscale this intuition fails dramatically. From Chapter 2 we know that in the Rayleigh regime, a particle's scattering amplitude scales with its volume, V, and, thus,

$$I_{sca} \propto V^2 \propto d^6, \tag{4.1}$$

where I_{sca} refers to the scattered light's intensity and d to the particle's diameter.

In other words, the scattering signal difference between a, for example, 10 nm and a 200 nm particle is $20^6 \sim 10^8$, if we assume the Rayleigh regime. As a result, darkfield based quantification, that relies on blocking the illumination wave and detecting scattered light[99,100], of said particle range is extremely challenging and widefield imaging is outright impossible as currently available cameras do not cover the required dynamic range.

Figure 4.1 illustrates said issue by showing the expected images for a sample containing particles with relative radii of 1 and 10. As seen in Figure 4.1a, when the integration time of the camera is set to detect the larger nanoparticles, the smaller particles' signal is lost below the detection threshold due to the dynamic range limit of the camera. In contrast, when the integration time is set to detect the small particles (Figure 4.1b), the larger ones locally saturate the camera.

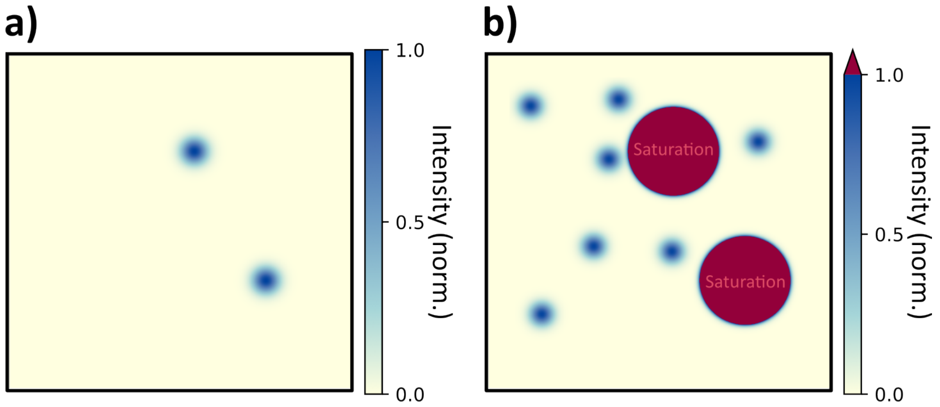

Figure 4.1, Darkfield images of nanoparticles at different integration times. a) Simulation of a darkfield image of a sample containing nanoparticles with diameters of 10 nm and 200 nm. The Rayleigh scattering regime was considered, which implies a signal difference of $\sim 10^8$ between both particles. The camera's integration-time is set to image the larger nanoparticles (dotted circles). The smaller ones are invisible (dashed circles) due to the dynamic range that was determined for the camera (40 dB). Shot-noise was not considered. b) Same simulation as before, but the integration time is set to image the smaller nanoparticles. In consequence, the strong scatterers saturate the camera.

Holographic approaches mitigate some of the problems as they allow signal amplification in a typical heterodyne-fashion, by interfering the scattered light, I_{sca}, with a reference wave, I_R. As a result, there is no need for unrealistically low detector dark-counts. From Chapter 2 we know that the recorded holographic signal, I_{hol}, can be described as[122]

$$I_{hol}(x,y) = I_R + I_{sca} + 2\sqrt{I_R I_{sca}}\cos(\Delta\varphi), \tag{4.2}$$

where $2\sqrt{I_R I_{sca}}\cos(\Delta\varphi)$ is the interference term, which depends on the phase difference, $\Delta\varphi$, between I_R and I_{sca}. In the limit of strong particle scattering, $I_{sca} \gg I_R$, we essentially recover darkfield behaviour and equation (4.2) simplifies to (1). Figure 4.2a compares the holographically obtained intensity, for two different reference-wave amplitudes, to the volume-square limit discussed above.

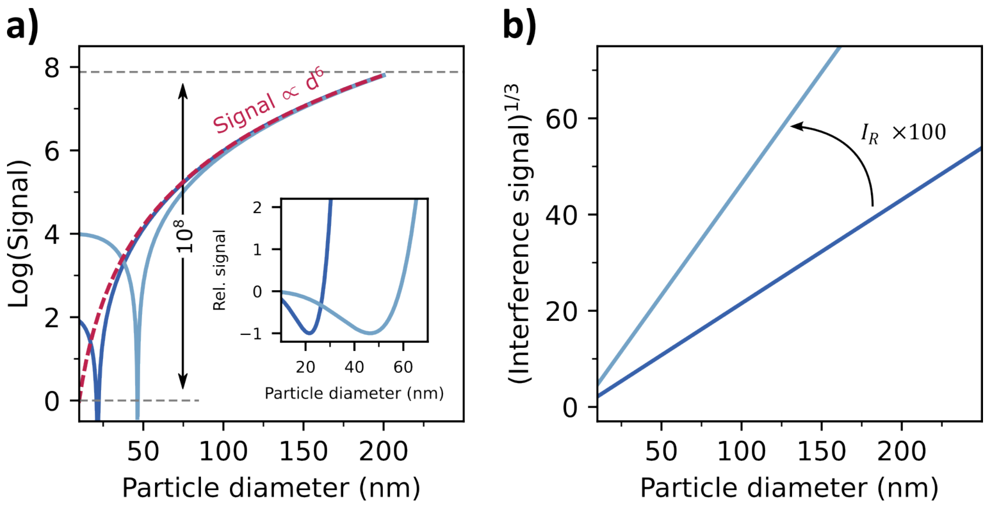

Figure 4.2, Signal scaling at the nanoscale. a) LogLinear representation of the particle-diameter dependent holographic signal intensities for different reference amplitudes (solid) assuming *in-line* detection, an I_R to I_{sca} phase-shift of π and the Rayleigh scattering emission regime. The dashed curve describes the limit of $I_R \rightarrow 0$, which is equivalent to darkfield detection. The inset shows the normalised signal intensities around $I_{sca} \approx I_R$ as $I_{hol}/I_R - 1$, on a linear scale, to highlight the signal ambiguity problem. b) Third-root representation of the isolated interference terms from the holographic signals shown in a).

Even though the total signal shows reference-wave dependent differences, the absolute signal variation remains, essentially, unaltered close to the factor of approximately 10^8 for darkfield scattering. Furthermore, the simultaneous detection of both the amplitude square and the interference terms results in particle-size ambiguities as different diameters exhibit the same signal (Figure 4.2a, inset).

Isolating the interferometric terms of I_{hol} would avoid those particle-size ambiguities and, additionally, maintain particles' signal amplification. Here is where *off-axis* configurations[121,165] come into play. As described in Chapter 2, those configurations modulate the interferometric terms in a way that Fourier transforming the hologram decouples them from the other signal terms[132,133]. As a result, the amplified particles' signal is isolated.

Figure 4.2b shows the scaling of an isolated interferometric term with respect to particles' size for two different reference-wave amplitudes. There is no particle-size ambiguity because the illumination beam does not act as a reference wave.

We can implement darkfield imaging systems either by blocking the illumination wave or by avoiding its collection by the imaging lens. The former case, shown in Figure 4.3a, consists on adding a beam-stop in the centre of the back-focal-plane (BFP) of the microscope objective[100,130]. Because the unscattered wave is restricted to the low spatial frequency domain, the stop blocks said wave. However, the beam-stop also blocks a portion of the signal of interest. Additionally, the need of blocking potential parasitic back-reflections may require larger beam-stops, which increases the signal loss.

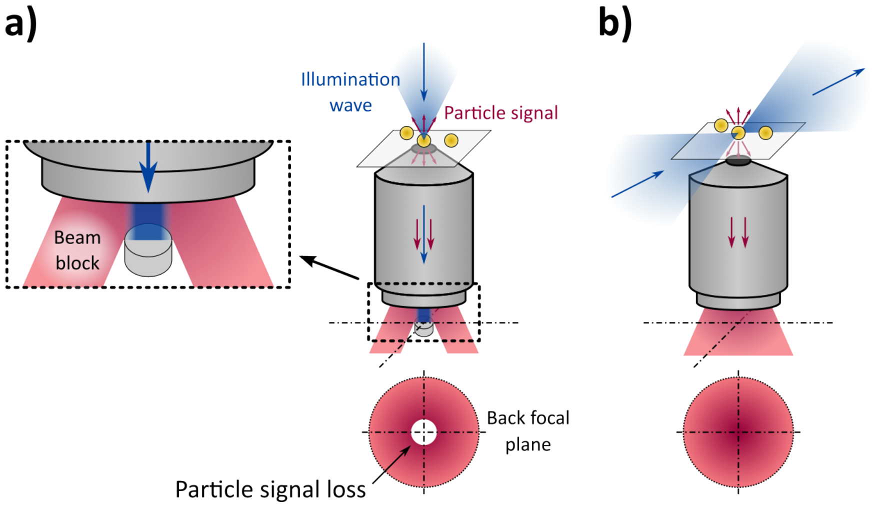

Figure 4.3, Darkfield imaging. a) Beam-stop based implementation. A perpendicular incoming wave illuminates the nanoparticle sample. The imaging lens collects both the scattered and the unscattered light. A beam-stop, placed in the back-focal-plane, blocks the illumination wave and the low spatial frequency components of the particles' signal. The inset shows a magnification of the bema-stop. b) Oblique illumination based implementation. A non-perpendicular wave illuminates the particles. Only the light scattered by the particle is collected.

Darkfield implementations based on oblique geometries for sample illumination avoid the signal loss described above. As shown in Figure 4.3b, said implementations do not collect the unscattered wave as long as the incident wave reaches the sample in an angle greater than the imaging lens's numerical aperture (NA). Hence, these configurations do not block any scattering signal fraction. Moreover, oblique illuminations enable very large field-of-views, which are difficult to achieve in through-objective configurations due to parasitic back-reflections that contaminate the signal of interest.

Isolating the signal of interest, however, is not enough for effectively imaging particles in the sub-wavelength regime. As shown in Figure 4.1, darkfield microscopes struggle to characterize polydisperse samples. Fourier imaging, which consists of recording a *k*-space plane of an optical system, is especially relevant for this regard. When imaging diffraction limited objects, their signal spreads over the *k*-space plane within NA[17] (Figure 4.4) and, therefore, the light is projected onto more camera pixels. Hence, it dramatically increases the dynamic range of imaging systems, as it scales up to what would be achievable by using the entire detector as a single pixel.

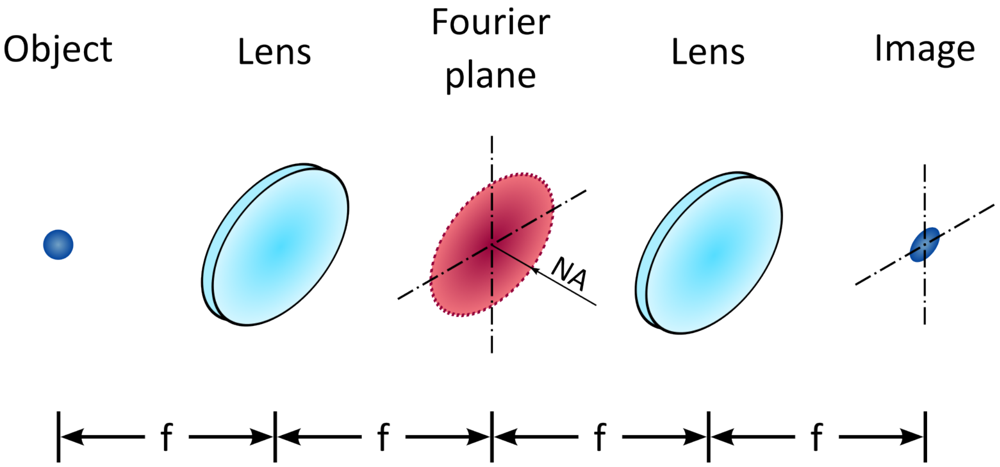

Figure 4.4, 1:1 optical relay system. A nanoparticle is imaged using a 2-lens system. The focal length of both lenses is f. At a distance of $4f$, the image of the nanoparticle is projected. At $2f$, the Fourier plane is located, which contains a *k*-space representation of the nanoparticle. The scattering signal of the nanoparticle is spread over this plane within lens NA limit (doted circle).

Finally, in terms of day-to-day use, a high particle throughput is strongly desirable for an efficient sample characterization. *Off-axis* holographic configurations are compatible with large field-of-views and, consequently, enable the necessary statistics that quantitative observations require.

4.3 Setup

We implement a microscope, the *k*-scope, that meets the signal and throughput characteristics describes above. Said microscope relies on *off-axis* interference between a reference wave and a *k*-space representation of the sample[166,167], that is, it interferes a reference wave with an image of the BFP of the microscope objective. Once detected, computational Fourier processing allows recovering a real-space darkfield image of the sample. Once processed, our recordings are equivalent to common real-space images, albeit at a dramatically increased dynamic range where the improvement is directly proportional to the total number of camera pixels. A 10-megapixel CMOS camera, with an intrinsic dynamic range of 40 dB, can thus be boosted to 110 dB.

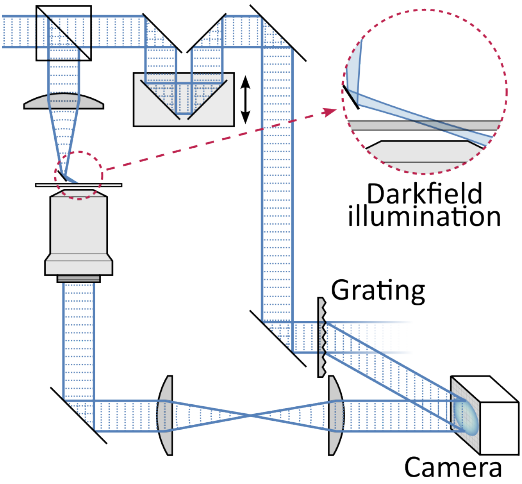

Figure 4.5, Schematic of the *k*-scope. The *off-axis* holographic microscope employs a grating to match the phase-front and a delay-line to match the optical path. The parallel blue lines indicate the phase-front of the beams. The inset shows a magnification of the darkfield-mask free collection configuration.

Figure 4.5 shows a schematic of our *k*-scope where a beamsplitter generates both illumination and reference fields from a diode laser centred at 520 nm (*LDM-520-100-C, Lasertack*). The former illuminates the sample under an oblique illumination configuration (Figure 4.5, inset). A microscope objective (*Mitutoyo MY100X-806*, NA=0.7) collects the sample scattering and a relay imaging system, with a 3.5x magnification, images the objective's BFP onto a camera (*acA2040-90um, Basler AG*) where it interferes with the reference wave in an *off-axis* configuration. We, furthermore, use a mechanical delay-line and a grating to ensure maximum interference contrast over the entire detector which is necessary due to the <100 µm coherence length of our laser. While the delay-line matches the optical path lengths for maximizing the interference, the grating allows generating a reference wave phase-front that is parallel to the detector plane. This adjustment of time delay and grating is only necessary for some, non-stabilised, diode lasers which might exhibit surprisingly short temporal coherence lengths, as the <100 µm of our laser. Diode pumped solid state lasers, however, do not require adjustments, as long as the path length difference is kept within a few tens of centimetres, which considerably simplifies the experimental setup.

Aiming at increasing the signal-to-background ratio of the analytes, we use mica sheets (V1 grade 0.15-0.21 mm thickness, *Micro to Nano*) as sample holders. Cleaving those sheets provide smooth surfaces with low scattering efficiencos[168], which reduces the scattering background compared to glass cover slides and, thus, facilitates the characterization of nanoparticles.

4.4 Data analysis

Figure 4.6 left shows an as-detected camera image obtained for a sample containing 20 nm diameter gold nanoparticles (GNPs) that we illuminate at 520 nm under an oblique illumination angle of 60^o with respect to the sample normal. The image exhibits a circular region, which is the relay-image of the BFP, and the superimposed reference wave which shows low frequency modulations due to the low-quality diffractive beamsplitter employed. A closer look additionally reveals high-frequency modulation which is a direct result of the phase gradient induced by the *off-axis* interference of the two terms[121,122,169].

Processing said hologram yields the real-space image shown in Figure 4.6 right, where we see many 20 nm GNPs over a field-of-view of approximately 200x200 µm. Analysing the particles' signal indicates high signal-to-noise and signal-to-background ratios. Paragraphs below explain how we process the *k*-scope's holograms and retrieve such real-space images.

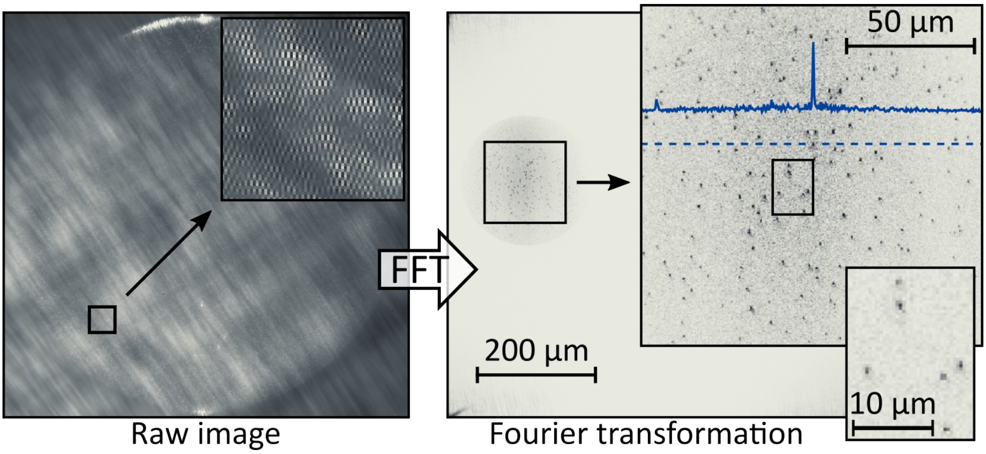

Figure 4.6, Data processing. Left: A typical back-focal-plane interferogram as recorded on the camera, for 20 nm diameter GNPs using an NA=0.7 air-objective. Magnified area shows the interferometric modulation. Right: The respective Fourier transformation reveals the image of interest over a large field-of-view; the amplitude range of the images with 200 µm and 50 µm scalebars has been restricted to approximately 20% of the maximum to visualise the particles. The solid blue line shows an image cross-section, comprising a 20 nm GNP, at the indicated position (dashed line).

First, we aim at isolating the interferometric components and transforming them into the real-space wavefronts; workflow illustrated in Figure 4.7. We begin by subtracting the camera dark-offset from all interferograms. We then separately acquire an image of the reference wave by blocking the sample-illumination and subtract the it from all acquired holograms. Additionally, we divide the resulting image by the square-root of the reference to correct potential amplitude inhomogeneities.

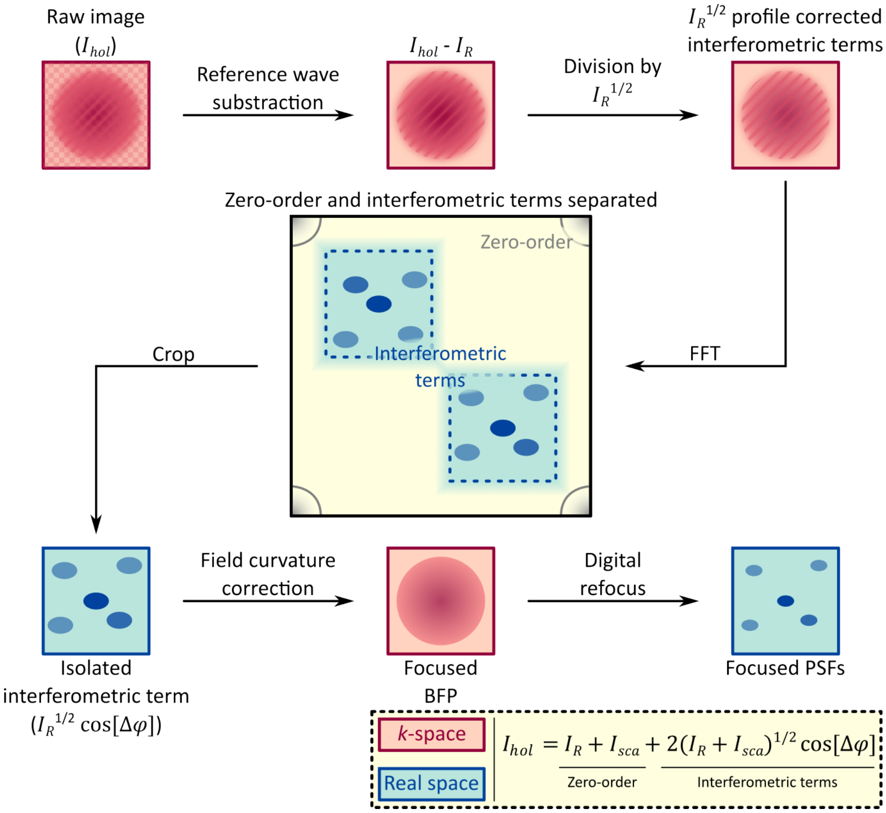

Figure 4.7, Real-space image retrieval. I_R contribution is subtracted from the raw data. Resulting image is divided by $\sqrt{I_R}$. An FFT is applied, resulting in real-space representations of the interferometric terms separated from the zero-order components. One of the former representations is isolated by cropping the image. The field curvature is corrected and the particles' PSF refocused. Salmon colour refers to *k*-space while turquoise indicates real space.

Afterwards, we isolate the interferometric terms by applying a fast Fourier transform (FFT) and cropping the signal of interest[121,170,171], as indicated in Figure 4.7. The resulting image is a real-space representation that shows the 20 nm GNPs (Figure 4.6).

However, the previous processing steps do not correct the potential defocus of the reconstructed wavefront. We correct the field curvature by multiplying each image with a spherical lens function. We then apply an inverse FFT (iFFT) that results in a focused BFP[17,133]. Finally, we correct the real-space image defocus.

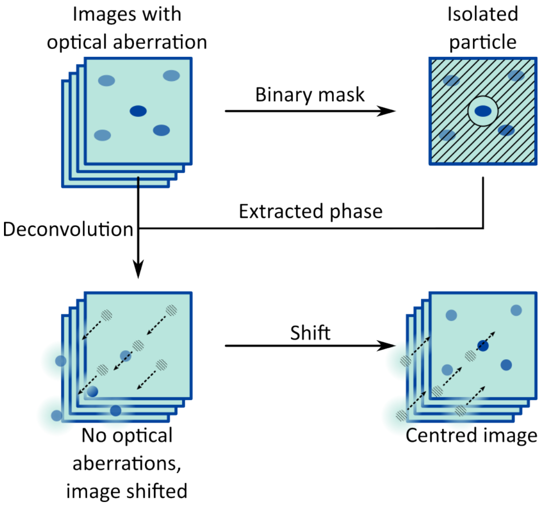

Figure 4.8, Optical aberration correction. A particle is isolated in an image by using a binary mask; its phase is extracted. All the images are deconvoluted with said phase, resulting in displaced optical aberration-free particles. The particles are the shifted to the original position.

We can further process the reconstructed image for correcting the potential optical aberrations, which can be quite severe when transmitting a wavefront through the freestanding, and often irregular, mica sheets. We start by characterizing the optical aberrations. We select a representative particle within one of the images and then isolate it by multiplying the image with a binary disk that eliminates all other image information (Figure 4.8). The typical circle size is approximately 10 times Nyquist. Afterwards, we iFFT the image and remove linear phase ramps, thus moving the particle to zero-order[132,138]. We then extract the residual phase information from the complex BFP image and divide the FFT of all individual images by said phase term. Finally, an iFFT of the phase-corrected complex BFP directly yields in-focus, aberration corrected, particle images[132,133].

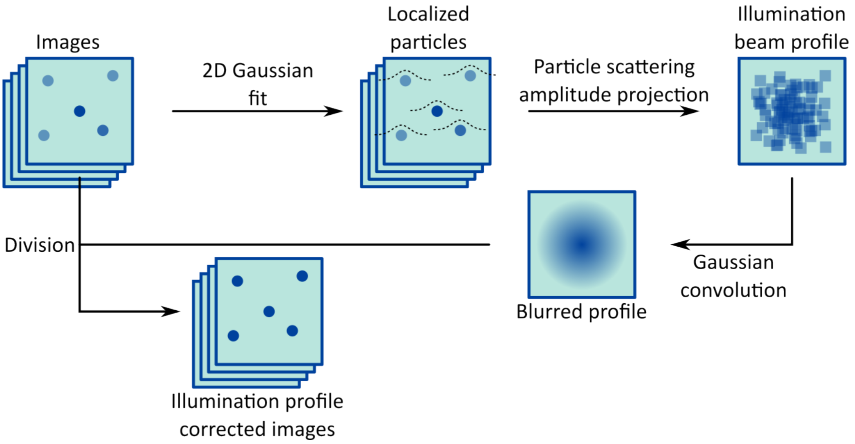

Figure 4.9, Illumination profile correction. Particles' location and scattering amplitude is extracted by performing 2D Gaussian fits. The illumination beam is reconstructed by projecting said values into a new image and convoluting it with a Gaussian function. All the images are divided by the reconstructed beam.

In a final step, we need to correct for the spatially non-uniform illumination profile which directly impacts the scattering amplitude. The process is shown in Figure 4.9. We identify all particles in all images and fit them using 2D Gaussian functions which yield scattering amplitudes alongside the x/y nanoparticle positions. Afterwards, we reconstruct the beam profile by relying on the amplitudes and positions of all particles. In brief, we generate an image containing all localised particles, normalised to the number of detection events per position and convolve the image with a wide Gaussian function. The area of the resulting beam-estimate is then normalised to unity and all particle-amplitudes are then divided by the beam's amplitude at their respective x/y-position. Particles in the low-amplitude regions of the illumination profile, <10% of the maximum amplitude, are excluded from the analysis as we noted considerable histogram broadening when including said fraction.

4.5 Experimental results

We ensure the linear dependence of the interferometric signal on both the illumination and reference wave amplitude by systematically measuring the power-dependence of each of them. The signal scaling (Figure 4.10a) confirms our expectations from equation (4.2). Apart from verifying that the obtained real-space image (Figure 4.6) is purely composed of interferometric contributions, the scaling has important implications for selecting ideal illumination/reference powers. Both the signal, as well as shot noise, scale linearly with the reference-amplitude and the signal-to-noise-ratio should thus be independent on it. Even though, sample-dependent factors might slightly impact this notion[172], it is necessary to operate above the dark-noise of the camera, which dictates the minimum amplitude of the reference wave. This minimum-reference approach conveniently reserves the highest possible camera range for detecting photons originating from the sample. The illumination power is then simply adjusted to ensure a sufficiently high signal-to-noise-ratio, without saturating the camera or destroying the sample.

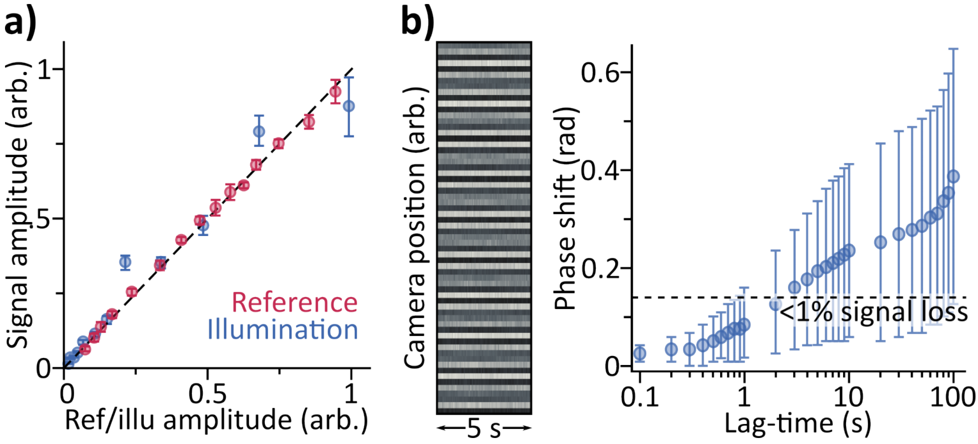

Figure 4.10, Signal dependence and stability. a) Signal amplitude dependence on the illumination (maroon) and reference (blue) field-amplitudes. b) Interference fringe stability over 5 s (left) and mean phase-shift for different lag-times between frames computed based on a 30 min experiment performed at 10 frames-per-second at 15 ms integration time (right). All error bars correspond to one standard deviation.

One additional consideration is the interferometric stability where *in-line* holography is often championed as being “more-stable” as the reference and scattering fields are intrinsically phase-locked. Based on our experience, however, *off-axis* holography only shows minor phase instabilities, that do not impact the signal quality, as long as sensible noise-reduction measures, such as floating the optical table, employing low beam heights and protecting the beam-path from air currents, are taken.

To quantify phase instabilities under extreme conditions, we separate the reference and illumination fields and dramatically increase the path of independent propagation to 3 m, before recombining them in the typical *off-axis* configuration. Figure 4.10b shows a phase-drift measurement with no statistically significant deviations from zero phase-shift for lag-times of <400 ms. We observe roughly 0.1 rad of drift, being equivalent to 8 nm, within one second. Such a phase drift manifests itself in a minor noise contribution on the order of 1% or, in other words, it is necessary to achieve unlikely single-particle signal-to-noise ratios exceeding 100 before the 0.1 rad phase-drift starts impacting the signal. More importantly, *off-axis* holography measures the signals' phase and computational phase-correction, prior to image averaging, is easily possible and eliminates the problem completely, as verified by performing signal-averaging experiments over observation times exceeding several tens of minutes.

Following this thorough technical characterisation of the sensing platform, we now turn our attention to quantitative particle size-measurements. As an initial test system, we employ GNPs of different nominal diameters ranging from 20 nm to 250 nm that are immobilized on mica. The samples are prepared by adding a 5 µL drop of a 0.1 g/ml solution of PLL-g-PEG (*SuSoS AG*) in PBS to freshly cleaved mica and then removing it immediately with a pipette. Following functionalisation, we incubate the sample with 2 µL of a suspension containing citrate-capped GNPs (*BBI Solutions*) and remove it after a few to tens of seconds, depending on the nominal size of the GNPs (40-250 nm). The 20 nm GNP stock-suspension was diluted five-fold prior to incubation.

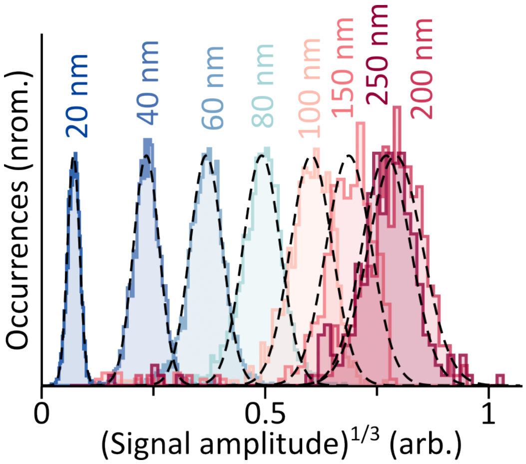

Figure 4.11, Quantitative sizing of GNPs. a) Signal distribution histograms measured for GNPs of different sizes, 20-250 nm (coloured) alongside Gaussian fits (dashed). The histograms contain: N_{20nm}=2563, N_{40nm}=3709, N_{60nm}=3354, N_{80nm}=1758, N_{100nm}=676, N_{150nm}=329, N_{200nm}=288, N_{250nm}=243.

Importantly, we perform all measurements under identical experimental conditions with the same illumination/reference intensities and camera-integration times, to demonstrate the extreme dynamic range of the *k*-scope. Figure 4.11 summarises the results obtained with particle-signal histograms, reminiscent of normal distribution functions. Figure 4.12a shows the relation in between the obtained signal and the particles' size. We opt for a cube-root plot of the measured signal amplitude for a clear representation of the different signals. The camera, in contrast, necessarily measures the scattering intensity which varies by more than five orders of magnitude for the different particles (Figure 4.12a, inset).

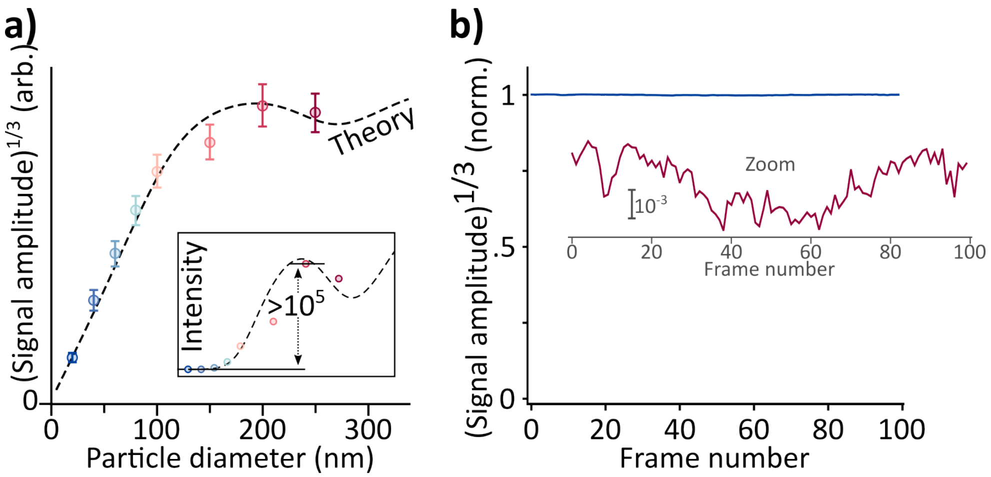

Figure 4.12, Quantitative sizing of GNPs. a) Comparison of the experimentally obtained particle size dependent (signal amplitudes)$^{1/3}$ with the theoretically expected values assuming scattering collection angles of 75-165°, 520 nm illumination and gold particles surrounded by air with a constant refractive index of n=1. The error bars correspond to one standard deviation. Inset: Same data and simulation but using an intensity scale corresponding to the signal-levels detected on the camera. b) Signal fluctuations of a single nanoparticle recorded over 100 frames. The zoom shows the signal in a different scale to highlight said variations.

As the particle diameter increases we observe a considerable deviation from the Rayleigh scattering approximation, with 250 nm GNPs exhibiting less scattering signal than 200 nm GNPs. A simple Mie-theory[102] based signal-estimate, which accounts for the 60°-illumination, nicely reproduces our experimentally observed trend (Figure 4.12a). In other words, the solid collection angle must be accounted for when theoretically describing the signal for particles being larger than 100 nm. Characterizing the calibration function is crucial for delimitating the signal amplitude range and avoiding sizing ambiguities.

Table 4.1 suggests that the origin of the histogram spread shown in Figure 4.11 for GNPs >40 nm is, predominantly, due to sample-intrinsic nanoparticle size variations and not due to measurement noise. To test this hypothesis, we record the signal of an ~100 nm particle over a total of 100 images. Figure 4.12b shows the diameter-signal, e.g. the cube-root amplitude, over the recorded frames. The signal fluctuates slightly around its normalised mean, with $1 \pm 8.6\times10^{-4}$ (one standard deviation), thus suggesting that the histogram spreads for the GNPs are due to the mentioned particle inhomogeneity and that the broadening due to noise is minimal.

GNP diameter (nm)	**Manufacturer**			**k-scope**
	Batch	*Mean diameter (nm)*	*Coefficient of variation (%)*	*Size error (%)*
250	25081	250.9	≤8	6.64
200	23710	202.9	≤8	7.20
150	24149	146.5	≤8	6.86
100	24071	102.2	≤8	7.17
80	22033	77.5	≤8	7.70
60	20633	60.0	≤8	8.69
40	21352	40.7	≤8	10.19
20	21799	19.6	≤8	11.15

Table 4.1, GNP size estimations. GNP specifications provided by the manufacturer and size errors from *k*-scope characterization.

To illustrate the achievable dynamic range we, simultaneously, immobilise the GNP exhibiting the lowest, 20 nm, and highest, 200 nm, scattering amplitudes on the same sample and record *k*-scope images as outlined above. Figure 4.13 shows representative scattering amplitude images that verify that simultaneous detection is indeed possible, albeit a nominal signal difference, as detected by the camera, by approximately 10^6.

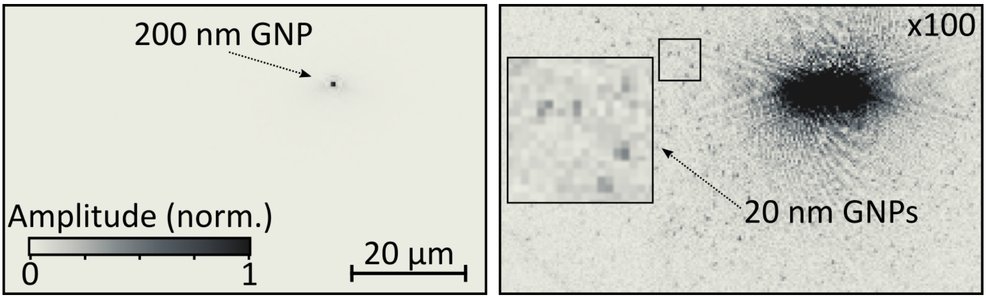

Figure 4.13, Image of a heterodisperse GNP sample. Amplitude image recorded for a sample containing 200 nm and 20 nm GNPs normalised to the maximum (left) and to 1/100 of it (right). The faint line in the bottom left corner is due to steps in the mica surface.

As a result of *k*-scope's extreme dynamic range, shot-noise might render it difficult to identify small particles that are spatially very close to a strongly scattering particles. An experimentally easy-to-implement mitigation is to use slightly diluted samples, thus increasing the inter-particle spacing.

Thus far, we concentrated on measuring GNPs as their widespread use allows facile cross-platform comparison. The results presented in Figure 4.12a suggest that quantitative sizing of arbitrary particles should be possible but the challenge is to provide a suitable calibration that allows relating the observed signals to the correct particle diameter. As biological particles are dielectric, we perform calibration experiments using SiO_2 particles whose refractive index of $n_{520nm}=1.461$ is somewhere between the extremes of EVs[173] and proteins[174]. This similarity ensures that only minor scaling is necessary to adopt the measured calibration to a biologically relevant material, thus reducing potential errors associated with dramatically scaling, as would be the case for a GNP-based calibration.

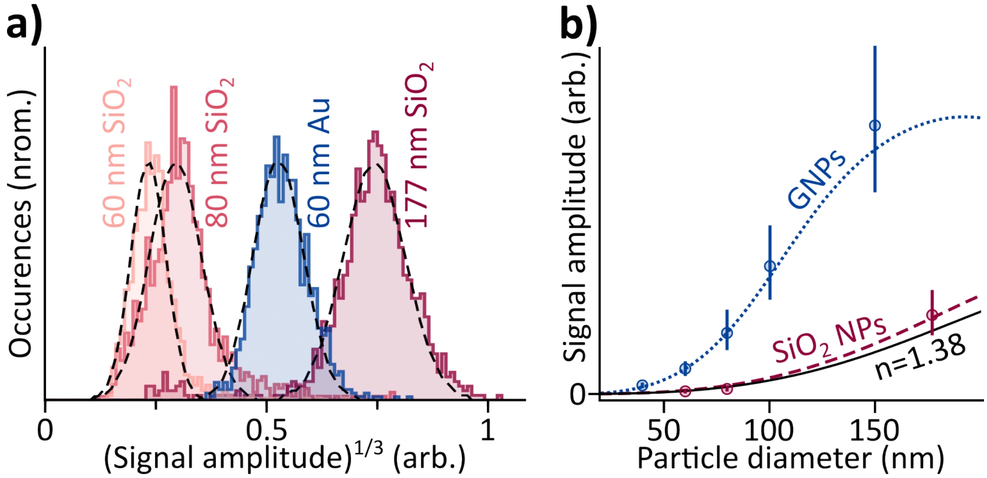

Figure 4.14, Absolute size calibration. a) SiO_2 nanoparticle-histograms for three different particle sizes alongside 60 nm GNPs. b) Theoretical signal dependences based on the SiO_2 data (maroon) describes the GNP amplitudes (blue) well. The black line shows the expected signal-scaling for EVs, assuming a refractive index of n=1.38. The error bars correspond to one standard deviation.

For these measurements, we immobilize SiO_2 (Table 4.2) particles by drying 5 µL of a diluted particle stock suspension on freshly cleaved mica. Figure 4.14a shows the histograms obtained for SiO_2 particles with diameters of 60, 80 and 177 nm in comparison to a measurement of 60 nm GNPs. The combination of the SiO_2 and the Au measurements allows estimating how well the particle size of one species can be determined by using a calibration obtained with a different material. As previously, we use a Mie theory-based simulation to describe the SiO_2 signal-dependence (Figure 4.14b). Simultaneously, we compute the expected signal-curve for GNPs and scale it by relying on the SiO_2 calibration. Figure 4.14b shows a near-perfect match between the SiO_2 and the Au measurements, even though the scaling of the theoretical curves purely relies on the SiO_2 data. Given the quality of agreement, albeit the dramatic difference in absolute scattering cross-sections, we suggest that a SiO_2 calibration should be well suited for sizing EVs, which exhibit similar cross-sections, with an approximate refractive index of n=1.38[173].

SiO_2 particle diameter (nm)	Manufacturer	Batch	Mean diameter (nm)	Coefficient of variation (%)
177	nanoComposix	sio2-R-L2017	177	9
80	nanoComposix	SCM0035	81	6
60	microParticles GmBH	JEA0144	60.3	2.9

Table 2, SiO_2 nanoparticle size estimations. Silica particle specifications provided by the manufacturer.

To conclude we perform sizing experiments of ovarian cancer (OVCA) cell-derived EVs. For these initial proof-of-concept demonstrations, we incubate freshly cleaved mica substrates with an aqueous EV suspension for approximately 5 mins and then carefully remove residual water from the surface. As we purely rely on nonspecific binding of the EVs, we suspect that we might be selectively detaching some of the larger EVs during the removal process. Despite this non-ideal approach, we clearly observe widely varying signal levels (Figure 4.15a). The image highlights the extremely heterogeneous nature of EV-samples, with relative scattering amplitudes varying by more than 100-fold, which is equivalent to $>10^4$ in measured signal-intensity. By acquiring multiple images, we obtain EV size-distribution histograms (Figure 4.15b). Reassuringly, separately prepared samples yield qualitatively similar histograms with some deviations in the larger diameter range as expected based on the considerations given above.

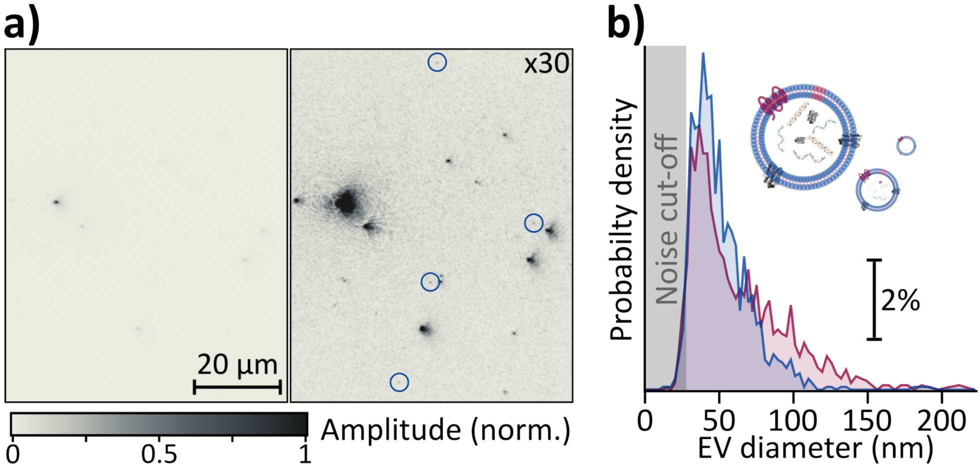

Figure 4.15, Extracellular vesicle characterization. a) Representative amplitude images of EVs immobilised on mica normalised to the maximum (left) and to 1/30 of it (right). b) EV size-distribution histograms for two independent measurements. The steep cut-off towards lower diameters, around 25 nm, is due to signal-to-noise limitations, when only one camera frame is acquired, and not representative of the real particle distribution.

Even though we observe some discrepancy between the measurements presented here and the independently performed size-quantification via NTA (Figure 4.16) we attribute this difference to the general limitation of NTA for quantifying small EVs, as recently highlighted in a comparative study by *Bachurski et al.*[175]. Irrespective, our current *k*-scope is able to detect single EVs with diameters as small as 25 nm, assuming a refractive index of n=1.38 which is on the lower end of the reported values[173,176,177]. Importantly, the experimentally limiting factor is merely the integration time chosen, which was set to 5 ms in the current experiment, as the mica surface is virtually background-free. Even though we could easily acquire more sensitive data, by averaging multiple images, we opted for the cut-off presented here as we believe that the main limitation in the small size-range is the difficulty to distinguish EVs from other microvesicles and potential contaminations such as protein aggregates or lipoproteins and not the mere detection of scattering particles.

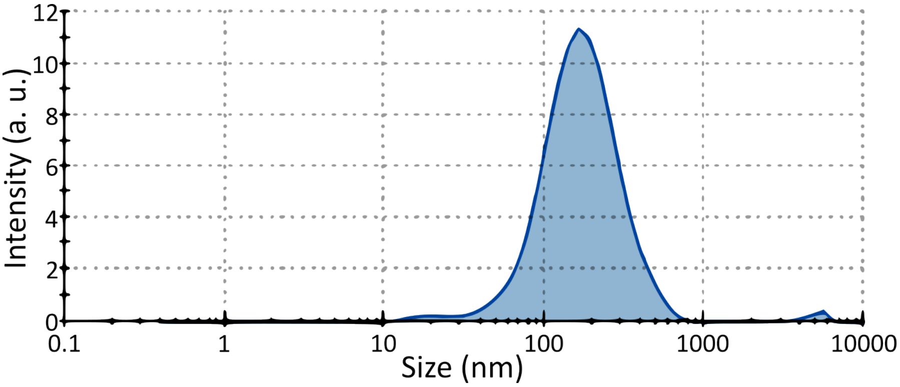

Figure 4.16, EV size distribution via NTA. Average EV diameter of 140.9 nm. The size distribution shows three peaks located at 189.8 nm, 20.17 nm and 4971 nm, with relative intensities of 0.98, 0.012 and 0.009, and widths of 102.0 nm, 4.884 nm and 625.2 nm respectively.

In order to perform these initial proof-of-concept experiments, Ala Jo and Hakho Lee obtained the EVs from cell cultures and performed the NTA measurements shown in Figure 4.16. For extracting the EVs, OVCA cells (SkOV3) are cultured in RPMI-1640 medium (*Cellgro*) with 10% fetal bovine serum (FBS) at 37°C in a humidified atmosphere with 5% CO_2. Afterwards, before EV collection, cells are grown in RPMI with 5% exosome-depleted FBS (*Thermo Fisher Scientific*) for 48 hours. Then the cell debris is removed by centrifuging the supernatants from the cell culture media at 300 g for 5 min. Next, the supernatant is filtered through a 0.2 µm membrane filter (*Millipore*) and, subsequently, concentrated at 10^5 g for 70 min. After the supernatant had been removed, the EV pellet is washed in PBS and then centrifuged at 10^5 g for 70 min. Finally, the EV pellet was resuspended in PBS and stored at -80°C. The EV concentration was determined by NTA (*NanoSight, Malvern*) and additional size-quantification was performed using a *Zetasizer Nano ZS* (*Malvern,* Figure 4.16).

4.6 Conclusion and outlook

To summarise, we implemented a *k*-space holographic microscope (*k*-scope) that images a sample of interest by interfering a conjugate plane of the microscope's BFP in an *off-axis* holographic configuration. This Fourier imaging approach dramatically boosts the achievable dynamic range of widefield nanoparticle-sensing platforms as the information of all individual particles is projected onto all camera pixels, rather than being localised at a well-defined pixel location. We demonstrated the feasibility and sensitivity of this approach by quantitatively sizing GNPs with diameters ranging from 20-250 nm. Furthermore, we proved that the *k*-scope is capable of determining the size of an unknown particle-distribution by relying on different material particle calibrations. Ultimately, we presented initial proof-of-concept work that shows that the *k*-scope is a promising candidate for a rapid EV size-quantification platform, capable of simultaneously sizing entire EV-populations due to the dramatically improved dynamic range. We believe that the *k*-scope can led for a clinically viable sizing-platform as our technology can be coupled with specifically modified sample-substrates[178,179]. In addition, the enormous miniaturisation-potential of devices based on digital holography would help making said device cost-competitive.

Chapter 5:

Simultaneous sizing and refractive index analysis of heterogeneous nanoparticle suspensions

Effective nanoparticle characterization is of key importance for a wide range of nano- and life-sciences. There are several techniques for analysing homogeneous particle populations exist, although they often fail to characterize heterogenous samples, as particles of different sizes and compositions can lead to undesignable signals. Here, we present the holographic Nanoparticle Tracking Analysis (NTA), which decouples the size and refractive index contributions while simultaneously capturing both properties. Conceptually, we combined high dynamic range k-space imaging with 3D particle tracking, which is supported by the digital propagation of the recorded wavefront. Our platform enables the long-term particle tracking by extending the volume-of-view and, in consequence, increases the sizing precision compared to typical NTA. As validation, we measured metallic and dielectric nanoparticles and monitored the protein-corona formation for three different proteins.

Parts of this chapter have been adapted from the following publication: Ortiz-Orruño, U., Quidant, R., van Hulst, N. F., Liebel, M., and Ortega Arroyo, J., *ACS Nano* **2023**, 17, 1, 221–229 and are copyright (2022) by American Chemistry Society. I built the setup and recorded the experimental data. Jaime Ortega-Arroyo performed the data analysis.

5.1 Introduction

Precise nano- and bio-particle characterization is of key-importance in the nano- and life-sciences[12,155,178–183]. These methods are key-enablers for both fundamental research as well as day-to-day screening and quality-control applications. Chapter 4 introduces a promising label-free microscope for particle sizing, the *k*-scope. We demonstrate that said platform is able to successfully size metallic and dielectric nanoparticles as well as bioparticles, which were measured in the form of extracellular vesicles (EV)[22–24]. However, all the characterized samples consist on particles bound to a surface, which is not ideal. For example, fixing the EVs to a surface can modify their shape[184]. Additionally, measurements that depend on non-specific surface-binding of the analyte can be strongly biased as only a fraction of the potentially randomly charged sample is captured[185]. Besides, particle-dependent buoyant densities and size-dependent Brownian motion might further distort the surface-based particle capture, thus rendering quantitative concentration-measurements difficult to impossible. Lastly, directly measuring particle suspensions provides particle information on media, which is especially relevant for biological applications[186–189].

Among the many available techniques able to characterize particles in suspension in a label-free manner, dynamic light scattering (DLS)[64,65] and nanoparticle tracking analysis (NTA)[18,19] are especially promising due to their non-invasive nature and their often straight-forward and inexpensive experimental implementation. Said methods indirectly infer the size of the particles by analysing their diffusion. DLS considers the whole nanoparticle population as a single entity, which induces a bias when polydisperse samples are studied[72]. NTA, in contrast, infers the hydrodynamic diameter (d) of many individual micro- or nanoparticles by following their Brownian motion over extended observation times. Albeit being incredibly powerful for larger nanoparticles, with diameters >100 nm, NTA struggles with smaller ones[162,190] which exhibit very large diffusion coefficients. These particles rapidly traverse the quasi two-dimensional observation plane of a conventional microscope within a few camera frames, which dramatically degrades the sizing precision[20,21].

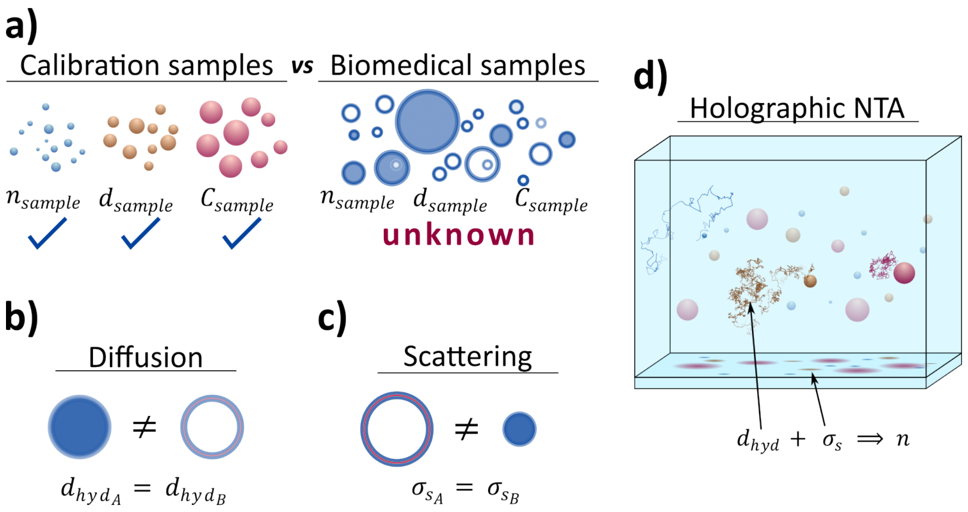

Figure 5.1, Challenges in nanoparticle sample characterisation. a) Typical calibration samples often don't reflect biomedical reality; the former exhibit well-defined dielectric constants, narrow size-ranges and known surface charges, the latter are heterogeneous and composed of different biological building-blocks. b) Diffusion-based NTA measures particle hydrodynamic radius but omits material composition. c) Particle scattering efficiency is related to both size and composition. If the composition is unknown, particle size cannot be determined from it. d) Holographic NTA simultaneously measures a particle's hydrodynamic radius and scattering amplitude and furthermore eliminates the need for potentially biased surface-binding. Combined, these quantities allow inferring the dielectric constant of the particle and hence its biological composition.

Beyond the sensitivity aspects, accurately characterizing unknown particle populations is complicated for both NTA and DLS as well as for systems that rely in quantifying the scattering cross-sections (σ_s), such as the k-scope. The label-free nature of said methods makes them depend on signal calibrations for estimating the particles' size from the recorded data. Typical calibration-samples exhibit known refractive indexes (n_{sample}), narrow size distributions (d_{sample}) and homogeneous surface charges (C_{sample}). However, contrary to calibration samples, typical biomedical samples such as, for example, EVs not only are very heterogeneous in size[157,158], but exhibit widely varying compositions and hence particle-dependent refractive indexes[191] and surface charges[192] (Figure 5.1a). Similar particle populations are also ubiquitous in the field of nanomedicine with the synthesis and development of targeted drug delivery systems, and colloidal chemistry, where different nanoparticle populations are synthesised and their interaction with other reagents is tested, e.g. protein corona formation[193]. Estimating the d by analysing the diffusion omits key information as, for instance, the cargo of mentioned vesicles (Figure 5.1b) or the presence of protein coronas. Methods based on scattering cross section quantification are even more limited as their size estimations are based on a parameter that highly depends on particle composition, decreasing sizing precision with composition heterogeneity (Figure 5.1c).

In this chapter, we address the aforementioned challenges by implementing a holographic NTA (holoNTA) platform, for the precise and accurate characterisation of nanometric sample suspensions. We holographically reconstruct the 3D trajectories of free-floating particles estimating their size from their diffusion while, at the same time, we record their scattering amplitudes. The approach, illustrated in Figure 5.1d, yields particles' d and refractive indexes at a single particle resolution, yielding important information about particle composition in a non-invasive form. The use of digital refocusing dramatically increases the volume-of-observation, compared to the quasi 2D observation-plane of conventional NTA. The approximate 40-fold increase in observed z-range allows recording long particle-trajectories and confidently characterising the diffusion coefficients of tiny NPs. Ultimately, the k-space imaging enables simultaneous detection of particles with vastly different sizes.

5.2 Theoretical considerations

Under Brownian motion, the relation between the time it takes for a particle to travel a certain distance, x_b, e.g. the boundaries of the imaged volume, can be derived from the typical first passage time, t_p, as $t_p = x_b^2/(2D)$, where D is the diffusion coefficient of the particle[194]. According to the Stokes-Einstein equation[108], D and d are related and, thus, we can estimate d from a particle motion.

NTA records videos of free-floating particles for calculating their D by analysing the particles' motion. According to NTA, we first locate the particles along the frames. Then, we retrieve x_b and t_p for different time intervals. Finally, we calculate the individually mean-square-displacement (MSD)[20] for each particle.

The uncertainty, σ_D/D, in determining the diffusion coefficient via MSD and thereby in sizing the nanoparticles, relies on several factors. Specifically, the overall trajectory length, N; the number of points used to fit MSD curve; and, the reduced localisation error[20,195]. The reduced localisation error, χ, is expressed as $\chi = \sigma^2/D\Delta t$, and can be understood as the ratio between the static localisation uncertainty and the displacement of the nanoparticle within consecutive frames. Specifically, σ and Δt, correspond to the localisation uncertainty and time between consecutive frames, respectively. For cases where $\chi \ll 1$ and recalling that $\sigma_D/D{\sim}\sigma_d/d$ by error propagation, the relation between the sizing uncertainty and the track length is given as $\sigma_d/d{\sim}\sqrt{3/(N-2)}$[20]. The above condition, $\chi \ll 1$, is satisfied for measurements with low localisation uncertainty of particles with large diffusion coefficients, i.e. nanoparticles. It is important to note that this relation applies to the relative size uncertainty and not the absolute one; therefore, larger particles exhibit higher absolute dispersion values compared to smaller ones.

Combining the expressions of first passage time together with the relative size uncertainty as a function of track length one can intuitively note that increasing the depth of focus by a factor, m, results in longer tracks by a factor of m^2. This in turn reduces the relative size uncertainty by approximately this same factor, m, hence dramatically improving the accuracy and precision.

Holographic detection can routinely extend the depth of focus by at least an order of magnitude. Thereby, when the depth of focus is the limiting dimension in the imaged volume, holography increases the total observation time of particles by at least two orders of magnitude. In consequence, holoNTA implementations drastically reduce the sizing uncertainties compared to traditional NTA platforms.

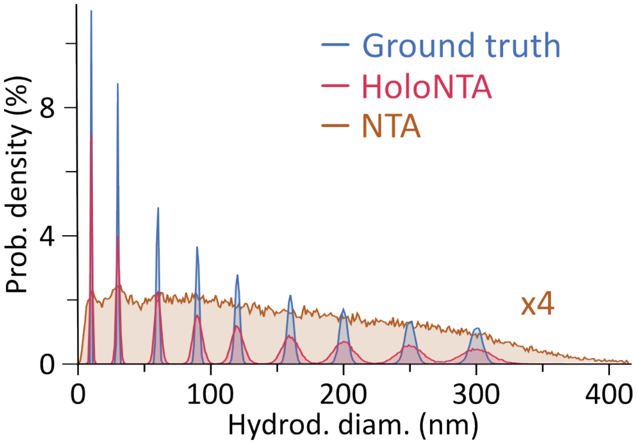

Figure 5.2, The advantage of holoNTA. Simulation comparing ground-truth and NTA- or holoNTA-recovered size-distributions.

To put these abstract numbers into a more accessible form, we simulate NTA and holoNTA experiments for freely diffusing particles, assuming a heterogeneous sample. We consider Brownian motion in water and 10000 particles, each with diameters of 10, 30, 60, 90, 120, 160, 200, 250 and 300 nm. To approximate a realistic experimental scenario, we assume 20 s image acquisition at 100 frames-per-second, a localization error of 10 nm in each dimension and a volume of observation of 80x80x4 μm^3 (NTA) and 80x80x80 μm^3 (holoNTA), respectively. Each nanoparticle diffuses from the centre of this volume either until it leaves the observation volume or until 2000 frames have been recorded. Figure 5.2 compares the size-accuracy of the two methodologies with the size-estimate that would have been obtained if each NP would have been observed for 2000 frames. While holoNTA only suffers a minor reduction in sizing-accuracy, NTA completely fails to recover the particle-distribution of this heterogeneous sample.

In addition, the longer particle observation times of holoNTA effectively resolve trajectories that NTA would fractionalize. In consequence, holoNTA reduces the number of double-detected particles, a common problem in NTA, where particles leave and then return to the small volume-of-observation, which has been associated to issues in repeatability amongst different commercial implementations[162].

5.3 Setup

Figure 5.3 schematically depicts our holoNTA platform, which consist of a simplified design of the *k*-scope introduced in Chapter 4. Both illumination and reference waves are obtained from a 532 nm DPSS laser (*CW532-100*, *Roithner Lasertechnik*) coupled into a 99:1 fibre-beamsplitter (*TN532R1A1*, *Thorlabs*). The former (99% fraction) is focussed onto the sample, mounted on top of an inverted microscope, in a transmission configuration. The use of a long focal-length lens ensures near-plane wave-illumination of the sample volume, which is positioned within the Rayleigh range of the focusing wave. The wave is collected by a water immersion objective (*UPLSAPO60XW/1.20*, *Olympus*) and the transmitted illumination light is selectively rejected via a beam-stop placed into the back-focal-plane of the objective that blocks the lower angles of the *k*-space[130]. The scattered light passes the beam-block towards higher angles and a 0.5x relay imaging system projects it forming an image of the objective's back-focal-plane on the camera (*a2A1920-160umBAS*, *Basler*), where it interferes with the collimated reference wave in an *off-axis* configuration. The coherence length of the laser we use ensures the inference of light scattered by particles over the whole volume-of-observation. The optical path lengths of both waves are coarsely matched, within a few centimetres, to ensure optimal interference contrast.

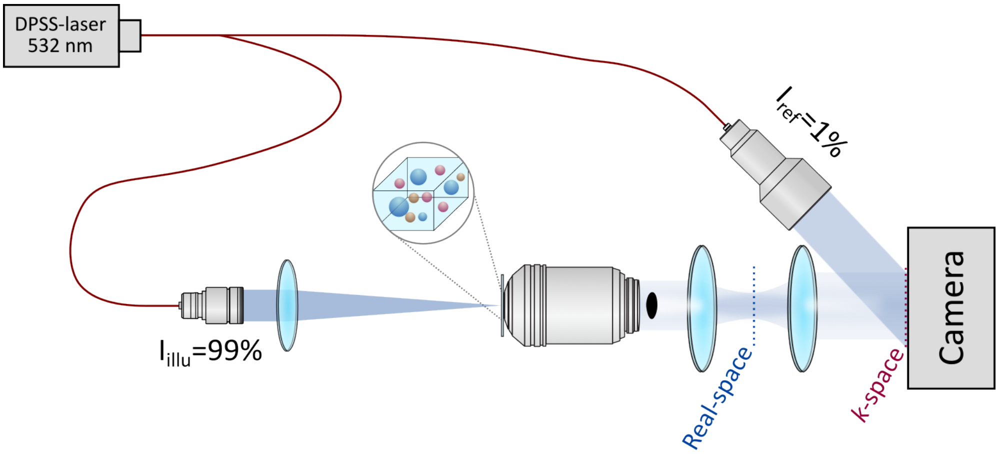

Figure 5.3, HoloNTA sensor. Schematic of the holoNTA implementation, based on a *k*-space holographic sensing platform. The waves propagate in the *off-axis* configuration.

The imaged *k*-space hologram corresponds to camera sensor area of 1200 pixels x 1200 pixels. We record videos composed by 2048 holograms. For all experiments, ten different measurements corresponding to different sample locations are taken at 20, 50 and 100 µs exposure times. Camera frame rate is set either to 78 Hz or 156 Hz, depending on the experiment, corresponding to a recording time of about 26 s and 13 s, respectively. The maximum frame rate of acquisition, 156 Hz, is limited by the minimum read-out time of the camera.

The sample is illuminated with 32 mW over an experimentally measured area of approximately 80 µm in diameter, encompassing >10% of the maximum amplitude. Reference beam, 18 µW, is set to overpass the dark-counts of the camera while maximizing the photon budged for the sample signal. Beam fluences are 6.8 µW/µm^2 and 4.2 pW/µm^2, respectively. Minor fluctuations between measurements are normalised by recording the power prior to each experiment.

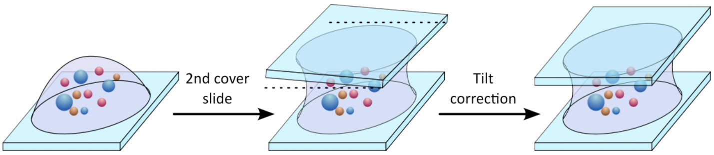

Figure 5.4, Aquarium. A drop of sample is placed onto a cover slide. A second slide is added forming a sandwich and its potential tilt is corrected.

To mount the sample on the microscope, we first place a cover slide and add a drop of the sample solution. A second cover slide, mounted above the former, is then lowered onto the sample solution until contact, forming a sandwich as indicated in Figure 5.4. If necessary, we tilt correct the orientation of the top cover slide to ensure that the back-reflections and the illumination wave are blocked by the beam-stop. Following the sample-mounting we wait a few minutes to ensure that disturbances, such as internal flows, do not distort the particles' free-diffusion.

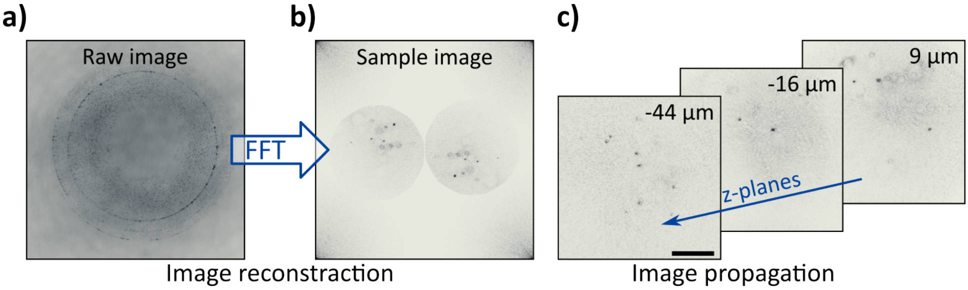

Figure 5.5, Data processing. a) Representative hologram alongside a Fourier-filter extracted sample image. b) Examples of multiple sample-planes obtained after computational image propagation. Scale bar: 25 µm.

5.4 Data analysis

Figure 5.5a shows an as-detected camera image. This section aims at explaining the data processing that enables extracting particles' σ_s and d from such holograms.

First, prior to performing any data processing, we subtract the camera's dark-offset from all recorded images. Additionally, for each experiment, we separately acquire an image of the reference wave, denoted here as reference, by blocking the sample illumination.

We then reconstruct the wavefront and correct the potential optical aberrations in a similar way to the data processing of Chapter 4. We start by subtracting the reference from all acquired holograms and then dividng the difference by the square root of the reference, thereby correcting for potential amplitude inhomogeneities, as described in Figure 5.6. Inverse Fourier transforming the processed *k*-space holograms then reveals three non-overlapping regions in image-space: the twin- and zero-order images, respectively (Figure 5.5b). We then isolate one twin-image, corresponding to one of the interference terms, by Fourier filtering, which involves hard-aperture selection followed by phase shifting. Finally, the as-processed twin-image is Fourier transformed to yield the wavefront in *k*-space which is subsequently used for further downstream processing.

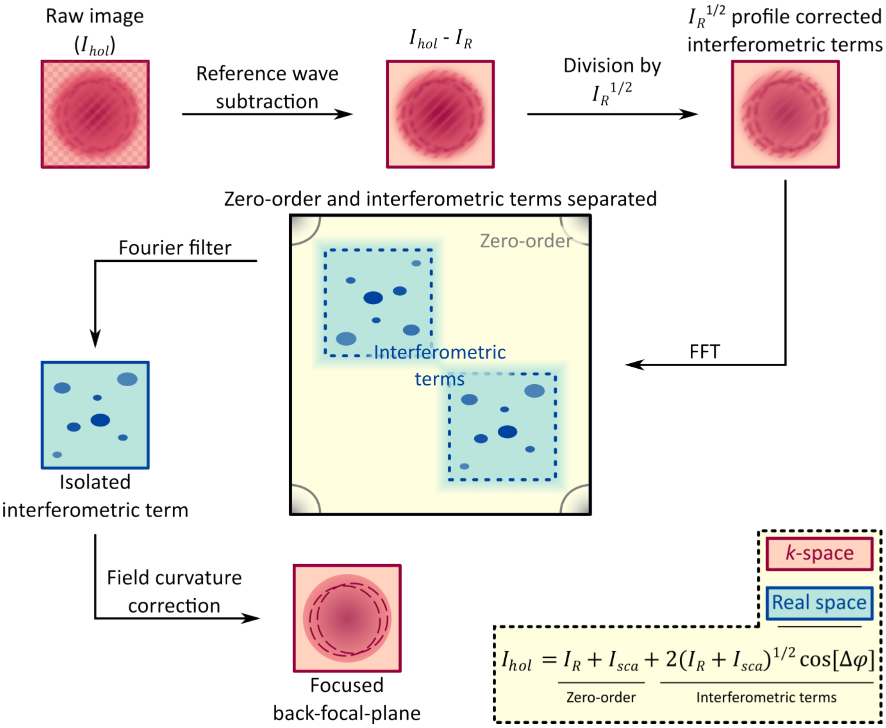

Figure 5.6, Hologram processing. The reference is subtracted from the raw data and the resulting image is further divided by the square-root of the reference. Next, the signal is Fourier transformed, resulting in real-space representations of the interferometric terms separated from the zero-order component. One of the former representations is then isolated by cropping the image and the field curvature is corrected. Salmon colour refers to *k*-space while turquoise indicates real space.

We continue by eliminating the contributions from static scattering signals, which are intrinsic to the sample and to imperfections in the optical system. First, we generate a *k*-space background based on the temporal median of the reconstructed wavefronts and we then subtract it from all *k*-space images (Figure 5.7a). We further account for the spatially nonuniform illumination profile, which affects the scattering signals by reconstructing the beam profile based on the amplitudes and positions of all localised particles in 3D[196], as described in Figure 5.7b. In short, we generate an image containing all localised particles, normalise it to the number of detection events per position and then lowpass filter this image. The resulting beam-area estimate is then normalized to unity and used to normalise all particle-amplitudes at their respective x/y-position. Particles in the low-amplitude regions of the illumination profile, <10% of the maximum amplitude, are excluded from the analysis. We continue by removing the potential optical aberrations (Figure 5.7c). We ensemble average the normalised point spread functions of all particles from a representative video and isolate them from the rest of the ensemble image using a binary mask with a width of ten times Nyquist. The resulting ensemble points spread function image in real-space is Fourier transformed, and the phase from the complex back-focal-plane image retrieved. Finally, we remove aberrations by deconvolving the real-space images.

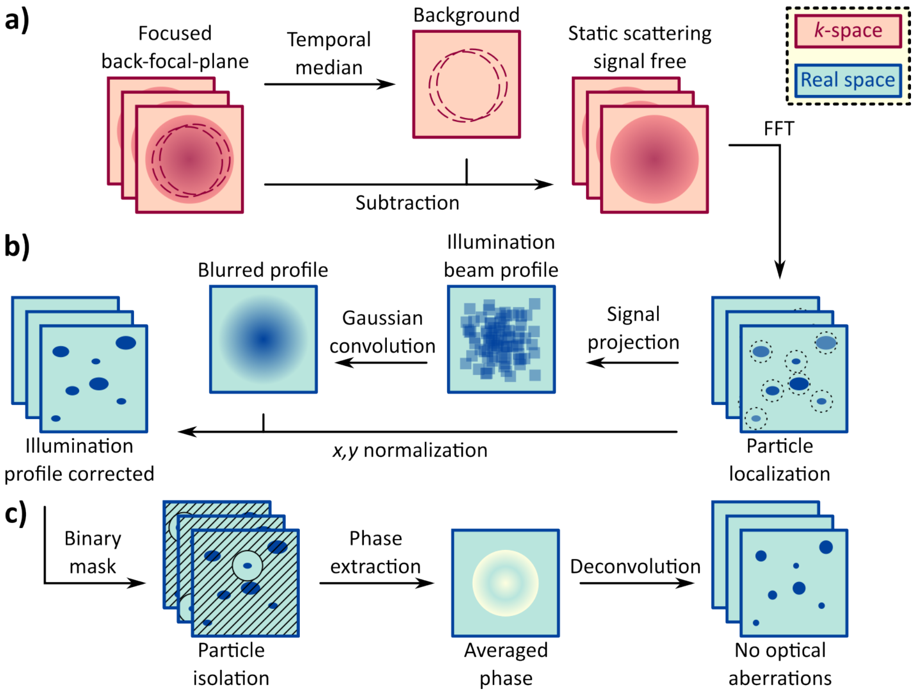

Figure 5.7, Background and aberration correction. A background of the static scattering signals is created by applying a temporal median to the previously processed images. The background is then subtracted from the images. Next, the images are Fourier transformed and all particles are localized. Afterwards, the illumination beam's profile is reconstructed by projecting the particles' signal into a new image and convoluting it with a Gaussian function. The images are then divided by the resulting beam profile. Next, particles are isolated and their phase extracted. Finally, images are deconvoluted by the average of the extracted phases, yielding on optical aberration-free images. Salmon colour refers to *k*-space while turquoise indicates real space.

Afterwards, we reconstruct the volume-of-view by propagating the aberration corrected holograms along the optical axis, according to the angular spectrum method[137,138,141] (described in Chapter 3). Briefly, the processed $M \times M$ pixel^2 *k*-space holograms are multiplied by the propagation kernel $\boldsymbol{K}$ and subsequently inverse Fourier transformed. Specifically, the propagation kernel has the form:

$$\boldsymbol{K}(x,y,z) = \exp\left(-i\sqrt{k_m^2 - k_x^2 - k_y^2}\, z\right), \tag{5.1}$$

where $k_m = 2\pi n/\lambda$, with n being the refractive index of medium through which the light propagates, corresponding to water in this work. The discretised spatial frequencies are $\left(k_x, k_y\right) = 2\pi(x, y)/M\Delta x$ for $(-M/2 \leq x, y \leq M/2)$, with Δx representing the magnified pixel size of the imaging system. Representative planes obtained from the same hologram are shown in Figure 5.5c.

We then 3D locate each nanoparticle (Figure 5.8). Each hologram is first propagated from −40 µm up to +40 µm with a coarse spacing between different Z-planes (*Δz*) of 400 nm. Next, the resulting 3D intensity maps are segmented into regions of interests based on local maxima and the z-range is set to 50-80 µm depending on the experiment. To achieve sub-pixel localisation, the particle-containing segmented regions of interest are propagated with a finer Δz spacing of 100 nm over a total of +/-2 µm with respect to their local maxima. We then determine the particles' maxima within a 1 µm x 1 µm region around the centre-of-mass and subsequently fit a parabola using the two most adjacent z-pixel values along the maximum. For subpixel localisation along the *xy*-plane, particles that are in focus at the calculated z-plane are fitted using the radial centre symmetry algorithm[197]. The particles' amplitude is then extracted. Finally, we use the adaptive tracking algorithm of Jaqaman *et al.* to link all the 3D localisations and generate 3D tracks[198]. Only trajectories longer than 100 time points are used for further analysis.

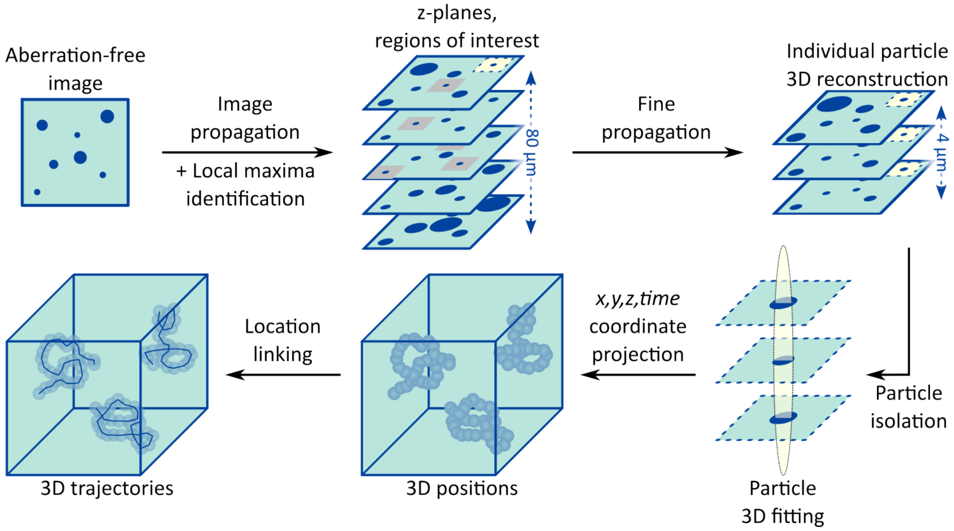

Figure 5.8, Hologram propagation and 3D single particle tracking. First, the previously reconstructed aberration-free images are propagated. Afterwards, the regions of interest are identified based on local maxima. A fine propagation is then done for each plane containing said regions. Next, particles are individually isolated and their 3D signal is fitted. The volume-of-view is then reconstructed by projecting particle spatial and temporal positions. Finally, 3D trajectories are extracted by linking particle localizations overtime.

Repeating the workflow outlined above, for videos composed of several hundreds to thousands of frames, yields the 3D trajectories of the particles. We then determine the size of each individually tracked particle from the 3D MSD curve. In brief, we extract the diffusion coefficient from the slope of a linear fit of the first three points ($t = m\Delta t$ for $m = 1,2,3$) of the MSD following the expression: $MSD(t) = x_0^2 + 6Dt$. We choose to only fit the first three points of the MSD curve as our experimental conditions closely satisfy the regime where $\chi \ll 1$, where $\chi = \sigma^2/D\Delta t$[20]. Namely, in our experiments the value for $\sqrt{D\Delta t}$, ranges from 100 to 270 nm, depending on the particle diameter (40-300 nm), whereas, our static localisation uncertainty, σ, is estimated to be on the order of 10 nm, making $\chi < 0.01$.

5.5 Experimental results

To experimentally validate our theoretical expectations, we perform holoNTA measurements on samples composed of freely diffusing gold nanoparticles (GNPs)

(*BBI solutions*) with nominal diameters of either 40 nm or 60 nm diluted in water ($2.5\text{x}10^8$ particle/mL). Figure 5.9 shows the experimentally obtained hydrodynamic diameter estimates, for 23 s videos, as a function of the available trajectory length used for extracting it. In terms of the relative uncertainty in hydrodynamic diameter as a function of track length, the measurements closely follow the expected $\sigma_d/d \sim \sqrt{1/N}$ scaling regardless of particle size, up until the results converge to the inherent dispersion of the nanoparticle population. Importantly, the widths of the size distributions obtained for >1000 frames reflect the intrinsic 8% size-heterogeneity of the, as purchased, GNP samples. In other words, holoNTA should be well-suited for accurately characterising both homogeneous and heterogeneous samples with realistic size-distribution ranges.

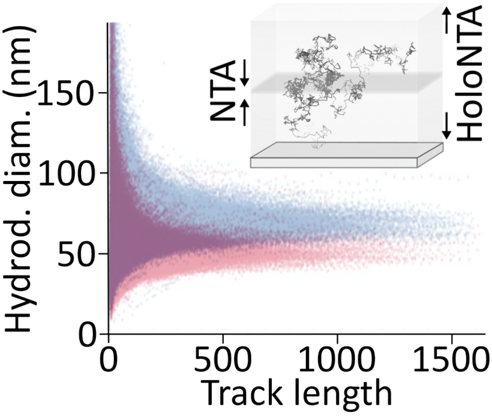

Figure 5.9, Track length effect on sizing precision. Experimentally obtained track length-dependent hydrodynamic diameters of samples containing either 40 nm or 60 nm GNPs suspended in water. Camera frame rate = 156 Hz, t_{exp} = 100 µs.

Following the discussion of our holoNTA platform and its advantages over traditional NTA, we now move towards thoroughly characterising its performance. To this end, we measure several monodisperse nanoparticle samples, e.g. particles with a well-defined mean diameter and composition that exhibit synthesis-dependent sample heterogeneity around their mean. Figure 5.10a shows the results obtained for both spherical Au (40, 60 and 80 nm) as well as SiO_2 (143 and 254 nm, *microParticles GmBH*) nanoparticles diluted in water ($2.5\text{x}10^8$ particle/mL). We obtain near-normal distributed diameter and scattering amplitude estimates for all five particles that are well-separated in the holoNTA-enabled 2D representation (Figure 5.10a). This simultaneous two-parameter estimate furthermore allows inferring the particles' refractive index. A comparison between our measurements and Mie theory-based diameter-amplitude curves for the two materials shows remarkably good agreement (Figure 5.10a, dashed lines).

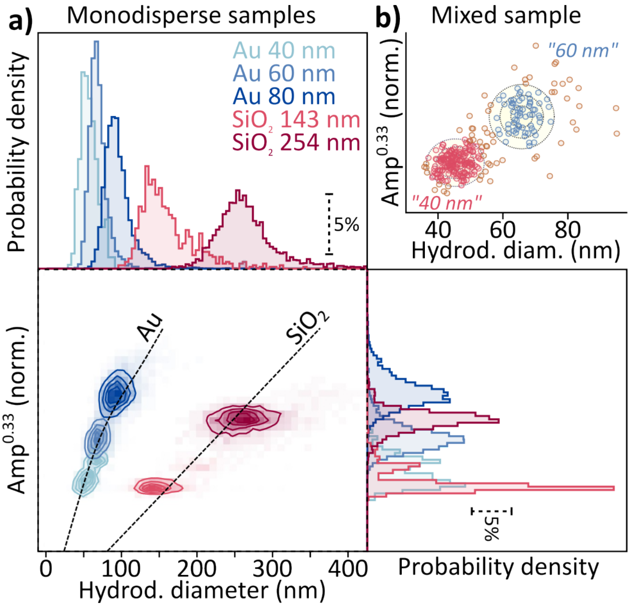

Figure 5.10, HoloNTA measurements of known samples. a) Experimental results obtained for holoNTA measurements of aqueous NP-dispersions for five different NP-samples. Normalised cube-root amplitudes are shown to account for the diameter-cube dependence of scattering amplitudes. The dashed lines show Mie-theory based scattering amplitudes for forward scattering of Au and SiO_2 NPs at 532 nm in water. b) Cube-root amplitude vs. hydrodynamic diameter plot obtained for a mixed sample containing 40 nm and 60 nm Au NPs. The rings represent the result of a fit to a bimodal distribution (sum of two Gaussians) with the representative rings indicating confidence intervals of 1, 2 and 3 standard deviations. All measurements were performed using identical illumination intensities and camera integration times (camera frame rate = 78 Hz, t_{exp} = 100 µs). Number of particles tracked: a: 320 (40 nm Au), 4394 (60 nm Au), 5249 (80 nm Au), 728 (143 nm SiO_2), 3050 (254 nm SiO_2) b: 310.

The results presented in Figure 5.10a are encouraging and suggest that holoNTA is well suited for directly inferring the size and dielectric constant of single nanoparticles without being biased by surface interactions or arrival-at sensing surface problems. However, most techniques are capable of accurately sizing monomodally distributed nanoparticle-samples but struggle with bi- or multi-modal distributions. HoloNTA is distribution unbiased as it determines the sample-characteristics by interrogating many individual particles. Figure 5.10b shows experimentally obtained results for a sample containing 40 nm and 60 nm GNPs alongside a bimodal normal distribution-based particle-classification, thus underlining that holoNTA is not limited to specific size-distributions.

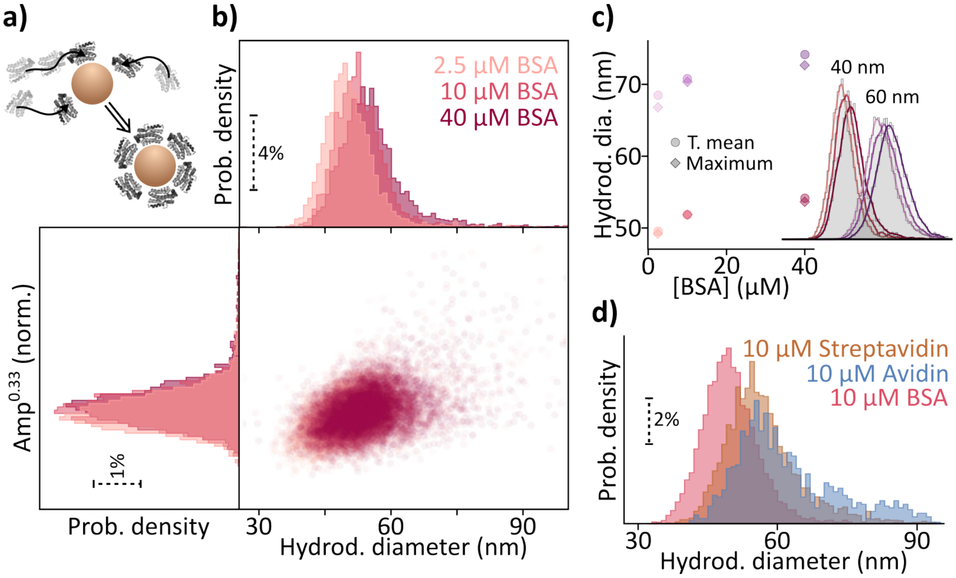

Figure 5.11, Sensing protein corona formation. a) Upon contact with biological fluid, particles are often coated in a so-called protein corona, a process that can dramatically alter the target-specificity of tailor-made nanodrugs. b) Holographic NTA reliably detects BSA protein-corona formation around 40 nm diameter Au NPs. c) The absolute hydrodynamic diameter-changes of 40 nm and 60 nm Au NPs are near-identical. All standard-deviations are <0.1 nm; no error bars are shown. d) Incubation with proteins of similar weight but different aspect-ratio results in markedly different hydrodynamic diameter shifts. All measurements were performed using identical illumination intensities and camera integration times (camera frame rate = 156 Hz, for each particle three measurements at integration times of t_{exp} = 20, 50 and 100 µs were combined). Number of particles tracked: b,c: 6694 (2.5 µM), 6352 (10 µM), 5906 (40 µM); d: 6352 (BSA), 1291 (avidin), 6352 (streptavidin). Hydrodynamic particle sizes (mean and standard error of the mean): b,c: 2.5 µM (49.16 ± 0.05 nm, 68.02 ± 0.08 nm), 10 µM (51.36 ± 0.05 nm, 70.34 ± 0.08 nm), 40 µM (53.64 ± 0.08 nm, 73.73 ± 0.09); d: BSA (51.36 ± 0.05 nm), avidin (57.1 ± 0.3 nm), streptavidin (54.91 ± 0.12 nm).

Following these validation experiments we conclude with holoNTA measurements of protein-corona formations around GNPs (Figure 5.11a), an often-encountered problem when nanoparticles come into contact with biological fluids. Due to the high protein concentrations in these fluids, the particles are coated with a protein layer: a serious problem for nanomedical applications as surface-bound target information is easily masked[199,200]. We form the protein coronas by diluting the proteins of interest in water to twice of the desired concentration and by mixing the dispersion at a 1:1 ratio with previously diluted GNPs, for a final concentration of 1.25×10^8 particle/mL. The solution then is incubated overnight.

Figure 5.11b shows holoNTA measurements of the corona-formation process for 40 nm GNPs incubated with different aqueous suspensions of bovine serum albumin (BSA) proteins. In agreement with our expectations, we observe an increase in both hydrodynamic diameter as well as in scattering amplitude with increasing BSA concentration.

To ensure that the hydrodynamic diameter change is not due to slight changes in fluid viscosity at increasing BSA concentrations, we compare the diameter changes for 40 nm and 60 nm GNPs (Figure 5.11c) with respect to the relative viscosity changes determined by the Krieger-Dougherty model[201]. Both particles exhibit similar absolute diameter increases, reminiscent of adsorption of a protein layer of identical thickness. The relative diameter changes are of 9% and 8% for 40 nm and 60 nm GNPs, respectively. Considering that maximum viscosity change for the employed BSA concentrations is less than 0.8%. Hence, considering the Stokes-Einstein equation[108], we can dismiss viscosity as the dominant parameter inducing the diameter shift.

Finally, we explore the hydrodynamic diameter changes for different proteins (BSA, avidin and streptavidin) with similar molecular weights but varying aspect ratio and surface charge. Considering the isoelectric point (pI) of said proteins, BSA (pI = 4.7) and streptavidin (pI = 5.0) are negatively charged in solution, whereas avidin (pI = 10.5) is positively charged. Albeit the difference in surface charge, the current hypothesis states that the protein binding to the negatively charged GNP surface is driven by the electrostatic interactions in between the particle and the positively charged amino acids present in all three proteins: lysine, arginine and histidine[202–204].

Figure 5.11d shows that the three proteins form a corona around 40 nm GNPs. Furthermore, despite identical incubation times and protein concentrations, the resulting nanoparticle protein corona complexes exhibit noticeably different hydrodynamic diameters even though the three proteins exhibit similar molecular weights. BSA, despite of being slightly heavier (66 kDa) than streptavidin (55 kDa) and similar to avidin (67-68 kDa), forms the smallest protein corona complexes. We can rationalise that the size difference in between streptavidin and avidin corona complexes is due to the different molecular weight. The higher degree of dispersion for avidin complexes could be due to the differences in protein surface charge. Specifically, avidin is more susceptible to non-specific interactions with the negatively charged GNPs[205], thus leading to larger protein corona formations. More detailed studies are required to characterise the type of protein-nanoparticles interactions, such as protein layer density or protein geometry. In particular in-situ single particle binding kinetics studies[206], for which holoNTA is ideally suited, offer a promising route to obtain this information.

5.6 Conclusion and outlook

To summarise, we experimentally implemented holographic nanoparticle tracking analysis (holoNTA), a much-needed extension of the extremely powerful and ubiquitously applied NTA methodology. HoloNTA simultaneously performs single-particle tracking and quantitative scattering measurements of freely diffusing (nano)particles. As a holographic technique, holoNTA readily accesses large 3D volumes-of-observation via digital hologram post-processing, which enables long-term observations for accurate and precise nanoparticle sizing. We highlighted the capabilities of holoNTA by measuring both monodisperse and mixed nanoparticle samples and observing protein-corona formation around small particles. Ultimately, holoNTA allows accessing the dielectric constant of individual nanoparticles, if pre-calibrated with a known reference material.

Conceptually, this work highlights a route to enhance the sizing precision by extending the length of individual particle trajectories. Specifically, we demonstrate this capability by increasing the total imaging volume by at least an order of magnitude compared to conventional NTA. As an alternative route, similar enhanced nanoparticle sizing performances have recently been achieved by either recording small imaging volumes at very high acquisition frame rates[207] or by combining high acquisition frame rates with 1D confinement inside a nanochannel[208]. It is important to remark that neither of these routes are mutually exclusive, i.e. large imaging volumes and high frame rate acquisition, and the main difference between them is how the track length increase scales with respect to the approach. In the case of volume extension, the average increase in trajectory length scales quadratically, whereas, improving the temporal resolution does so linearly. In principle, holoNTA is entirely compatible with high temporal resolution, as all experiments were performed with sensor integration times of 20-100 µs, analogous to Kashkanova, A. D *et al.*[207] and Špačková, B. *et al.*[208], which directly translates to >10 kHz frame rates. Our approach uses off-the shelf industrial sensors and does not require nanofabrication and as such we envision direct applications of our methodology for routine quantification and sizing in diverse fields of both fundamental and applied nature, ranging from heterogeneous catalysis over fundamental biology into the clinic.

Chapter 6:

Towards sub-nanometric sizing precision of individual free-floating nanoparticles

Nanoparticles can be designed for identifying and binding to target cells after being injected into our bodies. Such particles rely on active targeting, that is, on adding ligands onto their surface that specifically bind to a target receptor. However, once in contact with biological fluids, proteins bind non-specifically to those nanoparticles, forming protein-coronas and covering the ligands of interest. Here, to follow such binding events, we present a platform that confines individual free-floating particles into the volume-of-view of a holographic Nanoparticle Tracking Analysis (NTA) device. The combination of the 3D particle tracking with the extended holding times increases the NTA's sizing precision and enables the temporal characterization of the confined nanoparticles. As a validation, we characterize different gold nanoparticles and perform a thorough technical evaluation based on such measurements, reaching sizing uncertainties of ∼1% for holding times of 150 s.

6.1 Introduction

Recent advances in Nanomedicine involve the design of nanoparticles that, after being injected into our bodies, are able to identify and bind to target cells[209–212]. Once attached, the nanoparticle can, for example, release its cargo into the target cell or aid in the imaging of a specific tissue by enhancing the contrast. These nanoparticles rely on active targeting, which consists on adding ligands to their surfaces that specifically bind to a target receptor. However, the biological fluids contain proteins that can potentially attach to the nanodrug upon contact and form protein-coronas[199,200], which masks the ligands and drastically affect their circulation. The fundamental research of the protein-corona formation can potentially lead to new strategies for avoiding the protein binding[213].

The protein-corona formation is a dynamic process[203] and, thus, studying its temporal development is especially relevant. Such experiments would require the continuous characterization of nanoparticles in a protein solution. However, among the many available techniques[214], only few methods, such as dynamic light scattering (DLS)[65,68] and nanoparticle tracking analysis (NTA)[18,19], enable characterizing the protein-corona in the media of interest.

The continuous monitoring of a solution containing nanoparticles as well as proteins using both DLS and NTA would, in principle, indicate the temporal radius change of the particles and, thus, the protein-corona formation. However, the precision of the reported radial change would be limited. On the one hand, DLS cannot resolve individual particles’ radius due to its ensemble nature. In consequence, DLS can only report average statistics and, thus, would fail to detect potential heterogeneities in radius changes. On the other hand, due to the rapid diffusion of nanoparticles NTA would struggle at registering the individual particles’ radius changes and, hence, would effectively only report average statistics.

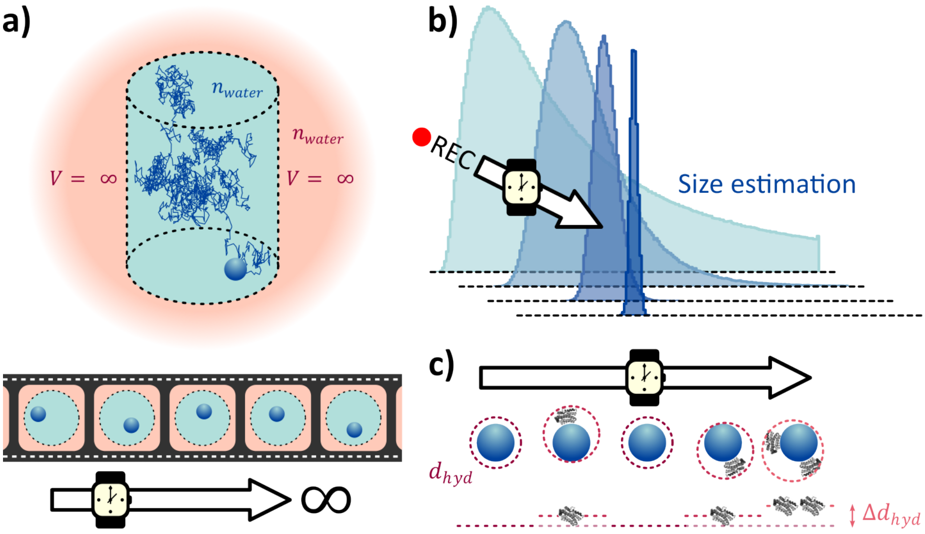

Figure 6.1, Concept. a) A nanoparticle is trapped in a microwell filled with water, where it freely moves. The refractive index of the potential walls matches the index of water. The particle does not leave the field-of-view, no matter recording time. b) NTA sizing gains precision with trajectory lengths. c) The hydrodynamic radius of a nanoparticle changes when a protein binds to it. Characterizing the particle's size over time reveals the radius change and, thus, indicates the protein adhesion.

Here, we address the challenges of capturing the protein-corona formation dynamics by presenting a platform that aims at improving the holographic NTA, holoNTA, capabilities. Such system confines individual free-floating nanoparticles in the volume-of-view of a microscope (Figure 6.1a) by trapping them into microwells. Sample videos are then recorded and particles' 3D-trajectories reconstructed. Because of particles' confinement, trajectory-lengths are not limited by the particles' diffusion but by the video duration. Hence, as shown in Figure 6.1b, the diffusion-based holoNTA's sizing precision is dramatically increased[105,195], beyond the limit for resolving the adsorption of an individual protein. Additionally, the fractionalization of such single particle long trajectories enables the detection of temporal changes in the particles' radius (Figure 6.1c).

6.2 Theoretical considerations

Chapter 5 already described how holoNTA measures the hydrodynamic radius of a nanoparticle by looking at its Brownian motion. In short, holoNTA extracts the diffusion coefficient, D, of the particles from the mean square displacement (MSD)

curve[20]. The precision of these measurements highly depends on the particles' trajectory time-points, N, and the reduced localization error, χ. The latter is defined as $\chi = \sigma^2/D\Delta t$, where σ refers to the static localisation uncertainty and Δt to the time in between two consecutive frames. In the regime of $\chi \ll 1$, i.e. the diffusion of the particles is much larger than the localization error, the sizing uncertainty scales as $\sqrt{1/N}$[105,195] and, hence, it tends to be negligible for infinitely long tracks. Confining a free-floating single particle in the field-of-view of a microscope using a microwell allows recording such long trajectories, as presented in this chapter.

6.3 Setup

A schematic of the employed holographic microscope is shown in Figure 6.2a. The output of a diode laser (*NLD521000G, Roithner Lasertechnik*) is divided into both the illumination and reference waves by a beam splitter. The former is focused into a water immersion objective (*UPLSAPO60XW/1.20, Olympus*) for widefield illumination. The sample, composed of a microwell array filled with water, is illuminated and scattered light collected. The microwell array and water are index-matched for minimizing the light scattered by the sample. A rod mirror, placed near the back-focal-plane of the objective, acts as a beam-stop[130,215] that blocks the lower angle contributions of the collected light in the *k*-space. Said light fraction is mostly composed of the reflections of the cover glass that holds the sample. An imaging lens projects the sample's scattered light onto the camera (*a2A1920-160umBAS, Basler*), in the form of real-space representation, where it interferes with the reference wave in an *off-axis* configuration. Figure 6.2b shows an as-detected hologram. The optical path lengths of both waves are matched, to ensure optimal interference contrast. Even though the coherence length of the laser being short, it covers the whole microwell depth. Hence, the holographically reconstructed volume covers the whole microwell.

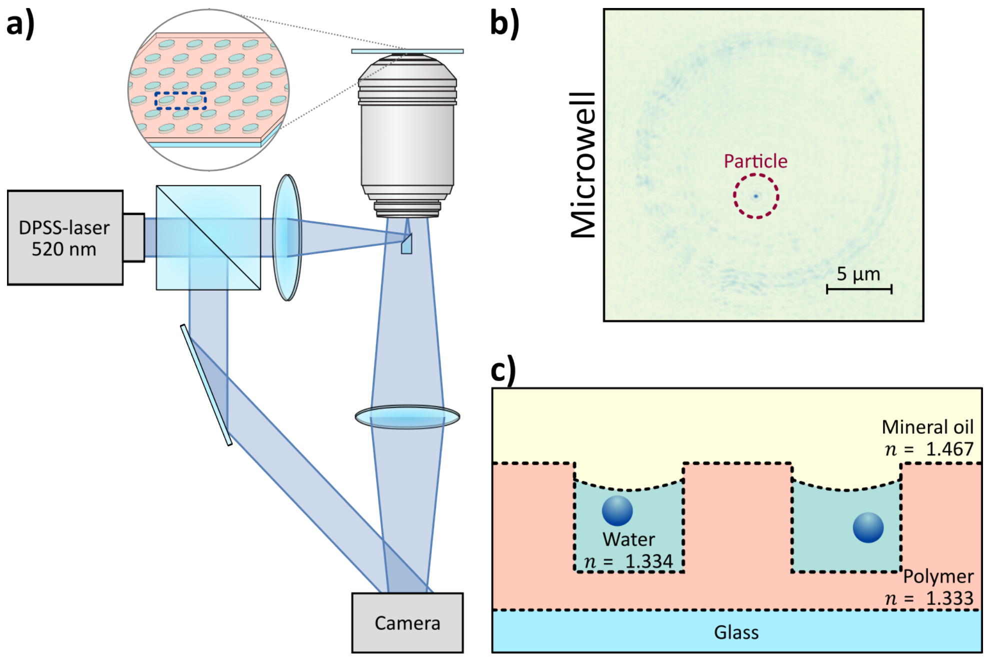

Figure 6.2, Setup. a) Schematic of the off-axis holographic microscope. Inset shows a drawing of a microwell array. b) As recorded microwell image. A nanoparticle, highlighted in maroon, is in the focal plane of the microscope. The image rings correspond to the background scattering signal generated by the microwell's walls. The image is normalized to the nanoparticle's maximum intensity. c) A magnified sketch of the nanoparticle trapping system.

Figure 6.2c depicts a magnified sketch of the microwell arrays that contain the trapped particles. In order to minimize the potential scattering signal and reflections originated from the illumination of the polymer-water interface, the microwells are composed of a polymer (*MY-133-V2000, My Polymers*; n=1.333) with a refractive index (n) similar to the one of water. Tests with another polymer of slightly higher n (*NOA 1348, Norland Products*; n=1.348), $\Delta n \sim 0.014$ with respect to water, led to larger background signals, indicating the importance of the refractive index-match. Additionally, the polymer layer on the bottom of the well ensures that the confined water does not spread across the polymer-glass interface.

The system is covered with oil in order to prevent the particle to leave the well. Initially, we planned to use $C_9H_5F_{15}O$ oil (*HFE-7500, 3M*; n=1.287) for minimizing the n difference in the oil-water interface. However, the polymer that we use for the microwells, as well as the tested alternative, are composed of fluorinated hydrocarbons and, hence, adsorb $C_9H_5F_{15}O$ oil. In consequence, the microwell arrays lose their conformation and detach from the glass. We decided to use mineral oil (*M8410, Merck*; *n*=1.467) for avoiding such issues.

Due to the *n* difference between the water and the mineral oil, the meniscus formed across their interface reflects light. In order to avoid collecting said light and, hence, reduce the background signal, we modify the meniscus curvature so that the reflected light is focused into the beam-stop. The curvature modification consists on a O_2 plasma treatment that alters the microwells' surface hydrophilicity[216] and, thus, the contact angle[217].

For trapping the particles, a solution of nanoparticles in water is added to the microwells. The system is then degassed for ensuring that the solution enters the microwells. Afterwards, the mineral oil is added and, due to its lower density (0.84 kg/L), it forms a layer above the solution. Finally, the solution in between the microwells and the oil-layer is removed by using a micropipette. The nanoparticle concertation must be adjusted to the desired particle-well ratio, which, in our case, consisted on a single nanoparticle per microwell.

We fabricate the microwell arrays by a two-step replica moulding process[218], which consist on first creating a negative mould, made of polydimethylsiloxane (PDMS), from a silicon-wafer master for the latter fabrication of the desired structures, the microwells. The PDMS negative moulds can be reused several times and its elasticity facilitates the peeling-off process, which would otherwise be challenging due to the rigidity of both the silicon-wafer and the glass-supported microwells.

We begin by preparing the PDMS moulds by soft lithography[219], whose fabrication is described in Figure 6.3a. First, the master is passivated by putting it under a fluorinated silane ($CF_3(CF_2)_5CH_2CH_2SiCl_3$) gas atmosphere for 30 min. Next, the PDMS (*Sylgard 184, DOW*) is casted onto the passivated surface and degassed for 1 h for removing the potential air bubbles. The PDMS is then cured at 80°C for 1 h, which grants the desired strength. Finally, the mould is released from the wafer.

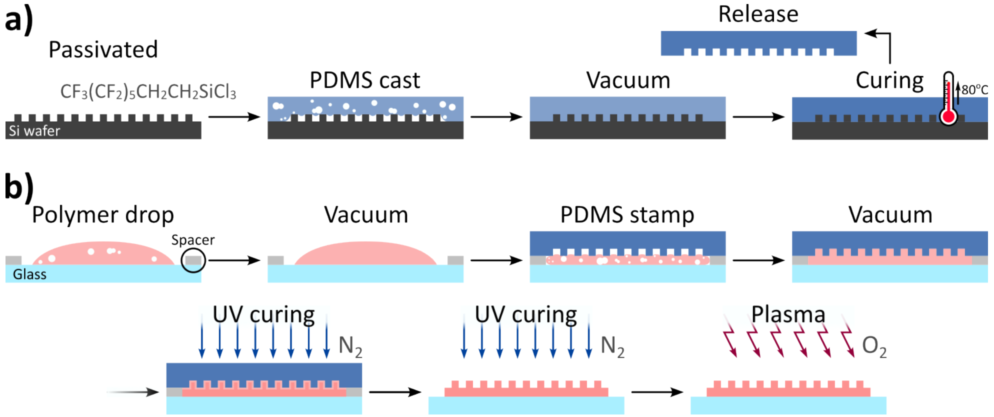

Figure 6.3, Microfabrication. a) PDMS stamp fabrication. First, a silicon wafer containing the microwell motifs is passivated with a fluorinated silane. The PDMS is then casted on the wafer and degassed. Finally, the PDMS is cured at 80°C and released from the wafer. b) Microwell array fabrication. First, a polymer drop is added on top of a cover-slide and the PDMS mould is placed above. The polymer is then degassed. Afterwards, the polymer is UV cured in a N_2 atmosphere. Next, the PDMS stamp is detached. Finally, the microwells are UV cured for a second time and then treated with O_2 plasma.

Once the negative mould is ready, we fabricate the microwell arrays as described in Figure 6.3b. First, a polymer drop is added on top of a glass cover slide and degassed for 20 min. A PDMS mould is then placed above the polymer and resulting sandwich degassed for 20 min. Two spacers avoid the direct contact of the microwell-motifs with the glass. Afterwards, the polymer is UV cured at 340 nm (*DUV340-SD353EL, Roithner Lasertechnik*) under N_2 atmosphere for 20 min. The PDMS mould is then released and the microwells are UV cured for another 2 min under N_2 atmosphere for ensuring the complete curing of the array's surface. Finally, the fabricated microwells are placed under O_2 plasma for 15 min. The plasma modifies the surface charge of the microwells and, thus, their hydrophilicity.

6.4 Data analysis

The holographic microscope implemented in this chapter is similar to the ones presented previously and, thus, they share the applicable hologram processing techniques. In addition, the NTA methodology of Chapter 4 is similar to the one explained below. However, in this chapter we aim at tracking particles and do not characterize the scattering cross-section of the nanoparticles and, hence, there is no need to correct the potential optical aberrations.

At a first glance, one can intuitively argue that omitting the optical aberration correction leads to a higher localization uncertainty and, thus, to a poorer size estimation by NTA. However, the simulations shown in Figure 6.4a indicate that the sizing uncertainty induced by the localization error is negligible for nanoparticles of high diffusion constants. Hence, the omission of the optical aberration correction simplifies the hologram processing without a significant impact on NTA's sizing precision.

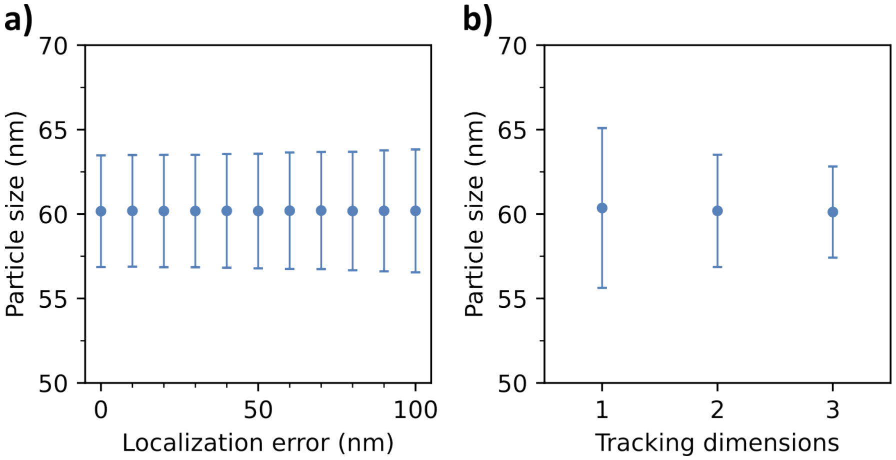

Figure 6.4, Simulations of the sizing error. The effect of the localization error (a) and trajectory dimensionality (b) on determining the particles' size. The simulations considered the diffusion of 60 nm particles in water (21°C). 100000 trajectories of 1000 time-points were simulated for each plot-point. The diffusion was extracted from a two-point MSD vs time curve. 2D trajectories and 0 nm localization error were considered for a) and b) respectively. Error bars correspond to one standard deviation.

Additionally, the simulations of Figure 6.4b show us the impact of the localizations' dimensionality on NTA's sizing precision. Although that the sizing uncertainty decreases when increasing the dimensionality, the precision gain is limited. According to the simulations

$$\sigma_{1D}/\sigma_{2D} = \sqrt{2} \tag{6.1}$$

and

$$\sigma_{2D}/\sigma_{3D} = \sqrt{3/2}$$

(6.2)

where σ_{1D}, σ_{2D} and σ_{3D} correspond to the standard deviations of the simulated size estimations for 1D, 2D and 3D, respectively. For the experiments reported in this chapter, we considered 2D localizations over the z-planes that contain the nanoparticles because we consider that the associated data analysis simplification compensates the gentle loss in precision.

Figure 6.5 shows the hologram processing and the particle localization methodology for videos containing a single nanoparticle. First, we Fourier transform the raw images, which decouples both the interferometric terms and the zero-order components. We then isolate one of the twin-images applying a hard-aperture function. Next, we 3D propagate the reconstructed image applying the angular spectrum method[137,138,141], yielding several image planes that describe the volume-of-view of the microscope. We repeat the process for all frames in the recorded video.

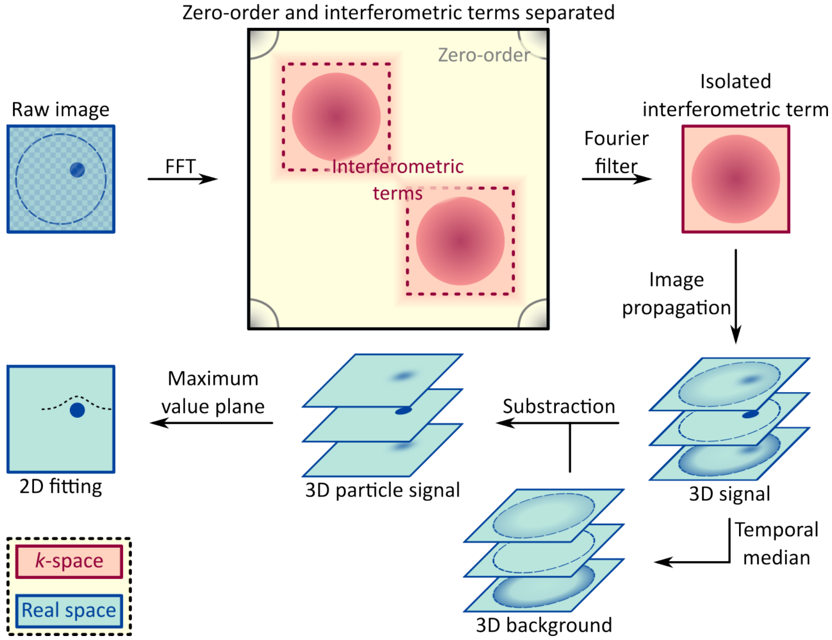

Figure 6.5, Hologram processing. First, the raw images are Fourier transformed for decoupling the zero-order and the interferometric terms. Next, a twin-image is isolated and propagated, yielding the microscope's volume-of-view. The process is then repeated for all the frames of the recorded video and, afterwards, the background 3D signal is calculated by applying a temporal median. To continue, the background 3D signal is removed from the reconstructed volume-of-view, which retrieves the particle´s 3D signal. Finally, the particle's focal plane is selected and its *xy* position retrieved by 2D fitting. Salmon colour refers to *k*-space while turquoise indicates real space.

To continue, we fractionalize the resulting 3D video into blocks of 1024 frames. We then apply a temporal median to each block for retrieving the 3D background. Afterwards, the 3D background is removed from the 3D frames, which yields particles' 3D signal. Fractionalizing the long videos accounts for the possible background changes that may occur.

Finally, we localize the trapped particle. First, we select the plane that contains the brightest pixel. We then add the signal of the two adjacent planes and fit a 2D Gaussian function for retrieving the particles *xy* position.

Once we retrieve the particle's localizations, we analyse them to identify potential mislocalizations. First, we identify the microwell boundaries by projecting all localizations into a 3D volume. We then discard the sparse localizations outside of the well. Finally, we calculate the particle's travel distance across consecutive frames and reject the unrealistic displacements.

Lastly, we determine the particle's hydrodynamic radius from the 2D MSD vs time[20,21] curve that we obtain from the particle's trajectory. In short, we get the diffusion coefficient from the slope of $MSD(t) = x_0^2 + 4Dt$. We only consider the first two points of said curve because our experimental conditions fulfil $\chi \ll 1$, i.e. the particle's displacement between consecutive frames is much larger than the localization uncertainty. As such, we can consider the localization error $\sim$0 and, thus, use the two curve points with better statistics[20,21]. We then transform the diffusion coefficient into the hydrodynamic radius applying the Stokes-Einstein equation[108]. For the temporal size estimations, the particles' trajectories were fractionalized and each division was independently analysed.

6.5 Experimental results

To experimentally validate our system, we first analyse the trajectories of the trapped particles for checking if they remain confined within the microwell. Figure 6.6a shows the 3D localizations of a single gold nanoparticle (GNP; *BBI Solutions*) over a video of $\sim$500 s. The discarded particle positions for said graph conform $\sim$1% of the total acquired particle positions. The particle's temporal position reveals the microwell's boundaries and, because all the localizations are inside such structure, we conclude that the particle remains confined. Interestingly, a closer inspection of the particle's trajectory, Figure 6.6b, reveals that the particle's position fluctuates inside a well's sub-region before displacing into a different one. Eventually, the particle moves around the whole microwell.

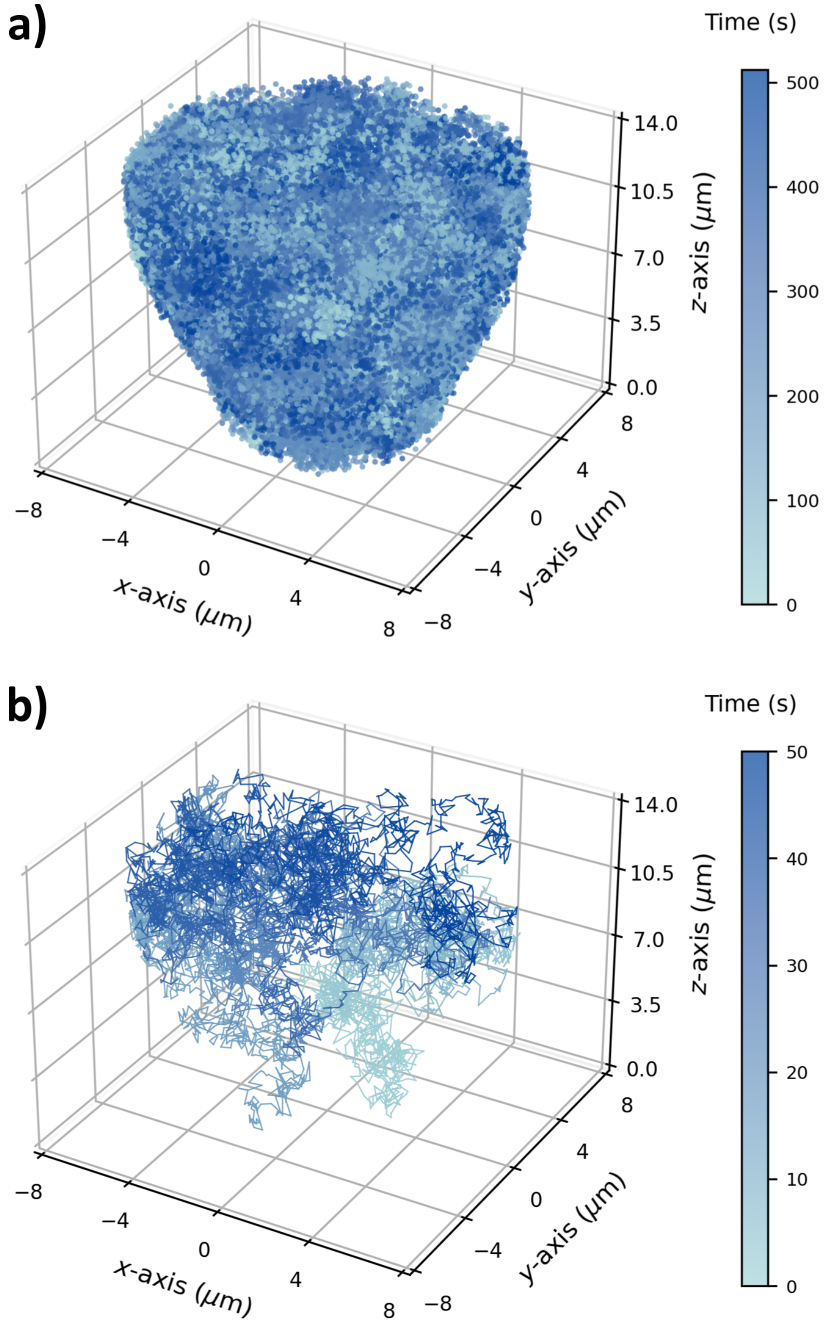

Figure 6.6, Particle localizations in a microwell. a) A particle's position as a function of time inside one microwell. Camera frame rate = 200 Hz, t_{exp} = 100 µs. 93684 time-points. b) A detailed view of the particle's trajectory shown in a), corresponding to the first 50 s. 9236 time-points.

Following the characterization of the microwell system, we now turn our attention to the potential effect of the wells' boundaries on the particles' diffusion. Specifically, we analyse the MSD of the particle from Figure 6.6 as a function of its position. Figure 6.7 shows MSD across the rotational plane of the microwell. If the particle's diffusion was affected, the MSD around the boundaries would be different to the inner one. However, we do not observe any difference. The higher noise around the rotational axis is due the lower well-volume and, thus, less localizations. Interestingly, the rotational plane shows the meniscus of oil-water interface.

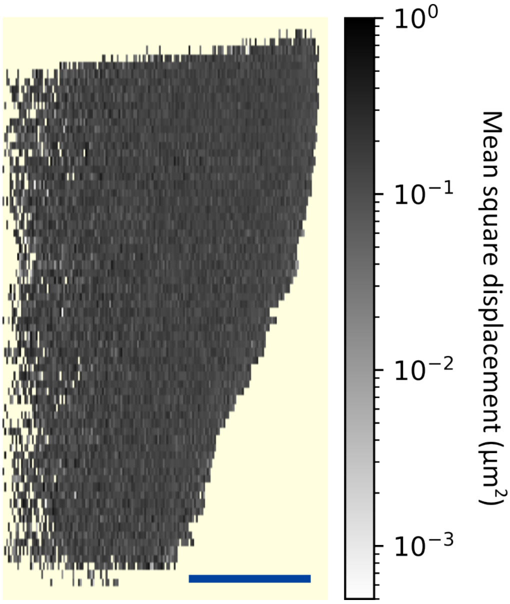

Figure 6.7, MSD as function of position. A particle's MSD over 5 ms as a function of its position on the rotational plane of the microwell. The scale bar corresponds to 3 µm. Camera frame rate = 200 Hz, t_{exp} = 100 µs.

We continue by sizing the trapped GNP. From the 2D MSD curve we determine a hydrodynamic diameter of 70.17 nm. According to the manufacturer, the mean diameter of the synthetized GNPs is 60 nm, with a coefficient of variation (CoV) of ≤8%. Hence, the reported GNP size is slightly high, which could be attributed to a small difference in temperature between the sample and the laboratory (21°C), that was the value considered for the size estimation. For example, a variation in temperature from 21°C to 23°C, and the correspondent water viscosity change, would translate into ~5.6% size difference. In addition, the hydrodynamic diameter refers to an uncharged spherical particle[109] and GNPs are negatively charged, which could also contribute to the reported size shift.

Interestingly, due to the trajectory's length, we can fractionalize it to experimentally analyse the effect of N on the particle's size estimation. Performing such analysis from a single particle's trajectory, in contrast to the ones based on nanoparticle-dispersions, is especially relevant because the potential bias due to the intrinsic size dispersity within particle-populations in avoided.

Figure 6.8a shows the hydrodynamic diameters measured for trajectory fractions of 10, 100, 1000 and 10000 time-points. We see that short trajectories yield wide Rayleigh probability density functions, indicating that NTA measurements of monodisperse nanoparticle samples can lead to a broad size-distribution if a minimum N is not considered. Additionally, the retrieved function's mean does not accurately indicate the particle size. A relatively moderate increase of N results in more accurate size distributions. Once the size-distribution function accurately indicates the particle's diameter, increasing N leads to a higher precision and moderate gains in accuracy.

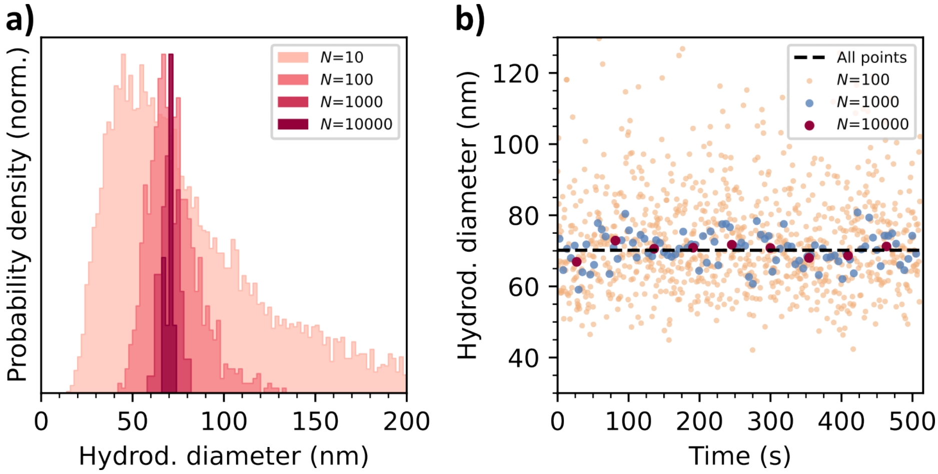

Figure 6.8, Effect of trajectory lengths. a) Histograms showing the estimated hydrodynamic diameter of a nanoparticle obtained by fractionalizing its trajectory. Colouring indicates N. b) Particle sizing estimates from (a) as a function of time. Dashed line indicates the estimation obtained using all trajectory points. Camera frame rate = 200 Hz, t_{exp} = 100 µs. $\chi = 0.04$.

Now, we turn our attention to the temporal sizing capacities of the microwells. Figure 6.8b shows the size estimates of Figure 6.8a as a function of time. We observe a constant sizing over time regardless of N. However, the sizing precision increases with N and, thus, the capacity of detecting potential temporal changes in particles' diffusion.

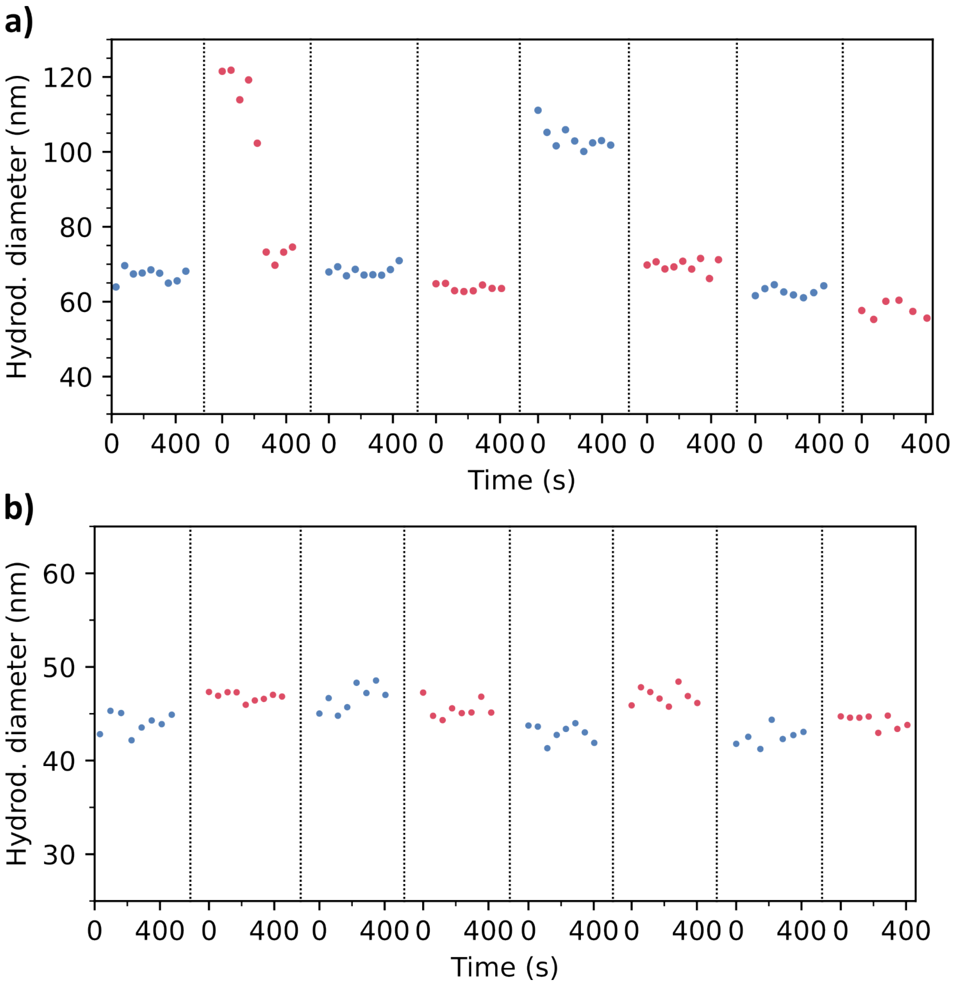

Figure 6.9, Nanoparticle characterization. Temporal hydrodynamic size measurements for different GNPs with, according to the manufacturer, diameters of around 60 (a) and 40 (b) nm. Alternate colours indicate different particles. 10000 time-points per size estimation. Camera frame rate = 200 Hz, t_{exp} = 100 µs. Measurement uncertainties, corresponding to one standard deviation calculated from the provided measurements, for the different particles from left to right are 2.75%, 24.3%, 1.96%, 1.38%, 3.15%, 2.40%, 2.01% and 3.75% for (a); and 2.54%, 0.98%, 3.02%, 2.23%, 2.19%, 2.03%, 2.33% and 1.61% for (b).

We continue the technical characterization of the microwells' sizing capacities by analysing the sizing estimations for different nanoparticles. Figure 6.9a shows the temporal measurements, of about 500 s, of the hydrodynamic diameters of 8 GNPs individually trapped in different wells. The first particle measurements correspond to the previously analysed GNP. The graph shows constant sizing across and within particles, except for the second and the fifth particle. Interestingly, the second particle shows a size-shift, indicating a change in particle´s behaviour. The size estimates for the fifth particle are similar to the initial ones of the second GNP, suggesting that the behaviour of both the second and the fifth nanoparticles could be biased by the microwell. Similarly, Figure 6.9b shows the temporal size estimation for 8 different GNPs, where we observe a constant size across and within the GNPs.

According to the manufacturer, the average size of the synthetized GNPs used in Figure 6.9a and b is of 60 and 40 nm ($CoV \leq 8\%$), respectively. Excluding the second and the fifth GNPs from Figure 6.9a, all particles' hydrodynamic radii are slightly higher than the manufacturer's specifications, which could be attributed to a temperature mismatch and to the surface charge of the particles, as discussed above. However, the most important remark form Figure 6.9 is the constant temporal sizing within particles, which indicates sizing stability.

We conclude the technical characterization of the platform by analysing its sizing uncertainty, σ_d/d, which refers to the ratio between the measured particle-diameters, d, and the standard deviation of such measurements, σ_d. Figure 6.10 shows σ_d/d for the particles of Figure 6.9a as a function of N.

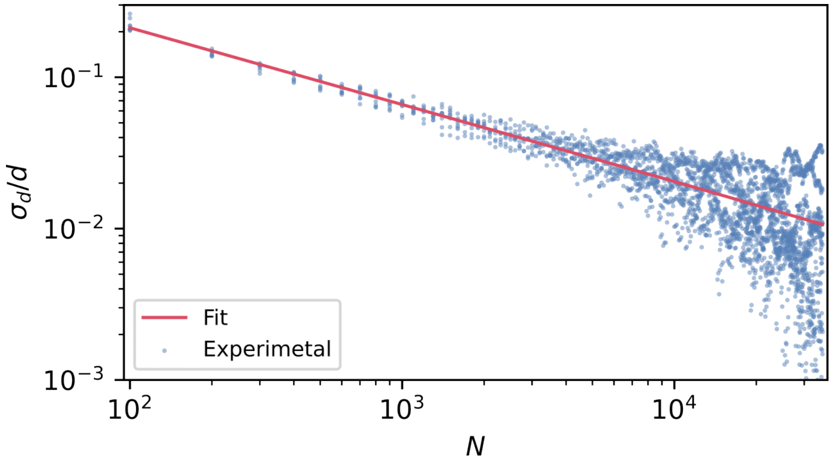

Figure 10, Platform's sizing uncertainty. σ_d/d of the hydrodynamic diameter measurements for 40 nm GNPs as a function of N. Dots and solid line indicate experimental values and fit, respectively. Camera frame rate = 200 Hz, t_{exp} = 100 µs.

The graph reveals that $\sigma_d/d = 2.1/\sqrt{N}$. Hence, we can estimate the N needed to detect the one-dimensional hydrodynamic diameter change induced by the adsorption of a single protein onto a nanoparticle. For a signal to noise ratio of 3, i.e. a change in the particle's size of 3 times the sizing uncertainty, the sizing uncertainty must satisfy

$$\sigma_d/d \leq \frac{\delta V}{3V}, \tag{6.3}$$

where δV refers to the volume change, i.e. the protein size, and V to the particle one. For example, for detecting the volume shift induced by the absorption of a BSA protein, modelled as a prolate spheroid with 14 and 4 nm axes[220], onto a 20 nm GNP, we would need to measure the temporal size of the particle using 51000 time-points per estimate. For the experimental frame-rate, 200 Hz, such trajectory length corresponds to ~4 min. However, considering $\chi \ll 1$, the sizing uncertainty does not depend on the frame-rate but just on N. Hence, high-speed cameras can dramatically reduce the trajectory time-periods and, thus, improve the temporal resolution. For example, a frame-rate of 1 kHz can gather such amount of data points in 51 s, whereas a 1 kHz camera would need just 5 s.

6.6 Conclusion and outlook

To summarise, we experimentally implemented a nanoparticle trap that further improves the sizing precision of holographic nanoparticle tracking analysis (holoNTA), up to what would be needed for detecting the adsorption of a single protein onto a particle. Conceptually, we presented a microwell-based system that effectively confines nanoparticles in the field-of-view of a microscope, while adding little background-signal, for recording extended nanoparticle trajectories.

We demonstrated the feasibility of the system by analysing a nanoparticle's trajectory inside one microwell. We showed that the particles remain confined and characterized the potential effects of the microwells' boundaries over the particles' diffusion. Moreover, we experimentally reported the effect of the trajectory lengths on particle-sizing by fractionalizing a long trajectory. That approach measures a single particle and, thus, avoids the potential bias that the intrinsic polydispersity of nanoparticle-populations induces. We finalize the technical characterization of the microwell system by testing the stability of the measurements, which was done by comparing the temporal sizing of different particles, and quantifying the uncertainty of the measurements.

Trapping free-floating single nanoparticles not only enables a dramatical increase on holoNTA’s sizing precision, but also points toward novel measurements. Being able to measure the temporal hydrodynamic radius permits, for instance, the study of particles’ response towards temperature changes or to characterize the protein adsorption onto a nanoparticle’s surface. Hence, we foresee that the presented microwell-based sizing system can play a key-role in the fundamental research of protein-corona formation, especially if combined with high-speed cameras for reaching higher temporal resolutions.

Chapter 7:

Conclusion and outlook

In this thesis I have explored the use of holographic microscopes for characterizing nanoparticles in a label-free manner. In particular, I focused on microscope-designs that interfere two non-parallel light waves, because they facilitate the phase retrieval and, hence, the wavefront reconstruction. I used such microscopes to record the scattering signal of several nanoparticle-populations and, after processing the holograms, I measured their size-distributions by quantifying the scattering amplitude or by analysing the particles' diffusion. Additionally, I was able to retrieve the refractive index of the particles by combining the amplitude quantification with the diffusion analysis.

First, I developed a holographic microscope, the *k*-scope, that is able to successfully measure polydisperse nanoparticle populations by quantifying the scattering amplitude. Traditional optical microscopes suffer from sensor saturation when they measure the scattering signal of such samples, due to the dramatic size-signal scaling. The design I presented, in contrast, overcomes that limitation by imaging the *k*-space plane of the system, where the diffraction-limited signals spread and, thus, local sensor-saturations are avoided.

I demonstrated the sizing capabilities of the *k*-scope by sizing dry polydisperse populations of particles made of gold and silica. Moreover, I showed that calibration curves can be scaled to fit the signal-scaling of different materials by adjusting the refractive index. Additionally, I presented initial proof-of-concept measurements employing extracellular vesicles, showing the platform's potential for clinical applications.

I foresee the combination of the *k*-scope with antibody-covered substrates for developing diagnosis platforms. The high sensibility, extended dynamic-range and low data processing times, combined with the relatively low cost of the system, make the *k*-scope suitable for fast and reliable point-of-care systems. In that regard, I find particularly interesting the potential synergies between the *k*-scope and lab-on-chip technologies.

Secondly, I implemented a holographic microscope that is able to perform nanoparticle tracking analysis (NTA), that is to size free-floating particles by examining their diffusion. The precision of such measurements depends on the recorded trajectory lengths and, hence, the time the nanoparticles stay in the volume-of-view. Typically, microscopes provide a quasi-2D volume-of-view and, thus, fail to capture the 3D movement of particles, which results in a limited NTA precision. Holographic NTA (holoNTA) implementations, in contrast, effectively expand the volume-of-view thanks to the capacity to propagate the reconstructed wavefront, which leads to recording longer particle trajectories. In addition, holoNTA is able to simultaneously characterize the scattering signal from each nanoparticle to retrieve the refractive index. Moreover, holoNTA is fully compatible with *k*-space imaging for extending the dynamic range.

I showed the particle characterization capabilities of holoNTA by measuring the size and refractive index of gold and silica nanoparticle dispersions. In terms of sizing precision, the coefficient of variation of the measurements was equal to the one provided by the manufacturer, which indicates that holoNTA was able to describe the intrinsic dispersion of the particle-populations. Moreover, I was able to measure the radial increase induced by the formation of a protein corona. In that regard, I reported different radial shifts for different proteins, which evinces the system's high sensitivity.

Considering that, in principle, traditional and holographic NTA share the application scope, one can easily anticipate several usage scenarios for holoNTA. In that regard, both routine particle characterization and fundamental research could benefit from the increased precision and refractive index retrieval of holoNTA. In particular, due to the longer data-processing times, holoNTA best suits the scenarios where precision is preferred to speed.

Finally, I presented a microwell-based sizing platform that confines nanoparticles in the volume-of-view of a microscope for increasing the recorded track lengths and, hence, the sensitivity of holoNTA. I demonstrated the sizing potential of such platform by characterizing gold nanoparticles and, more importantly, I quantified the system's precision. Given the long trajectories that were recorded, I could fractionalize them for retrieving the temporal size of the particles.

Considering the microwell-based platform's ability to detect temporal shifts on particles' diameter, I believe that fundamental research on biological dynamic events could benefit from using such system. In particular, I foresee the platform's use in nanomedice for characterizing the protein corona formation around drug nanocarriers and for studying the antibody binding to ligands on nanoparticles' surfaces.

With those achievements I believe to have contributed to the design of new nanoparticle characterization platforms. In particular, I presented label-free techniques that tackle the challenges that sizing polydisperse-populations entails and, in addition, provide high sensitivity on a single nanoparticle level. I am eager to see the potential adoption of such particle sizing platforms.

Acknowledgements

First of all, I want to thank Niek for giving me the opportunity to join his group at ICFO and conduct the research I present in this thesis. I feel very grateful for his continuous support, guidance and the freedom he provided, so that I could find my own scientific path. I especially appreciate the opportunities that he gave me to present my research at different conferences, which somehow made me feel that my work was fruitful.

I am tremendously grateful to Matz for his continuous help (and patience) during all these years. He provided me tons of knowledge, support and guidance. I feel particularly thankful for his trust in me to develop his scientific ideas. It was a pleasure to work together.

Further thanks to Ala Jo, Hakho Lee and Romain Quidant for their contributions to this thesis. Special thanks to Jaime for giving me the opportunity to develop the holoNTA and for his scientific guidance, in addition to his contributions. Thanks also to ICFO facilities, that made my research work smoother, and to Lucía Cámara for the fantastic cover.

I also want to thank the entire Molecular Nanophotonic Research group, for the great working environment and the scientific support they provided. To the past members, AlexB, AlexD, Esther, Ion, James, Lisa, Monse, Nick, Nicola, Richard, Sylwester, Vikas, and to the current members, Luca, Giulia, Guille, Jana, Joe, Sandra and Saurabh.

I also want to thank the public education system. From the day I joined the elementary school till my PhD defence, I studied in public intuitions and, hence, this thesis work is the result of public teaching. In this regard, I want to thank the numerous teachers and professors I had during all my student stages.

Finalmente, quiero dedicar unas líneas para agradecer el apoyo recibido por familiares y amig@s durante todos estos años. Se me hace complicado imaginar este trabajo sin su constante cariño. Para no estirar el texto más de lo necesario, y para no olvidarme a nadie, no mencionaré nombres. Tengo la certeza de que las personas apeladas se darán por aludidas.

Primero de todo, agradecer el apoyo incondicional a mis padres, Esther y Carlos. Sé que ellos se han esforzado mucho para que yo hoy esté dónde estoy. Quiero darle también las gracias a mi hermana, Garazi, que siempre ha estado ahí cuando la he necesitado. Y cómo olvidar a mis abuel@s, Esther, Jesús, José y Pruden, que tanto se han preocupado por mí durante tantos años. También quiero agradecer el cariño de mis tí@s y prim@s, con una mención especial a Guille, José, José Luis, Julen, Lourdes y Luci por facilitar tanto mi estancia en Barcelona.

A mis amig@s de Vitoria les estoy tremendamente agradecido por todo el esfuerzo que han hecho para que la distancia que nos separa no sea impedimento de nada. A mi gente de Revilla les agradezco todos los buenos momentos de verano que tanta energía me han dado para retomar el laboratorio con ganas. A las amistades de Barcelona les digo que sin vosotr@s mi estancia aquí no hubiese tenido sentido y, por tanto, me hubiese vuelto a Vitoria antes de empezar el PhD.

Bibliography

1. Mertz, J. Monochromatic Field Propagation Through a Lens. in *Introduction to Optical Microscopy* (ed. Mertz, J.) 33–48 (Cambridge University Press, 2019). doi:DOI: 10.1017/9781108552660.005.

2. López-Serrano, A., Olivas, R. M., Landaluze, J. S. & Cámara, C. Nanoparticles: a global vision. Characterization, separation, and quantification methods. Potential environmental and health impact. *Anal. Methods* **6**, 38–56 (2014).

3. Mourdikoudis, S., Pallares, R. M. & Thanh, N. T. K. Characterization techniques for nanoparticles: comparison and complementarity upon studying nanoparticle properties. *Nanoscale* **10**, 12871–12934 (2018).

4. Modena, M. M., Rühle, B., Burg, T. P. & Wuttke, S. Nanoparticle Characterization: What to Measure? *Advanced Materials* **31**, 1901556 (2019).

5. Jacobsen, V., Stoller, P., Brunner, C., Vogel, V. & Sandoghdar, V. Interferometric optical detection and tracking of very small gold nanoparticles at a water-glass interface. *Opt Express* **14**, 405 (2006).

6. Hsieh, C.-L., Spindler, S., Ehrig, J. & Sandoghdar, V. Tracking Single Particles on Supported Lipid Membranes: Multimobility Diffusion and Nanoscopic Confinement. *J Phys Chem B* **118**, 1545–1554 (2014).

7. de Wit, G., Albrecht, D., Ewers, H. & Kukura, P. Revealing Compartmentalized Diffusion in Living Cells with Interferometric Scattering Microscopy. *Biophys J* **114**, 2945–2950 (2018).

8. Cheng, C.-Y., Liao, Y.-H. & Hsieh, C.-L. High-speed imaging and tracking of very small single nanoparticles by contrast enhanced microscopy. *Nanoscale* **11**, 568–577 (2019).

9. Spindler, S. *et al.* Visualization of lipids and proteins at high spatial and temporal resolution via interferometric scattering (iSCAT) microscopy. *J Phys D Appl Phys* **49**, 274002 (2016).

10. Huang, Y.-F. *et al.* Coherent Brightfield Microscopy Provides the Spatiotemporal Resolution to Study Early Stage Viral Infection in Live Cells. *ACS Nano* **11**, 2575–2585 (2017).

11. Huang, Y.-F., Zhuo, G.-Y., Chou, C.-Y., Lin, C.-H. & Hsieh, C.-L. Label-free, ultrahigh-speed, 3D observation of bidirectional and correlated intracellular cargo transport by coherent brightfield microscopy. *Nanoscale* **9**, 6567–6574 (2017).

12. Liebel, M., Hugall, J. T. & van Hulst, N. F. Ultrasensitive Label-Free Nanosensing and High-Speed Tracking of Single Proteins. *Nano Lett* **17**, 1277–1281 (2017).

13. Young, G. *et al.* Quantitative mass imaging of single biological macromolecules. *Science (1979)* **360**, 423–427 (2018).

14. Gabor, D. Holography, 1948-1971. *Science (1979)* **177**, 299–313 (1972).

15. Kim, M. K. Principles of Holography. in *Digital Holographic Microscopy: Principles, Techniques, and Applications* (ed. Kim, M. K.) 29–42 (Springer New York, 2011). doi:10.1007/978-1-4419-7793-9_3.

16. Schnars, U., Falldorf, C., Watson, J. & Jüptner, W. Introduction. in *Digital Holography and Wavefront Sensing: Principles, Techniques and Applications* (eds. Schnars, U., Falldorf, C., Watson, J. & Jüptner, W.) 1–4 (Springer Berlin Heidelberg, 2015). doi:10.1007/978-3-662-44693-5_1.

17. Goodman, J. W. Frequency Analysis of Optical Imaging Systems. in *Introduction to Fourier Optics* 126–171 (McGraw-Hill, 1996).

18. Schätzel, K., Neumann, W.-G., Müller, J. & Materzok, B. Optical tracking of single Brownian particles. *Appl Opt* **31**, 770 (1992).

19. Garbow, N., Müller, J., Schätzel, K. & Palberg, T. High-resolution particle sizing by optical tracking of single colloidal particles. *Physica A: Statistical Mechanics and its Applications* **235**, 291–305 (1997).

20. Michalet, X. Mean square displacement analysis of single-particle trajectories with localization error: Brownian motion in an isotropic medium. *Phys Rev E* **82**, 41914 (2010).

21. Michalet, X. & Berglund, A. J. Optimal diffusion coefficient estimation in single-particle tracking. *Phys Rev E* **85**, 61916 (2012).

22. van der Pol, E., Boing, A. N., Harrison, P., Sturk, A. & Nieuwland, R. Classification, Functions, and Clinical Relevance of Extracellular Vesicles. *Pharmacol Rev* **64**, 676–705 (2012).

23. Colombo, M., Raposo, G. & Théry, C. Biogenesis, Secretion, and Intercellular Interactions of Exosomes and Other Extracellular Vesicles. *Annu Rev Cell Dev Biol* **30**, 255–289 (2014).

24. van Niel, G., D'Angelo, G. & Raposo, G. Shedding light on the cell biology of extracellular vesicles. *Nat Rev Mol Cell Biol* **19**, 213–228 (2018).

25. Erni, R., Rossell, M. D., Kisielowski, C. & Dahmen, U. Atomic-Resolution Imaging with a Sub-50-pm Electron Probe. *Phys Rev Lett* **102**, 96101 (2009).

26. Orlova, E. v & Saibil, H. R. Structural Analysis of Macromolecular Assemblies by Electron Microscopy. *Chem Rev* **111**, 7710–7748 (2011).

27. Anderson, W., Kozak, D., Coleman, V. A., Jämting, Å. K. & Trau, M. A comparative study of submicron particle sizing platforms: Accuracy, precision and resolution analysis of polydisperse particle size distributions. *J Colloid Interface Sci* **405**, 322–330 (2013).

28. Egerton, R. F. The Transmission Electron Microscope. in *Physical Principles of Electron Microscopy: An Introduction to TEM, SEM, and AEM* (ed. Egerton, R. F.) 55–88 (Springer International Publishing, 2016). doi:10.1007/978-3-319-39877-8_3.

29. Zhou, W. & Greer, H. F. What Can Electron Microscopy Tell Us Beyond Crystal Structures? *Eur J Inorg Chem* **2016**, 941–950 (2016).

30. Schorb, M., Haberbosch, I., Hagen, W. J. H., Schwab, Y. & Mastronarde, D. N. Software tools for automated transmission electron microscopy. *Nat Methods* **16**, 471–477 (2019).

31. Egerton, R. F. The Scanning Electron Microscope. in *Physical Principles of Electron Microscopy: An Introduction to TEM, SEM, and AEM* (ed. Egerton, R.

F.) 121–147 (Springer International Publishing, 2016). doi:10.1007/978-3-319-39877-8_5.

32. Venables, J. A. & Harland, C. J. Electron back-scattering patterns—A new technique for obtaining crystallographic information in the scanning electron microscope. *The Philosophical Magazine: A Journal of Theoretical Experimental and Applied Physics* **27**, 1193–1200 (1973).

33. Rades, S. *et al.* High-resolution imaging with SEM/T-SEM, EDX and SAM as a combined methodical approach for morphological and elemental analyses of single engineered nanoparticles. *RSC Adv.* **4**, 49577–49587 (2014).

34. Grubb, D. T. Radiation damage and electron microscopy of organic polymers. *J Mater Sci* **9**, 1715–1736 (1974).

35. Bergmans, L., Moisiadis, P., van Meerbeek, B., Quirynen, M. & Lambrechts, P. Microscopic observation of bacteria: review highlighting the use of environmental SEM. *Int Endod J* **38**, 775–788 (2005).

36. KIRK, S. E., SKEPPER, J. N. & DONALD, A. M. Application of environmental scanning electron microscopy to determine biological surface structure. *J Microsc* **233**, 205–224 (2009).

37. Abdullah, S. Z., Bérubé, P. R. & Horne, D. J. SEM imaging of membranes: Importance of sample preparation and imaging parameters. *J Memb Sci* **463**, 113–125 (2014).

38. Nanou, A., Crespo, M., Flohr, P., de Bono, J. S. & Terstappen, L. W. M. M. Scanning Electron Microscopy of Circulating Tumor Cells and Tumor-Derived Extracellular Vesicles. *Cancers (Basel)* **10**, (2018).

39. Delvallée, A., Feltin, N., Ducourtieux, S., Trabelsi, M. & Hochepied, J. F. Direct comparison of AFM and SEM measurements on the same set of nanoparticles. *Meas Sci Technol* **26**, 085601 (2015).

40. Binnig, G., Quate, C. F. & Gerber, Ch. Atomic Force Microscope. *Phys Rev Lett* **56**, 930–933 (1986).

41. Meyer, E. Atomic force microscopy. *Prog Surf Sci* **41**, 3–49 (1992).

42. Giessibl, F. J. Advances in atomic force microscopy. *Rev Mod Phys* **75**, 949–983 (2003).

43. Putman, C. A. J., van der Werf, K. O., de Grooth, B. G., van Hulst, N. F. & Greve, J. Tapping mode atomic force microscopy in liquid. *Appl Phys Lett* **64**, 2454–2456 (1994).

44. Hofer, W. A., Foster, A. S. & Shluger, A. L. Theories of scanning probe microscopes at the atomic scale. *Rev Mod Phys* **75**, 1287–1331 (2003).

45. Junno, T., Deppert, K., Montelius, L. & Samuelson, L. Controlled manipulation of nanoparticles with an atomic force microscope. *Appl Phys Lett* **66**, 3627–3629 (1995).

46. Canet-Ferrer, J., Coronado, E., Forment-Aliaga, A. & Pinilla-Cienfuegos, E. Correction of the tip convolution effects in the imaging of nanostructures studied through scanning force microscopy. *Nanotechnology* **25**, 395703 (2014).

47. Hansma, H. G. & Hoh, J. H. Biomolecular Imaging with the Atomic Force Microscope. *Annu Rev Biophys Biomol Struct* **23**, 115–140 (1994).

48. Dufrêne, Y. F. *et al.* Imaging modes of atomic force microscopy for application in molecular and cell biology. *Nat Nanotechnol* **12**, 295–307 (2017).

49. Piontek Melissa C. and Roos, W. H. Atomic Force Microscopy: An Introduction. in *Single Molecule Analysis: Methods and Protocols* (ed. Peterman, E. J. G.) 243–258 (Springer New York, 2018). doi:10.1007/978-1-4939-7271-5_13.

50. Vorselen, D., Piontek, M. C., Roos, W. H. & Wuite, G. J. L. Mechanical Characterization of Liposomes and Extracellular Vesicles, a Protocol. *Front Mol Biosci* **7**, (2020).

51. Maivald, P. *et al.* Using force modulation to image surface elasticities with the atomic force microscope. *Nanotechnology* **2**, 103–106 (1991).

52. Vinckier, A. & Semenza, G. Measuring elasticity of biological materials by atomic force microscopy. *FEBS Lett* **430**, 12–16 (1998).

53. Nonnenmacher, M., O'Boyle, M. P. & Wickramasinghe, H. K. Kelvin probe force microscopy. *Appl Phys Lett* **58**, 2921–2923 (1991).

54. Fujihira, M. KELVIN PROBE FORCE MICROSCOPY OF MOLECULAR SURFACES. *Annual Review of Materials Science* **29**, 353–380 (1999).

55. Martin, Y. & Wickramasinghe, H. K. Magnetic imaging by '"force microscopy"' with 1000 Å resolution. *Appl Phys Lett* **50**, 1455–1457 (1987).

56. Hartmann, U. MAGNETIC FORCE MICROSCOPY. *Annual Review of Materials Science* **29**, 53–87 (1999).

57. Kikhney, A. G. & Svergun, D. I. A practical guide to small angle X-ray scattering (SAXS) of flexible and intrinsically disordered proteins. *FEBS Lett* **589**, 2570–2577 (2015).

58. Li, T., Senesi, A. J. & Lee, B. Small Angle X-ray Scattering for Nanoparticle Research. *Chem Rev* **116**, 11128–11180 (2016).

59. Polte, J. *et al.* Nucleation and Growth of Gold Nanoparticles Studied via in situ Small Angle X-ray Scattering at Millisecond Time Resolution. *ACS Nano* **4**, 1076–1082 (2010).

60. Fleury, B. *et al.* Gold Nanoparticle Internal Structure and Symmetry Probed by Unified Small-Angle X-ray Scattering and X-ray Diffraction Coupled with Molecular Dynamics Analysis. *Nano Lett* **15**, 6088–6094 (2015).

61. Boldon, L., Laliberte, F. & Liu, L. Review of the fundamental theories behind small angle X-ray scattering, molecular dynamics simulations, and relevant integrated application. *Nano Rev* **6**, 25661 (2015).

62. Graewert, M. A. & Jeffries, C. M. Sample and Buffer Preparation for SAXS. in *Biological Small Angle Scattering: Techniques, Strategies and Tips* (eds. Chaudhuri, B., Muñoz, I. G., Qian, S. & Urban, V. S.) 11–30 (Springer Singapore, 2017). doi:10.1007/978-981-10-6038-0_2.

63. Li, T., Senesi, A. J. & Lee, B. Small Angle X-ray Scattering for Nanoparticle Research. *Chem Rev* **116**, 11128–11180 (2016).

64. Foord, R. *et al.* Determination of Diffusion Coefficients of Haemocyanin at Low Concentration by Intensity Fluctuation Spectroscopy of Scattered Laser Light. *Nature* **227**, 242–245 (1970).

65. Goldburg, W. I. Dynamic light scattering. *Am J Phys* **67**, 1152–1160 (1999).

66. Lim, J., Yeap, S. P., Che, H. X. & Low, S. C. Characterization of magnetic nanoparticle by dynamic light scattering. *Nanoscale Res Lett* **8**, 381 (2013).

67. Gast, K., Damaschun, G., Misselwitz, R. & Zirwer, D. Application of dynamic light scattering to studies of protein folding kinetics. *European Biophysics Journal* **21**, 357–362 (1992).

68. Stetefeld, J., McKenna, S. A. & Patel, T. R. Dynamic light scattering: a practical guide and applications in biomedical sciences. *Biophys Rev* **8**, 409–427 (2016).

69. Palmieri, V. *et al.* Dynamic light scattering for the characterization and counting of extracellular vesicles: a powerful noninvasive tool. *Journal of Nanoparticle Research* **16**, 2583 (2014).

70. Pusey, P. N. & van Megen, W. Dynamic light scattering by non-ergodic media. *Physica A: Statistical Mechanics and its Applications* **157**, 705–741 (1989).

71. van Megen, W. & Pusey, P. N. Dynamic light-scattering study of the glass transition in a colloidal suspension. *Phys Rev A (Coll Park)* **43**, 5429–5441 (1991).

72. Varenne, F., Makky, A., Gaucher-Delmas, M., Violleau, F. & Vauthier, C. Multimodal Dispersion of Nanoparticles: A Comprehensive Evaluation of Size Distribution with 9 Size Measurement Methods. *Pharm Res* **33**, 1220–1234 (2016).

73. Weatherall, E. & Willmott, G. R. Applications of tunable resistive pulse sensing. *Analyst* **140**, 3318–3334 (2015).

74. Willmott, G. R. Tunable Resistive Pulse Sensing: Better Size and Charge Measurements for Submicrometer Colloids. *Anal Chem* **90**, 2987–2995 (2018).

75. Vogel, R. *et al.* Quantitative Sizing of Nano/Microparticles with a Tunable Elastomeric Pore Sensor. *Anal Chem* **83**, 3499–3506 (2011).

76. Willmott, G. R. Tunable Resistive Pulse Sensing: Better Size and Charge Measurements for Submicrometer Colloids. *Anal Chem* **90**, 2987–2995 (2018).

77. Pal, A. K. *et al.* High Resolution Characterization of Engineered Nanomaterial Dispersions in Complex Media Using Tunable Resistive Pulse Sensing Technology. *ACS Nano* **8**, 9003–9015 (2014).

78. Sowerby, S. J., Broom, M. F. & Petersen, G. B. Dynamically resizable nanometre-scale apertures for molecular sensing. *Sens Actuators B Chem* **123**, 325–330 (2007).

79. Barth, H. G., Boyes, B. E. & Jackson, C. Size Exclusion Chromatography. *Anal Chem* **68**, 445–466 (1996).

80. Kostanski, L. K., Keller, D. M. & Hamielec, A. E. Size-exclusion chromatography—a review of calibration methodologies. *J Biochem Biophys Methods* **58**, 159–186 (2004).

81. Pitkänen, L. & Striegel, A. M. Size-exclusion chromatography of metal nanoparticles and quantum dots. *TrAC Trends in Analytical Chemistry* **80**, 311–320 (2016).

82. Kunji, E. R. S., Harding, M., Butler, P. J. G. & Akamine, P. Determination of the molecular mass and dimensions of membrane proteins by size exclusion chromatography. *Methods* **46**, 62–72 (2008).

83. Pujar, N. S. & Zydney, A. L. Electrostatic effects on protein partitioning in size-exclusion chromatography and membrane ultrafiltration. *J Chromatogr A* **796**, 229–238 (1998).

84. Süß, S., Metzger, C., Damm, C., Segets, D. & Peukert, W. Quantitative evaluation of nanoparticle classification by size-exclusion chromatography. *Powder Technol* **339**, 264–272 (2018).

85. Calvin, G. J., F, Y. F. J. & N, M. M. Flow-Field-Flow Fractionation: A Versatile New Separation Method. *Science (1979)* **193**, 1244–1245 (1976).

86. Giddings, J. Calvin., Yang, F. J. & Myers, M. N. Theoretical and experimental characterization of flow field-flow fractionation. *Anal Chem* **48**, 1126–1132 (1976).

87. Williams, S. K. R., Runyon, J. R. & Ashames, A. A. Field-Flow Fractionation: Addressing the Nano Challenge. *Anal Chem* **83**, 634–642 (2011).

88. Wahlund, K.-G. Flow field-flow fractionation: Critical overview. *J Chromatogr A* **1287**, 97–112 (2013).

89. Davis, J. M. Influence of crossflow hydrodynamics on retention ratio in flow field-flow fractionation. *Anal Chim Acta* **246**, 161–169 (1991).

90. Zhang, H. & Lyden, D. Asymmetric-flow field-flow fractionation technology for exomere and small extracellular vesicle separation and characterization. *Nat Protoc* **14**, 1027–1053 (2019).

91. Williams, P. S., Carpino, F. & Zborowski, M. Magnetic Nanoparticle Drug Carriers and Their Study by Quadrupole Magnetic Field-Flow Fractionation. *Mol Pharm* **6**, 1290–1306 (2009).

92. Huang, Y., Wang, X. B., Becker, F. F. & Gascoyne, P. R. Introducing dielectrophoresis as a new force field for field-flow fractionation. *Biophys J* **73**, 1118–1129 (1997).

93. Gascoyne, P. R. C. Dielectrophoretic-Field Flow Fractionation Analysis of Dielectric, Density, and Deformability Characteristics of Cells and Particles. *Anal Chem* **81**, 8878–8885 (2009).

94. Liu, J. & Shire, S. J. Analytical ultracentrifugation in the pharmaceutical industry. *J Pharm Sci* **88**, 1237–1241 (1999).

95. Carney, R. P. *et al.* Determination of nanoparticle size distribution together with density or molecular weight by 2D analytical ultracentrifugation. *Nat Commun* **2**, 335 (2011).

96. Planken, K. L. & Cölfen, H. Analytical ultracentrifugation of colloids. *Nanoscale* **2**, 1849–1869 (2010).

97. Lawrie, A. S., Albanyan, A., Cardigan, R. A., Mackie, I. J. & Harrison, P. Microparticle sizing by dynamic light scattering in fresh-frozen plasma. *Vox Sang* **96**, 206–212 (2009).

98. Filipe, V., Hawe, A. & Jiskoot, W. Critical Evaluation of Nanoparticle Tracking Analysis (NTA) by NanoSight for the Measurement of Nanoparticles and Protein Aggregates. *Pharm Res* **27**, 796–810 (2010).

99. Mertz, J. Widefield Microscopy. in *Introduction to Optical Microscopy* (ed. Mertz, J.) 185–210 (Cambridge University Press, 2019). doi:DOI: 10.1017/9781108552660.012.

100. Priest, L., Peters, J. S. & Kukura, P. Scattering-based Light Microscopy: From Metal Nanoparticles to Single Proteins. *Chem Rev* **121**, 11937–11970 (2021).

101. van de Hulst, H. C. Conservation of energy and momentum. in *Light scattering by small particles* 11–16 (Dover Publications, Inc., 1981).

102. van de Hulst, H. C. Rigorous scattering theory for spheres of arbitrary size (Mie theory). in *Light scattering by small particles* 114–130 (Dover Publications, Inc., 1981).

103. van de Hulst, H. C. Particles small compared to the wavelength. in *Light scattering by small particles* 63–84 (Dover Publications, Inc., 1981).

104. Niskanen, I. *et al.* Determination of nanoparticle size using Rayleigh approximation and Mie theory. *Chem Eng Sci* **201**, 222–229 (2019).

105. Qian, H., Sheetz, M. P. & Elson, E. L. Single particle tracking. Analysis of diffusion and flow in two-dimensional systems. *Biophys J* **60**, 910–921 (1991).

106. Ruthardt, N., Lamb, D. C. & Bräuchle, C. Single-particle Tracking as a Quantitative Microscopy-based Approach to Unravel Cell Entry Mechanisms of Viruses and Pharmaceutical Nanoparticles. *Molecular Therapy* **19**, 1199–1211 (2011).

107. Silmore, K. S., Gong, X., Strano, M. S. & Swan, J. W. High-Resolution Nanoparticle Sizing with Maximum A Posteriori Nanoparticle Tracking Analysis. *ACS Nano* **13**, 3940–3952 (2019).

108. Edward, J. T. Molecular volumes and the Stokes-Einstein equation. *J Chem Educ* **47**, 261 (1970).

109. Schultz, S. G. & Solomon, A. K. Determination of the Effective Hydrodynamic Radii of Small Molecules by Viscometry. *Journal of General Physiology* **44**, 1189–1199 (1961).

110. Maguire, C. M., Rösslein, M., Wick, P. & Prina-Mello, A. Characterisation of particles in solution – a perspective on light scattering and comparative technologies. *Sci Technol Adv Mater* **19**, 732–745 (2018).

111. Hoover, B. M. & Murphy, R. M. Evaluation of Nanoparticle Tracking Analysis for the Detection of Rod-Shaped Particles and Protein Aggregates. *J Pharm Sci* **109**, 452–463 (2020).

112. Giebel, B. & Helmbrecht, C. Methods to Analyze EVs. in *Exosomes and Microvesicles: Methods and Protocols* (ed. Hill, A. F.) 1–20 (Springer New York, 2017). doi:10.1007/978-1-4939-6728-5_1.

113. Szakács, Z., Mészáros, T., de Jonge, M. I. & Gyurcsányi, R. E. Selective counting and sizing of single virus particles using fluorescent aptamer-based nanoparticle tracking analysis. *Nanoscale* **10**, 13942–13948 (2018).

114. Osten, W. *et al.* Recent advances in digital holography [Invited]. *Appl Opt* **53**, G44–G63 (2014).

115. Goodman, J. W. *Introduction to Fourier Optics*. (McGraw-Hill, 1996).

116. Poon, T.-C. & Liu, J.-P. *Introduction to Modern Digital Holography*. (Cambridge University Press, 2014). doi:10.1017/CBO9781139061346.

117. Kim, M. K. *Digital Holographic Microscopy*. vol. 162 (Springer New York, 2011).

118. Schnars, U., Falldorf, C., Watson, J. & Jüptner, W. *Digital Holography and Wavefront Sensing*. (Springer Berlin Heidelberg, 2015). doi:10.1007/978-3-662-44693-5.

119. Gabor, D. A New Microscopic Principle. *Nature* **161**, 777–778 (1948).

120. Schnars, U., Falldorf, C., Watson, J. & Jüptner, W. Digital Holography. in *Digital Holography and Wavefront Sensing: Principles, Techniques and Applications* (eds. Schnars, U., Falldorf, C., Watson, J. & Jüptner, W.) 39–68 (Springer Berlin Heidelberg, 2015). doi:10.1007/978-3-662-44693-5_3.

121. Cuche, E., Marquet, P. & Depeursinge, C. Spatial filtering for zero-order and twin-image elimination in digital off-axis holography. *Appl Opt* **39**, 4070 (2000).

122. Kühn, J. Multiple-wavelength digital holographic microscopy. 233 (2009) doi:10.5075/epfl-thesis-4399.

123. Kim, M. K. Introduction. in *Digital Holographic Microscopy: Principles, Techniques, and Applications* (ed. Kim, M. K.) 1–10 (Springer New York, 2011). doi:10.1007/978-1-4419-7793-9_1.

124. H J Kreuzer, M J Jericho, I A Meinertzhagen & Wenbo Xu. Digital in-line holography with photons and electrons. *Journal of Physics: Condensed Matter* **13**, 10729 (2001).

125. Xu, W., Jericho, M. H., Meinertzhagen, I. A. & Kreuzer, H. J. Digital in-line holography of microspheres. *Appl Opt* **41**, 5367–5375 (2002).

126. Kim, M. K. Digital Holography Configurations. in *Digital Holographic Microscopy: Principles, Techniques, and Applications* (ed. Kim, M. K.) 55–69 (Springer New York, 2011). doi:10.1007/978-1-4419-7793-9_5.

127. Ortega-Arroyo, J. & Kukura, P. Interferometric scattering microscopy (iSCAT): new frontiers in ultrafast and ultrasensitive optical microscopy. *Phys. Chem. Chem. Phys.* **14**, 15625 (2012).

128. Orzó, L. High speed phase retrieval of in-line holograms by the assistance of corresponding off-axis holograms. *Opt Express* **23**, 16638–16649 (2015).

129. Leith, E. N. & Upatnieks, J. Reconstructed Wavefronts and Communication Theory*. *J Opt Soc Am* **52**, 1123–1130 (1962).

130. Weigel, A., Sebesta, A. & Kukura, P. Dark Field Microspectroscopy with Single Molecule Fluorescence Sensitivity. *ACS Photonics* **1**, 848–856 (2014).

131. Kim, M. K. Numerical Techniques of Digital Holography. in *Digital Holographic Microscopy: Principles, Techniques, and Applications* (ed. Kim, M. K.) 109–127 (Springer New York, 2011). doi:10.1007/978-1-4419-7793-9_9.

132. Goodman, J. W. Analysis of Two-Dimensional Signals and Systems. in *Introduction to Fourier Optics* 32–62 (McGraw-Hill, 1996).

133. Goodman, J. W. Wave-Optics Analysis of Coherent Optical Systems. in *Introduction to Fourier Optics* 96–125 (McGraw-Hill, 1996).

134. Kim, M. K. Suppression of DC and Twin-Image Terms. in *Digital Holographic Microscopy: Principles, Techniques, and Applications* (ed. Kim, M. K.) 85–94 (Springer New York, 2011). doi:10.1007/978-1-4419-7793-9_7.

135. Douglass, K. M., Sieben, C., Archetti, A., Lambert, A. & Manley, S. Super-resolution imaging of multiple cells by optimized flat-field epi-illumination. *Nat Photonics* **10**, 705–708 (2016).

136. Cole, R. W., Jinadasa, T. & Brown, C. M. Measuring and interpreting point spread functions to determine confocal microscope resolution and ensure quality control. *Nat Protoc* **6**, 1929–1941 (2011).

137. Goodman, J. W. Foundations of Scalar Diffraction Theory. in *Introduction to Fourier Optics* 32–62 (McGraw-Hill, 1996).

138. Kim, M. K. Diffraction and Fourier Optics. in *Digital Holographic Microscopy: Principles, Techniques, and Applications* (ed. Kim, M. K.) 11–28 (Springer New York, 2011). doi:10.1007/978-1-4419-7793-9_2.

139. Liu, S., Xiao, W. & Pan, F. Automatic compensation of phase aberrations in digital holographic microscopy for living cells investigation by using spectral energy analysis. *Opt Laser Technol* **57**, 169–174 (2014).

140. Memmolo, P. *et al.* Recent advances in holographic 3D particle tracking. *Adv Opt Photonics* **7**, 713 (2015).

141. Yu, L. & Kim, M. K. Wavelength-scanning digital interference holography for tomographic three-dimensional imaging by use of the angular spectrum method. *Opt Lett* **30**, 2092 (2005).

142. Joan, B., Cheryl, D., Nidia, L., Tina, M. & Tammy, T. Clinical and Financial Benefits of Rapid Detection of Respiratory Viruses: an Outcomes Study. *J Clin Microbiol* **38**, 2824–2828 (2000).

143. Ko, F. & Drews, S. J. The impact of commercial rapid respiratory virus diagnostic tests on patient outcomes and health system utilization. *Expert Rev Mol Diagn* **17**, 917–931 (2017).

144. Nouvellet, P. *et al.* The role of rapid diagnostics in managing Ebola epidemics. *Nature* **528**, S109–S116 (2015).

145. Kerman, K., Saito, M., Tamiya, E., Yamamura, S. & Takamura, Y. Nanomaterial-based electrochemical biosensors for medical applications. *TrAC Trends in Analytical Chemistry* **27**, 585–592 (2008).

146. González-Guerrero, A. B., Maldonado, J., Herranz, S. & Lechuga, L. M. Trends in photonic lab-on-chip interferometric biosensors for point-of-care diagnostics. *Analytical Methods* **8**, 8380–8394 (2016).

147. Koukouvinos, G. *et al.* Development and Bioanalytical Applications of a White Light Reflectance Spectroscopy Label-Free Sensing Platform. *Biosensors (Basel)* **7**, (2017).

148. Reta, N., Saint, C. P., Michelmore, A., Prieto-Simon, B. & Voelcker, N. H. Nanostructured Electrochemical Biosensors for Label-Free Detection of Water- and Food-Borne Pathogens. *ACS Appl Mater Interfaces* **10**, 6055–6072 (2018).

149. Xu, K., Zhou, R., Takei, K. & Hong, M. Toward Flexible Surface-Enhanced Raman Scattering (SERS) Sensors for Point-of-Care Diagnostics. *Advanced Science* **6**, 1900925 (2019).

150. Soler, M., Huertas, C. S. & Lechuga, L. M. Label-free plasmonic biosensors for point-of-care diagnostics: a review. *Expert Rev Mol Diagn* **19**, 71–81 (2019).

151. Soler, M., Estevez, M. C., Cardenosa-Rubio, M., Astua, A. & Lechuga, L. M. How Nanophotonic Label-Free Biosensors Can Contribute to Rapid and Massive Diagnostics of Respiratory Virus Infections: COVID-19 Case. *ACS Sens* **5**, 2663–2678 (2020).

152. Zheng, G., Horstmeyer, R. & Yang, C. Wide-field, high-resolution Fourier ptychographic microscopy. *Nat. Photonics* **7**, 739–745 (2013).

153. Ozcan, A. & McLeod, E. Lensless Imaging and Sensing. *Annu. Rev. Biomed. Eng.* **18**, 77–102 (2016).

154. Curtis, A. S. G. A Study by Interference Reflection Microscopy. *J. Cell Biol.* **20**, 199–215 (1964).

155. Piliarik, M. & Sandoghdar, V. Direct optical sensing of single unlabelled proteins and super-resolution imaging of their binding sites. *Nat. Commun.* **5**, 4495 (2014).

156. Lin, Y.-H., Wei-Lin, C. & Hsieh, C.-L. Shot-noise limited localization of single 20 nm gold particles with nanometer spatial precision within microseconds. *Opt. Express* **22**, 9159–9170 (2014).

157. Mathieu, M., Martin-Jaular, L., Lavieu, G. & Théry, C. Specificities of secretion and uptake of exosomes and other extracellular vesicles for cell-to-cell communication. *Nat. Cell Biol.* **21**, 9–17 (2019).

158. Bachurski, D. *et al.* Extracellular vesicle measurements with nanoparticle tracking analysis–An accuracy and repeatability comparison between NanoSight NS300 and ZetaView. *J. Extracell. Vesicles* **8**, 1596016 (2019).

159. Gandham, S. *et al.* Technologies and Standardization in Research on Extracellular Vesicles. *Trends Biotechnol* **38**, 1066–1098 (2020).

160. Sitar, S. *et al.* Size Characterization and Quantification of Exosomes by Asymmetrical-Flow Field-Flow Fractionation. *Anal Chem* **87**, 9225–9233 (2015).

161. Akers, J. C. *et al.* Comparative Analysis of Technologies for Quantifying Extracellular Vesicles (EVs) in Clinical Cerebrospinal Fluids (CSF). *PLoS One* **11**, e0149866 (2016).

162. Bachurski, D. *et al.* Extracellular vesicle measurements with nanoparticle tracking analysis – An accuracy and repeatability comparison between NanoSight NS300 and ZetaView. *J Extracell Vesicles* **8**, 1596016 (2019).

163. Faez, S. *et al.* Fast, Label-Free Tracking of Single Viruses and Weakly Scattering Nanoparticles in a Nanofluidic Optical Fiber. *ACS Nano* **9**, 12349–12357 (2015).

164. Vollmer, F. & Yang, L. Review Label-free detection with high-Q microcavities: a review of biosensing mechanisms for integrated devices. *Nanophotonics* **1**, 267–291.

165. Schnars, U. & Jüptner, W. Direct recording of holograms by a CCD target and numerical reconstruction. *Appl Opt* **33**, 179–181 (1994).

166. Hillman, T. R., Gutzler, T., Alexandrov, S. A. & Sampson, D. D. High-resolution, wide-field object reconstruction with synthetic aperture Fourier holographic optical microscopy. *Opt. Express* **17**, 7873–7892 (2006).

167. Alexandrov, S. A., Hillman, T. R., Gutzler, T. & Sampson, D. D. Synthetic aperture Fourier holographic optical microscopy. *Phys. Rev. Lett.* **97**, 1–4 (2006).

168. Holanová, K., Vala, M. & Piliarik, M. [INVITED] Optical imaging and localization of prospective scattering labels smaller than a single protein. *Opt Laser Technol* **109**, 323–327 (2019).

169. Takeda, M., Ina, H. & Kobayashi, S. Fourier-transform method of fringe-pattern analysis for computer-based topography and interferometry. *J. Opt. Soc. Am.* **72**, 156 (1982).

170. Verrier, N. & Atlan, M. Off-axis digital hologram reconstruction: some practical considerations. *Appl Opt* **50**, H136 (2011).

171. Poon, T.-C. & Liu, J.-P. *Introduction to Modern Digital Holography*. (Cambridge University Press, 2013). doi:10.1017/CBO9781139061346.

172. Charrière, F. *et al.* Shot-noise influence on the reconstructed phase image signal-to-noise ratio in digital holographic microscopy. *Appl Opt* **45**, 7667 (2006).

173. Gardiner, C. *et al.* Measurement of refractive index by nanoparticle tracking analysis reveals heterogeneity in extracellular vesicles. *J Extracell Vesicles* **3**, 25361 (2014).

174. McMeekin, T. L., Groves, M. L. & Hipp, N. J. Refractive Indices of Amino Acids, Proteins, and Related Substances. in *Amino Acids and Serum Proteins* vol. 44 54–66 (American Chemical Society, 1964).

175. Bachurski, D. *et al.* Extracellular vesicle measurements with nanoparticle tracking analysis–An accuracy and repeatability comparison between NanoSight NS300 and ZetaView. *J. Extracell. Vesicles* **8**, 1596016 (2019).

176. Rupert, D. L. M. *et al.* Effective Refractive Index and Lipid Content of Extracellular Vesicles Revealed Using Optical Waveguide Scattering and Fluorescence Microscopy. *Langmuir* **34**, 8522–8531 (2018).

177. de Rond, L. *et al.* Refractive index to evaluate staining specificity of extracellular vesicles by flow cytometry. *J. Extracell. Vesicles* **8**, 1643671 (2019).

178. Im, H. *et al.* Label-free detection and molecular profiling of exosomes with a nano-plasmonic sensor. *Nat Biotechnol* **32**, 490 (2014).

179. Daaboul, G. G. *et al.* Digital Detection of Exosomes by Interferometric Imaging. *Sci Rep* **6**, 37246 (2016).

180. Ortega Arroyo, J. *et al.* Label-Free, All-Optical Detection, Imaging, and Tracking of a Single Protein. *Nano Lett* **14**, 2065–2070 (2014).

181. Yang, Y. *et al.* Interferometric plasmonic imaging and detection of single exosomes. *Proceedings of the National Academy of Sciences* **115**, 10275–10280 (2018).

182. Tamamitsu, M. *et al.* Label-free biochemical quantitative phase imaging with mid-infrared photothermal effect. *Optica* **7**, 359–366 (2020).

183. Bai, Y., Yin, J. & Cheng, J.-X. Bond-selective imaging by optically sensing the mid-infrared photothermal effect. *Sci Adv* **7**, eabg1559 (2022).

184. Chernyshev, V. S. *et al.* Size and shape characterization of hydrated and desiccated exosomes. *Anal Bioanal Chem* **407**, 3285–3301 (2015).

185. McLeod, E. *et al.* High-Throughput and Label-Free Single Nanoparticle Sizing Based on Time-Resolved On-Chip Microscopy. *ACS Nano* **9**, 3265–3273 (2015).

186. Pelaz, B. *et al.* Interfacing Engineered Nanoparticles with Biological Systems: Anticipating Adverse Nano–Bio Interactions. *Small* **9**, 1573–1584 (2013).

187. Treuel, L. *et al.* Physicochemical characterization of nanoparticles and their behavior in the biological environment. *Phys. Chem. Chem. Phys.* **16**, 15053–15067 (2014).

188. Moore, T. L. *et al.* Nanoparticle colloidal stability in cell culture media and impact on cellular interactions. *Chem Soc Rev* **44**, 6287–6305 (2015).

189. Yang, S.-A., Choi, S., Jeon, S. M. & Yu, J. Silica nanoparticle stability in biological media revisited. *Sci Rep* **8**, 185 (2018).

190. van der Pol, E., Coumans, F. A. W., Sturk, A., Nieuwland, R. & van Leeuwen, T. G. Refractive Index Determination of Nanoparticles in Suspension Using Nanoparticle Tracking Analysis. *Nano Lett* **14**, 6195–6201 (2014).

191. van der Pol, E. *et al.* Absolute sizing and label-free identification of extracellular vesicles by flow cytometry. *Nanomedicine* **14**, 801–810 (2018).

192. Midekessa, G. *et al.* Zeta Potential of Extracellular Vesicles: Toward Understanding the Attributes that Determine Colloidal Stability. *ACS Omega* **5**, 16701–16710 (2020).

193. Pino, P. Del *et al.* Protein corona formation around nanoparticles - From the past to the future. *Mater Horiz* **1**, 301–313 (2014).

194. Born, M. Mean first-passage times of Brownian motion and related problems. *Proc R Soc Lond A Math Phys Sci* **211**, 431–443 (1952).

195. Saxton, M. J. Single-particle tracking: the distribution of diffusion coefficients. *Biophys J* **72**, 1744–1753 (1997).

196. Martinez-Marrades, A., Rupprecht, J.-F., Gross, M. & Tessier, G. Stochastic 3D optical mapping by holographic localization of Brownian scatterers. *Opt Express* **22**, 29191 (2014).

197. Parthasarathy, R. Rapid, accurate particle tracking by calculation of radial symmetry centers. *Nat Methods* **9**, 724–726 (2012).

198. Jaqaman, K. *et al.* Robust single-particle tracking in live-cell time-lapse sequences. *Nat Methods* **5**, 695–702 (2008).

199. Corbo, C. *et al.* The impact of nanoparticle protein corona on cytotoxicity, immunotoxicity and target drug delivery. *Nanomedicine* **11**, 81–100 (2015).

200. Barui, A. K., Oh, J. Y., Jana, B., Kim, C. & Ryu, J.-H. Cancer-Targeted Nanomedicine: Overcoming the Barrier of the Protein Corona. *Adv Ther (Weinh)* **3**, 1900124 (2020).

201. Sarangapani, P. S., Hudson, S. D., Migler, K. B. & Pathak, J. A. The Limitations of an Exclusively Colloidal View of Protein Solution Hydrodynamics and Rheology. *Biophys J* **105**, 2418–2426 (2013).

202. Brewer, S. H., Glomm, W. R., Johnson, M. C., Knag, M. K. & Franzen, S. Probing BSA Binding to Citrate-Coated Gold Nanoparticles and Surfaces. *Langmuir* **21**, 9303–9307 (2005).

203. Casals, E., Pfaller, T., Duschl, A., Oostingh, G. J. & Puntes, V. Time Evolution of the Nanoparticle Protein Corona. *ACS Nano* **4**, 3623–3632 (2010).

204. Dominguez-Medina, S., McDonough, S., Swanglap, P., Landes, C. F. & Link, S. In Situ Measurement of Bovine Serum Albumin Interaction with Gold Nanospheres. *Langmuir* **28**, 9131–9139 (2012).

205. Jain, A., Barve, A., Zhao, Z., Jin, W. & Cheng, K. Comparison of Avidin, Neutravidin, and Streptavidin as Nanocarriers for Efficient siRNA Delivery. *Mol Pharm* **14**, 1517–1527 (2017).

206. Tan, X. & Welsher, K. Particle-by-Particle In Situ Characterization of the Protein Corona via Real-Time 3D Single-Particle-Tracking Spectroscopy. *Angewandte Chemie International Edition* **60**, 22359–22367 (2021).

207. Kashkanova, A. D., Blessing, M., Gemeinhardt, A., Soulat, D. & Sandoghdar, V. Precision size and refractive index analysis of weakly scattering nanoparticles in polydispersions. *Nat Methods* 2021.11.13.468485 (2022) doi:10.1038/s41592-022-01460-z.

208. Špačková, B. *et al.* Label-free nanofluidic scattering microscopy of size and mass of single diffusing molecules and nanoparticles. *Nat Methods* **19**, 751–758 (2022).

209. Moghimi, S. M., Hunter, A. C. & Murray, J. C. Nanomedicine: current status and future prospects. *The FASEB Journal* **19**, 311–330 (2005).

210. Riehemann, K. *et al.* Nanomedicine—Challenge and Perspectives. *Angewandte Chemie International Edition* **48**, 872–897 (2009).

211. Pelaz, B. *et al.* Diverse Applications of Nanomedicine. *ACS Nano* **11**, 2313–2381 (2017).

212. Shi, J., Kantoff, P. W., Wooster, R. & Farokhzad, O. C. Cancer nanomedicine: progress, challenges and opportunities. *Nat Rev Cancer* **17**, 20–37 (2017).

213. Barui, A. K., Oh, J. Y., Jana, B., Kim, C. & Ryu, J.-H. Cancer-Targeted Nanomedicine: Overcoming the Barrier of the Protein Corona. *Adv Ther (Weinh)* **3**, 1900124 (2020).

214. Weber, C., Morsbach, S. & Landfester, K. Possibilities and Limitations of Different Separation Techniques for the Analysis of the Protein Corona. *Angewandte Chemie International Edition* **58**, 12787–12794 (2019).

215. Nan, X., Sims, P. A. & Xie, X. S. Organelle Tracking in a Living Cell with Microsecond Time Resolution and Nanometer Spatial Precision. *ChemPhysChem* **9**, 707–712 (2008).

216. Jokinen, V., Suvanto, P. & Franssila, S. Oxygen and nitrogen plasma hydrophilization and hydrophobic recovery of polymers. *Biomicrofluidics* **6**, 016501 (2012).

217. Cai, S. & Bhushan, B. Meniscus and viscous forces during separation of hydrophilic and hydrophobic surfaces with liquid-mediated contacts. *Materials Science and Engineering: R: Reports* **61**, 78–106 (2008).

218. Lafleur, J. P. *et al.* Rapid and simple preparation of thiol–ene emulsion-templated monoliths and their application as enzymatic microreactors. *Lab Chip* **15**, 2162–2172 (2015).

219. Xia, Y. & Whitesides, G. M. Soft Lithography. *Angewandte Chemie International Edition* **37**, 550–575 (1998).

220. Su, T. J., Lu, Thomas, R. K., Cui, Z. F. & Penfold, J. The Conformational Structure of Bovine Serum Albumin Layers Adsorbed at the Silica−Water Interface. *J Phys Chem B* **102**, 8100–8108 (1998).